



*Highly advanced Probabilistic design and Enhanced Reliability methods for high-value, cost-efficient offshore WIND*

Title: Wave field characterization and associated uncertainties  
Deliverable no: D2.2

Delivery date: 28.02.2023  
Lead beneficiary: EDF  
Dissemination level: Public



*This project has received funding from the European Union's Horizon 2020 Research and Innovation Programme under Grant Agreement No. 101006689*







|   |    |
|---|----|
| 1. Introduction.....  | 3  |
| 2. HOSM – DNV: Validations, study of the breaking model and statistics at crests..... | 5  |
| 3. HOS vs linear prediction of kinematics. ....                                       | 31 |
| 4. Influence of bathymetry – A non-hydrostatic multilayer wave model .....            | 61 |
| 5. General conclusion.....  | 80 |
| 6. Synthesis on the uncertainties.....  | 80 |
| 7. References.....  | 81 |

## Abstract

The representation of a temporal sea state from a spectrum or scatter diagram is a necessary step in the design chain of a structure submitted to water waves over a long time. Usually, a linear approach is taken, and multiple simulations are conducted with different phases fields to obtain statistically converged results. This approach suffers multiple flaws arising from the strong hypothesis of the linear theory. A model, denoted stretching model, is often used to overcome the most impactful one: no solution is given above the still water level. We first tackle the influence of those stretching models by comparing them to a High Order Spectral approach. Effects of other usual assumptions and methodologies used in the engineering field are also quantified, such as the choice of unidirectional spectrum, the effect of selecting a deterministic amplitude as well as the wave breaking influence. To quantify these effects, three variables are investigated: the free surface elevation, horizontal velocity and horizontal acceleration, and their prediction are compared between model from a statistical point of view. Four different site and sea states are selected to tackle a broad range of conditions.

This report describes the work carried out by DNV and EDF in work package WP2 (Environmental condition modelling) task 2.4 (nonlinear phase-resolved wave modelling) as part of deliverable D2.2 (Realistic representation of nonlinear wave conditions applicable for offshore wind turbine design).

In total, three wave models have been considered in this work:

- A linear potential model (Calhypso), along with multiple variations of the free surface stretching models.
- A higher order spectral (HOS) method suitable for highly efficient nonlinear simulation of waves in rectangular period domains with constant water depth. Two different numerical implementations of the method were used: denoted HOSM (DNV), and Cosmhos (EDF).
- A Boussinesq-like multilayer model, suitable for simulation of waves in more complex domains with variable complex bathymetry

The existing DNV HOSM code as well as the EDF Cosmhos code have been extended with a wave-breaking model, providing improved description of steep sea states in which wave breaking plays a role. Extensive validation of HOSM with the newly implemented breaking model has been carried out through comparison

with model-test data for long- and short-crested irregular sea states, and through direct comparison of wave crests and wave kinematics from full CFD simulations.

It is shown that HOSM predicts wave-crest statistics in good agreement with model-test results over a wide range of different sea state parameters, but that a breaking model is crucial for reliable results in steep sea states. By comparing with full CFD-simulations (which are several orders of magnitudes slower than HOSM from a computational point of view) it is shown that HOSM predicts surface elevation (crest heights) as well as wave kinematics below mean water level in good agreement with CFD-results, while the deterministic agreement for kinematics in breaking crests are less good. However, for a statistical point of view it is seen that HOSM seems to be conservative relative to CFD-results.

As a case study, HOSM has been used in long- and short-crested simulations of four sea states relevant for the Teesside and Brittany sites considered in the Hiperwind project. Resulting crests wave elevation statistics (considering return periods up to 1000 hours for each sea state) are compared with commonly used reference distributions based on linear and second-order theories as well as to recent distributions taking wave-breaking and shallow water depth into account. It is shown that HOSM predicts results in good agreement with the relevant reference distributions.

Hence, it is shown that HOSM represents an attractive alternative to simpler approaches based on linear- or second-order theories. A new event-based approach, that enables using HOSM in full long-term analyses of wave-induced loads to estimate return periods up to 10 000 years has also been developed and validated in the present work.

As a continuation, the EDF HOS model, denoted Cosmhos, has been used to compute the statistics of the three main variables of interest at the free surface: the free surface elevation, the horizontal velocity and the horizontal acceleration.

With all of the most common stretching models, used in addition to a linear potential prediction, it is shown that most of the time, an underprediction of maxima of the studied variable is obtained.

In addition to HOSM, a multilayer-wave model [1] suitable for large-scale simulation of waves in complex geometries and with variable bathymetry is considered, and validated. Despite being more computational expensive than HOSM, it is still capable of propagating long time-series of 2D and 3D irregular wave fields. Through validation against various deep and shallow water cases, the model has proven to be robust when tackling wave breaking, wetting and drying of the coastline as waves hit the shore. It is also capable of reproducing model test measurements at a high accuracy level. The multilayer wave model has shown to be a promising tool for wave modelling in complex nearshore locations.

## 1. Introduction

In the context of design of offshore structures submitted to waves, the accurate quantification of the flow kinematics and free surface elevation is of prime importance. For example, for wave loads applied on slender structures such as cables or monopile of contained diameter compared to the wavelength, the Morison formulation is valid and commonly used in the engineering field. However, this approach necessitates the determination of the instantaneous wet surface (i.e., the free surface elevation), and the kinematics up to the wave crest. In addition, the wave environment needs to be described over very long time periods, e.g. for wave-in-deck loads on jacket structures return periods up to  $10^4$  years are typically considered. Traditionally, linear- or second-order random wave theories are often used to describe the short-

and long-term wave properties such as distribution of wave crest heights, while design loads are often calculated using regular waves (e.g. Stokes fifth order) with crest height according to the appropriate return period. Commonly, irregular sea states are represented by a theoretical spectrum, usually of JONSWAP type. The different components of the spectrum are assumed to be linear (Airy waves) and independent: the free surface elevation is determined via the addition of the different wave components. There are however several inaccuracies and uncertainties related to such simplified approaches. Higher order nonlinear effects may give larger crest elevations than predicted by second order theory, for two separate reasons: first, as an effect of higher-order bound waves and secondly to nonlinear modulation effects. An example of those modulation effect is the modulational instability which is suggested to play a role in generation of rare extreme events (often referred to as rogue or freak waves, see e.g. [2]–[4]). Also, one of the shortcomings of linear methods is the fact that, given the linear assumption, the different variables are only available up to the mean water level ( $z = 0$ ).

Today, Computational Fluid Dynamic (CFD) methods can simulate nonlinear and breaking waves with high accuracy, although with a significant computational cost prohibitive for estimating long-term wave statistics and wave-induced loads directly. However, in the range from simple analytical methods like linear and second-order wave-theories and "full" CFD-methods, there are a wide range of simplified methods that describe nonlinear waves under different simplifying assumptions (e.g. weak nonlinearity, narrow spectral bandwidth, potential theory and shallow water depth to mention some).

One such simplified model is the so-called High Order Spectral Method (HOSM), which is a numerical method for describing nonlinear waves under assumption of potential theory. It enables highly efficient simulation of irregular short-crested waves, including calculation of wave kinematics in the fluid domain (see e.g. [5]–[7]).

This report presents the different investigations conducted on the weight of the different commonly made assumptions in the design chain: in particular, is investigated here the effect on the free surface elevation and kinematics of:

- the linearity assumption, by comparing a linear simulation with different stretching models to a highly non-linear model (HOS). This part of the study also serves to assess the capabilities of the different stretching models to extrapolate the kinematics up to the free surface (for  $0 < z < \eta$ ),
- the choice, commonly encountered, of selecting random phases but deterministic amplitudes when representing a given frequency spectrum into a spatial wave field,
- the directionality of the spectrum, by comparing different spectrum spreading factors,
- the wave breaking on a relatively non-linear spectrum,

While HOSM is a highly efficient method for solving nonlinear wave fields in periodic rectangular domains of infinite water depth, it cannot easily describe waves propagating in more complex domains where waves are affected by e.g. coastlines and variable bathymetry. For such situations we consider another model well suited for large-scale simulation of waves in complex geometries with variable bathymetry [1].

In this report these two phase-resolved wave models are considered in the context of obtaining improved nonlinear description of the wave environment, relevant for the design of offshore structures. Extensive validations of these methods are presented, and various effects and choices related to the use of such models are discussed.

We first define the environmental conditions considered for the studies: two physical sites both with two different sea states are selected in section 3.1. The sites correspond to the south of French Brittany

(Coordinates: [ -4.5925; + 46.801]) and the Teesside site. Both are studied with two site specific sea states: one corresponding to a common sea state largely impacting the fatigue equivalent damage over the lifetime of the structure (based on hydrodynamic consideration only), and one corresponding to a severe sea state. We also describe the different models that will be used, namely the linear potential (DIEGO) and the High Order Spectral (HOS, cosmos) models. Afterwards, each parameter influence is studied, each in a dedicated section, namely section 3.2 for the nonlinearity, section 3.3 for the random amplitude, section 3.4 for the bidimensionality of the sea state and section 3.5 for the wave breaking. Section 3.6 summarize all simulations and influence, to compare the respective influence of the different studies, and conclude this report.

## 2. HOSM – DNV: Validations, study of the breaking model and statistics at crests.

### 2.1. Introduction

The High Order Spectral Method (HOSM) is based on the formulation of the potential water-wave problem (the Laplace equation with nonlinear kinematic and dynamic boundary conditions at the free surface) in the surface variables: the surface elevation  $\eta(\mathbf{x}, t)$  and the surface potential  $\psi(\mathbf{x}, t) = \phi(\mathbf{x}, z = \eta(\mathbf{x}, t), t)$ , where  $\phi(\mathbf{x}, z, t)$  is the velocity potential in the fluid domain, and  $\mathbf{x} = (x, y)$ . This formulation of the water wave basic equations was first presented by [8], who showed that they constitute a Hamiltonian system, with  $\eta$  and  $\psi$  as Hamiltonian variables, in the form

$$\begin{aligned}\frac{\partial \eta}{\partial t} &= w_s (1 + |\nabla \eta|^2) - \nabla \psi \cdot \nabla \eta, \\ \frac{\partial \psi}{\partial t} &= -g\eta - \frac{1}{2} |\nabla \psi|^2 + \frac{w_s^2}{2} (1 + |\nabla \eta|^2),\end{aligned}$$

where  $w_s = \left. \frac{\partial \phi}{\partial z} \right|_{z=\eta}$  is the vertical surface velocity and where  $\nabla = \left( \frac{\partial}{\partial x}, \frac{\partial}{\partial y} \right)$  is the horizontal gradient operator.

By using a pseudo-spectral approach, in which all spatial derivatives can be calculated in Fourier-space, the system above can easily be solved numerically using standard solvers for ordinary differential equations. This requires, however, that one can express the vertical surface velocity  $w_s$  in terms of  $\eta$  and  $\psi$ . An efficient iterative spectral method for evaluating  $w_s$  in terms of  $\eta$  and  $\psi$  was proposed by [5], [6], and has later been known as HOS/HOSM. It has been shown that HOSM alternatively can be derived and formulated in terms of the Dirichlet–Neumann operator [9], [10].

The solution of HOSM provides the surface elevation  $\eta$  and the surface potential  $\psi$  at every integration time step. However, in many practical applications the water particle kinematics are needed. The calculation of water particle kinematics within the HOSM formulation was considered by [7], who presented two methods for the calculation of the kinematics in an approach similar to the Dirichlet–Neumann operator applied in [9], [10]. In the DNV HOSM code [11] applied in this work the most accurate of these two methods, the so-called  $H_2$ -operator, is implemented.

Due to its simplicity and computational efficiency HOSM has become a widely used model for simulation of nonlinear waves, in particular in application where long- and large-scale simulation are needed to obtain

information about wave statistics, including extreme events occurring with low probability and populate the tails of the relevant wave statistical distributions (see e.g. [12]–[14]).

In this project, the following development and validation of HOSM has been carried out, as reported in the following sections.

- Implementation of a wave-breaking model in HOSM which extends the applicability of HOSM to steeper sea states in which wave-breaking plays a significant role.
- Validation of HOSM and the implemented wave-breaking model:
  - Comparison with model-tests results of irregular waves.
  - Direct comparison of HOSM and full CFD-simulation for a large number of wave events.
  - Comparison of crest distributions obtained from HOSM simulations to relevant reference distributions for wave crests.

## 2.2. Implementation of wave breaking model in HOSM

One important limitation of HOSM and other similar methods is the inability to describe wave breaking. The lack of breaking may lead to unrealistically steep and extreme waves in the simulations and associated problems with numerical instabilities, as well as overprediction of e.g. crest-heights in steep sea states. However, recently there have been several efforts on including wave breaking models in HOSM and similar models [15]–[17]. While such breaking models cannot describe the actual breaking process to full accuracy (e.g. overturning surface and accurate wave kinematic in a breaking crest), they often successfully identify the onset of breaking and are able to dissipate energy so that the waves are in reasonable agreement after and during the breaking event.

A breaking model based on the breaking criterion of [18] combined with the eddy-viscosity model of [19], [20] has been implemented and validated. The breaking criterion discussed in [18] is based on the ratio of the water particle velocity in the wave crest  $u$  and the local crest/phase velocity  $c$ . That is, a wave is considered to be breaking when  $B = u/c > U_c$  for some threshold  $U_c$ . It was reported in [18] that the onset of breaking was found to occur for  $0.85 < B < 0.86$ . Here,  $U_c = 0.85$  has been used, which also has been validated to agree well with model tests with respect to crest-height statistics.

As discussed in [15], the local crest velocity can be calculated from the local wavenumber  $k(\mathbf{x}, t)$  as

$$c(\mathbf{x}, t) = \sqrt{\frac{g \tanh(k(\mathbf{x}, t)h)}{k(\mathbf{x}, t)}}.$$

The local wavenumber can efficiently be calculated in HOSM using the Hilbert-transform in 1D and Riesz transform/monogenic signal [21] (see also [22] for a simple overview) in 2D. For unidirectional propagation this gives

$$k(x, t) = \frac{1}{\tilde{\eta}^2 + \eta^2} \left( \eta \frac{\partial \tilde{\eta}}{\partial x} + \tilde{\eta} \frac{\partial \eta}{\partial x} \right),$$

where  $\tilde{\eta}$  is the Hilbert-transform of  $\eta$  with respect to  $x$ .

The fluid velocity in the wave crest can be calculated as  $u = |\nabla\psi|$ , where it is used that

$$\nabla\phi|_{z=\eta} = \nabla\psi - \nabla\eta \frac{\partial\phi}{\partial z} \Big|_{z=\eta} = \nabla\psi,$$

since  $\nabla\eta = 0$  at a crest.

The actual breaking is modelled using the eddy-viscosity model described in [19], [20] and applies the modified HOSM equations in the following form

$$\begin{aligned} \frac{\partial\eta}{\partial t} &= w_s (1 + |\nabla\eta|^2) - \nabla\psi \cdot \nabla\eta + 2\nu_{eddy} \nabla^2\eta, \\ \frac{\partial\psi}{\partial t} &= -g\eta - \frac{1}{2} |\nabla\psi|^2 + \frac{w_s^2}{2} (1 + |\nabla\eta|^2) + 2\nu_{eddy} \nabla^2\psi, \end{aligned}$$

where  $\nu_{eddy} = 0$  for waves not satisfying the breaking criterion above, and  $\nu_{eddy} = \alpha H_{br} L_{br} / T_{br}$  for waves satisfying the breaking criterion.  $H_{br}$ ,  $L_{br}$  and  $T_{br}$  are properties of the breaking wave (see equations (12) and (14) in [20]) and  $\alpha$  is a constant, which is set to 0.02, as suggested in [19].

Extensive validation and testing of the two key parameters  $U_c$  and  $\alpha$  in the breaking model have been carried out through comparison of crest statistics from model tests. It has been found that the values suggested in the literature  $U_c \approx 0.85$  and  $\alpha \approx 0.02$  seems to fit well also when used in HOSM.

## 2.3. Details on running HOSM

The original HOS-formulation is suitable for describing the nonlinear time evolution of a given initial condition, defined by the surface elevation and surface potential in the computational domain, in a rectangular domain with periodic boundary conditions in both horizontal dimensions and constant water depth. Although there exist methods utilizing HOSM and HOSM-like formulations for e.g. non-periodic boundaries [23] and variable bathymetry [24], this typically leads to less efficient methods lacking some of the advantages of HOSM. In this work HOSM is run with constant water depth and periodic boundary conditions only. For situations with more complex geometries and variable bathymetry another wave model more suitable for this kind of problems is considered, as documented in Section 4.

In the following subsection, some details and choices related to the use of HOSM are discussed.

### 2.3.1. Running HOSM for long time in large domains

The perhaps most common way to use HOSM is to simulate relatively large ocean areas for relatively long durations (20-60 minutes, for example), and extract statistics of properties such as crest heights or wave kinematics. Often simulations are repeated many times with different random amplitudes and phases in the initial condition, which typically is chosen according to a relevant wave spectrum.

One difficulty related to using HOSM and other methods simulating waves in periodic domains in long-time simulations to extract short-time wave statistics, is that the periodic domain should ideally be large enough that the statistics are not affected by waves propagating through the domain affecting the statistical independence in the time evolution (i.e. that the autocorrelation is not strictly decreasing with increasing time-lag). Despite the computational efficiency of HOSM, this represents a computational challenge if running many simulations to obtain information about the tails of the distributions.

Moreover, when employing a breaking model that drains energy from the wave field, another difficulty of simulating over relatively long periods is that the resulting time-evolution is non-stationary since the total energy is reduced with time, breaking the typical assumption of stationary conditions over e.g. one or three-hours. One option to maintain stationarity with respect to significant wave-height, for example, is to input the energy that is lost due to wave breaking. Although this can be considered a way to model the balance between wind and breaking occurring in the real ocean, it is challenging to replace the lost energy in a realistic manner.

### 2.3.2. Running HOSM for short-duration wave events

To address some of these challenges of using HOSM for e.g. running long-term analysis of waves and wave-induced structural loads, another way to run HOSM is suggested and validation in the present work. Instead of running HOSM for a large domain, describing the full random surface of a given sea state, it is possible to simulate only relevant wave-events (typically associated with large waves occurring in the given sea state) [25]. In this case, only a short duration (e.g. one minute) associated with the large wave event is simulated. Because of the short duration, a relatively small domain size may also be used. This makes this approach very efficient and enables simulation of a very large number of events, which facilitates using HOSM in real long-term analysis of wave-induced loads, as demonstrated in [25].

#### 2.3.1. Initial condition

As initial condition, HOSM needs the initial surface elevation  $\eta(\mathbf{x}, t = 0)$  and initial surface potential  $\psi(\mathbf{x}, t = 0)$  in the computational domain. Ideally, these should be initialized according to their nonlinear relationship, expressing all bound waves correctly. If the free waves are specified (e.g. as components according to a relevant wave spectrum with random phases and amplitudes), these relations are known from second-order theory [26], and up to fourth-order in e.g. [27]. To use consistent initialization beyond second-order is however both computationally demanding for large domains (many wave components), and requires implementation of the very complicated coefficients in [27]. Therefore, linear or second-order theory is typically used. Some testing of the effect of linear vs second-order initialization has been carried out in Section 2.6.6, with the conclusion that the differences are generally quite small. However, it is still recommended to use second-order initialization for better consistency with the nonlinear evolution equations and to avoid transient start up effects (see also [28] for related discussions).

#### 2.3.2. Largest wavenumber to resolve

Probably the most challenging parameter to consistently decide in HOSM is the choice of the largest wavenumber (shortest wave) that is resolved by the simulation. While the size of the domain is typically chosen according to the problem of interest, the largest wavenumber  $k_{max}$  to resolve in the corresponding Fourier-grid can be chosen independently of the domain size. The combination of the domain-size and the maximum wavenumber then decide the number of grid points to use to discretize the surface elevation and surface potential, i.e.  $n_x = 2 \frac{x_{max}}{\lambda_p} \frac{k_{max}}{k_p}$ , where  $x_{max}$  is the size of the periodic domain and  $\lambda_p$  and  $k_p$  are the peak wavelength and peak wavenumber, respectively.

For steep waves, setting  $k_{max}$  too large, may lead to numerical instabilities, which affect the solution and the effect of the breaking model in particular. Typically, there will be stronger breaking if  $k_{max}$  is large. Some investigation of the effect of  $k_{max}$  in HOSM is presented in [29]. Typically, a maximum wavenumber in the range from  $6k_p$  to  $8k_p$  is suitable. It is found that for less steep sea states, the difference between  $k_{max} = 6k_p$  and  $k_{max} = 8k_p$  is minor.

Note that the values discussed above correspond to the grid representing the aliasing free solution. Normally, HOSM is run with full de-aliasing, such that HOSM internally uses a finer grid with corresponding maximum wavenumber  $(M - 1)k_{max}$ , where  $k_{max}$  is the maximum wavenumber of the aliasing-free solution.

### 2.3.3. Nonlinear order

Although HOSM is often referred to as a fully nonlinear model, in most applications HOSM is used with nonlinear order  $M$  between 3 and 7. At third order the dominating nonlinear modulation effects due to quasi-resonant four-wave interactions are already included. It is found (as presented in e.g. Section 2.6.4) that in simulations of realistic irregular wave fields the difference between  $M = 3$  and  $M = 5$  is quite small, and the difference between  $M = 5$  and  $M = 7$  is even smaller. Hence, in most applications it is sufficient to use  $M = 3$  or  $M = 5$ .

## 2.4. Validation of HOSM with breaking model for unidirectional simulations

In the following HOSM with the breaking model described in Section 2.2 are validated through comparison of crest-height distributions obtained from HOSM-simulations and results from model tests for 13 different long-crested sea states.

### 2.4.1. Simulation setup

The present model tests-results come from wave-flume experiments of unidirectional irregular waves generated according to JONSWAP spectra. Corresponding long-crested HOSM simulations are run for the same sea states. Here, HOSM is run with a domain  $x_{max} = 16\lambda_p$  resolving wavenumbers up to  $k_{max} = 8k_p$ , leading to a computational grid of  $n_x = 1024$  points. Note that this is for the aliasing-free solution, which means that for nonlinear order  $M = 5$  wavenumbers up to  $32k_p$  on a grid with 4096 points is used internally. Each simulation is run for a duration of 30 minutes, and crest heights are found by considering the time-series of the surface elevation in a single point. Simulation of the same sea state is repeated several times, with different random phases and amplitudes each run. The water depth in both model tests and HOSM simulations corresponds to infinite depth conditions. Due to the challenges related to decreasing energy during the simulation when breaking model is applied (i.e. non-stationary  $H_s$ ), as discussed in Section 2.3.1, here an energy-pumping scheme is used where the energy is maintained stable during the simulation. Energy is inputted uniformly over all wavenumbers.

### 2.4.2. Sensitivity of breaking-threshold

To test the sensitivity of the parameters in the breaking model, simulations were run for a range of different values for the breaking criterion  $U_c$ . As described in Section 2.2, this controls the threshold for when the local breaking-term in the equations are activated. Hence, smaller  $U_c$  leads to more waves breaking, while larger  $U_c$  gives less waves breaking.

The agreement with the model-test results were then quantified in terms of the Kolmogorov–Smirnov statistic for the difference in crest-distributions obtained from HOSM simulations and from the model tests. The results are summarized in Figure 2-1, showing that best results are obtained for  $U_c \approx 0.8 - 0.9$ , which is consistent with the experimental values reported in [18], where  $U_c = 0.85$  was suggested.

A similar study was carried out with respect to the breaking-term parameter  $\alpha$ , which was varied in the range from 0.015 to 0.025. The results were shown to be quite robust within this range, and the suggested value  $\alpha = 0.02$  was confirmed as a good choice.

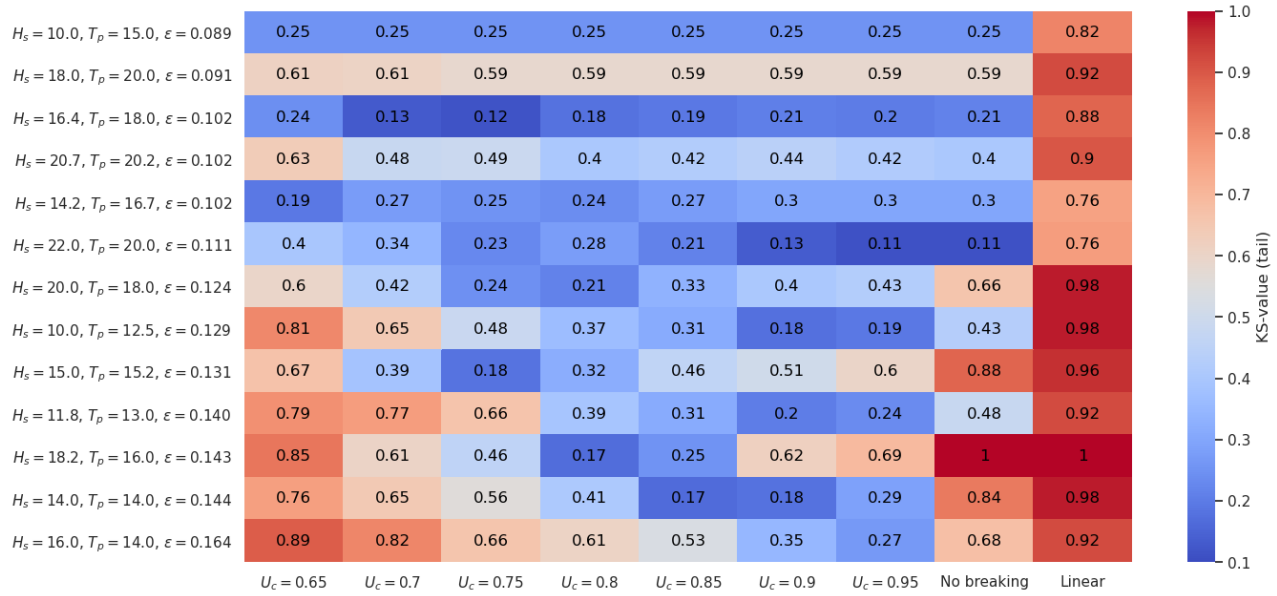


Figure 2-1 Deviation from model tests for different values of the breaking-threshold  $U_c$ , measured in terms of the Kolmogorov–Smirnov statistic for the difference in crest-distribution between HOSM-simulations and model-tests. Results from linear simulations are also included as reference. Smaller values/blue color indicates better agreement.

### 2.4.3. Crest distributions

Based on the sensitivity test discussed in the previous subsection, the breaking model was run with  $U_c = 0.85$  and  $\alpha = 0.02$  in the following. The resulting crest distributions obtained from HOSM with and without breaking model, compared to the experimental data, as well as to Rayleigh and Forristall [30] distributions for crest-heights are shown in Figure 2-2 to Figure 2-4. The sea-state parameters  $H_s$  and  $T_p$ , as well as the corresponding sea-state wave steepness  $\epsilon = H_s k_p / 2$  are indicated in each plot.

As seen from the figures, the agreement with the model-tests is quite good in all sea states when the breaking model is used. HOSM without breaking model significantly overestimates crest heights in steep sea states, highlighting the importance of modelling wave breaking in models like HOSM. Note, however, that in the less steep sea states with sea-state steepness  $\epsilon$  lower than about 0.12, the breaking model has very little effect, since very few waves exceed the breaking criterion.

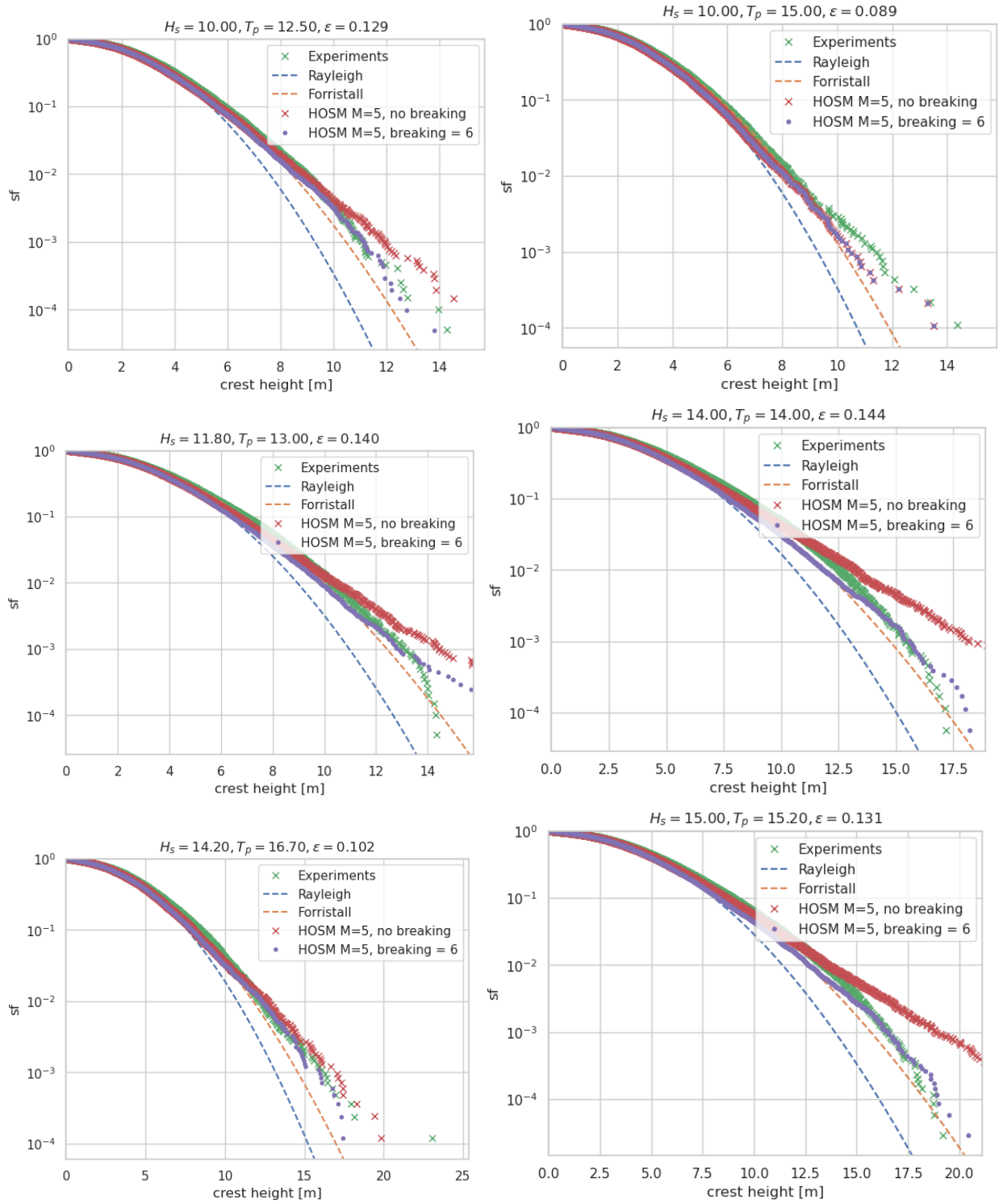


Figure 2-2 Empirical crest-distribution obtained from HOSM simulations with and without wave breaking model, compared to model-test results, as well as to common reference crest distributions.

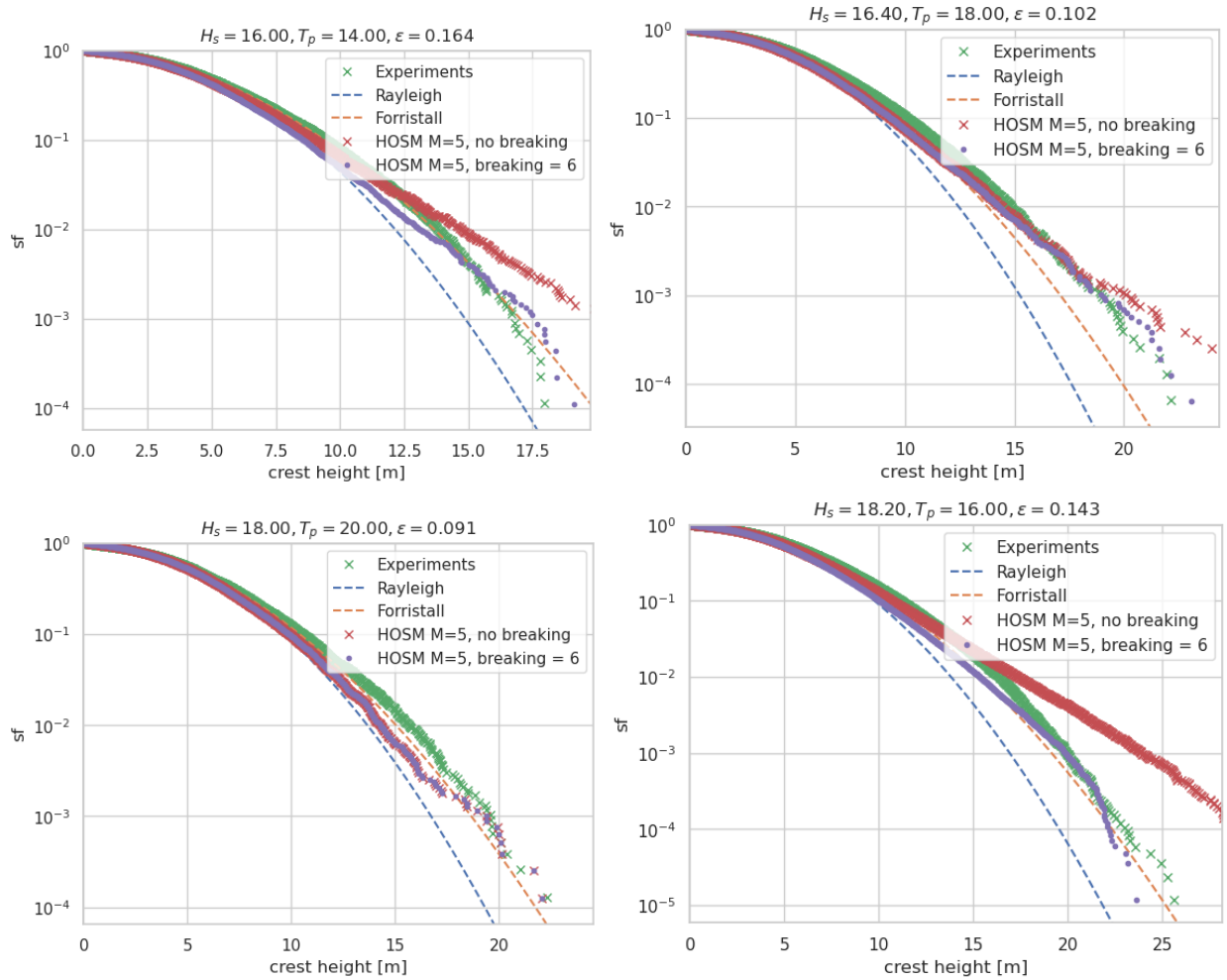


Figure 2-3 Empirical crest-distribution obtained from HOSM simulations with and without wave breaking model, compared to model-test results, as well as to common reference crest distributions.

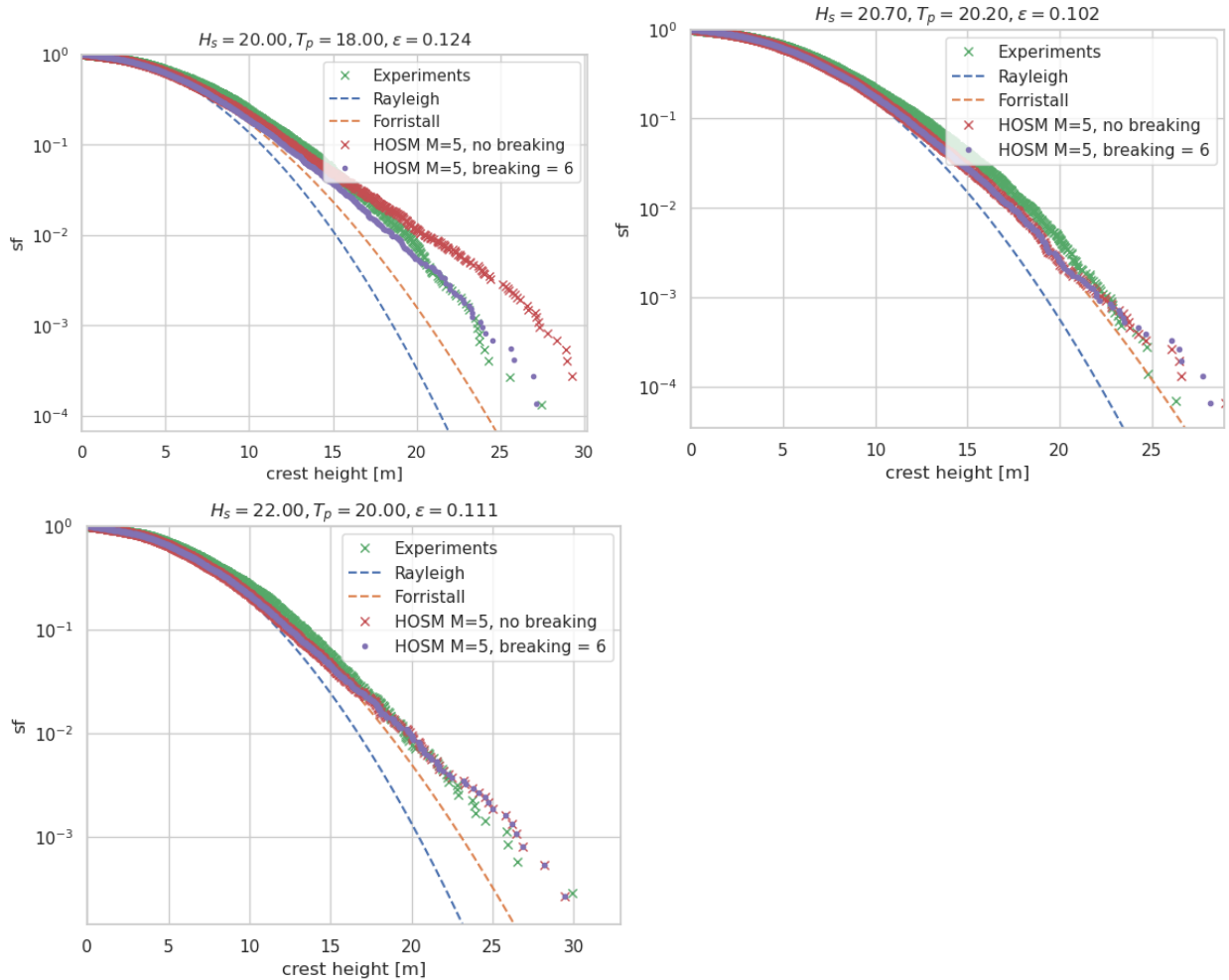


Figure 2-4 Empirical crest-distribution obtained from HOSM simulations with and without wave breaking model, compared to model-test results, as well as to common reference crest distributions.

## 2.5. Validation of HOSM with breaking model for long- and short-crested simulations using event-based approach

### 2.5.1. Event-based method

While it is feasible to run 1D-HOSM (long-crested/1D wave propagation) in long-time simulations to establish statistics of wave crests and other statistical properties, this is a demanding computational task for 2D-HOSM (short-crested/2D wave propagation), due to the considerations discussed in Section 2.3.1. Moreover, in many applications one is interested only in the tails of the distributions of wave statistical quantities.

To address these limitations in running long-term analysis of short-crested waves we have developed an event-based methodology for which HOSM is used to simulate a selection of large wave events from a sea state. The events to simulate can be identified through a linear Monte-Carlo simulation, where typically only wave-events with a sufficiently large linear crest are simulated with HOSM. Effectively, this focuses the HOSM simulation to estimate the tail of the distribution for a given sea state. More details of this methodology is given in [25].

Another advantage of this event-based methodology is that HOSM can be compared directly with more advanced wave-models such as full CFD-codes, since the small domain (typically three to six peak wavelengths in both horizontal directions) and short duration (a few peak periods) used for simulating the events allows for using computationally demanding CFD-models.

In the following subsections, the validation of this event-based methodology is presented in terms of comparison to model-test results (crest distributions) as well as deterministic and statistical comparison with CFD-simulation of the same events using the CFD-code Comflow.

## 2.5.2. Simulation setup

### 2.5.2.1. HOSM

For the event-based approach used in this section, the computational domain used to simulate each event in HOSM was  $x_{max} \times y_{max} = 6\lambda_p \times 3\lambda_p$  and the computational grid was chosen so that wavenumbers up to  $k_{max} = 6k_p$  were resolved in both directions, leading to a computational grid of  $n_x \times n_y = 72 \times 36$  points. Note, however, that for an aliasing-free solution on this grid, HOSM internally uses a finer grid with  $n_x \times n_y = 144 \times 72$  for nonlinear order  $M = 3$  and  $n_x \times n_y = 216 \times 108$  for  $M = 5$ , corresponding to maximum wavenumbers  $12k_p$  and  $18k_p$ , for  $M = 3$  and  $M = 5$ , respectively. Here HOSM has been run with nonlinear orders  $M = 3$  or  $M = 5$ , and in each case HOSM was initialized according to linear or second-order theory. The breaking model was run using the "default" parameters as suggested in the literature and previously verified for long-crested propagation (see Section 2.4.2):  $U_c = 0.85$  and  $\alpha = 0.02$ .

### 2.5.2.2. Comflow

Comflow is a one-phase volume-of-fluid code that solves the full Navier-Stokes equations, and is therefore, in principle, able to describe processes such wave-breaking directly. However, it is noted that wave breaking is a complicated process for which deterministic prediction is associated with uncertainties even in CFD codes like Comflow.

For the comparison with HOSM simulations presented in the following, Comflow and HOSM were run in one-horizontal dimension (long-crested waves). The computational grid in Comflow was set to 150 points per peak wavelength ( $n_x = 900$  over the  $6\lambda_p$ ) in the horizontal direction and 250 points per wavelength in the vertical direction for  $z > -30$  m. Two grid-refinements regions were applied so that coarser grids of half and one-quarter of the finest resolution were used for  $z < -30$  m and  $z < -80$  m, respectively. Comflow version 4.3.2 was used.

## 2.5.3. Comparison with Comflow simulations

For the following comparison of HOSM-simulation to full CFD-simulation of the same wave events, a number of events generated from eleven different sea states were considered. For each sea state, 200 events with linear crest in the origin exceeding  $H_s/2$  were simulated. Additionally, in the steepest sea state ( $H_s = 10$  m,  $T_p = 10$  s) 3859 were run, and used to estimate a crest distribution from the Comflow results. The sea-state parameters for each sea state are listed in Table 2-1. The events were generated subject to the chosen wave spectrum for each sea state (JONSWAP) and the crest height in the origin, using the event-sampling technique described in [25].

Each event was run (in both Comflow and HOSM) for a duration of  $5.5T_p$ , where  $T_p$  is the peak period of the sea state from which the relevant event was generated. The first  $1.5T_p$  of each simulation were discarded (in order to let the nonlinear simulation adjust itself from the linear or second-order initial condition), so that the last  $4T_p$  were actually used. Some testing of the sensitivity of the length of the initial adjustment period were carried out.

Table 2-1 Sea state parameters for the 11 sea states considered.

| $H_s$ [m] | $T_p$ [s] | $\epsilon$ [-] | Number of events |
|-----------|-----------|----------------|------------------|
| 10.0      | 18.0      | 0.067          | 200              |
| 15.0      | 18.3      | 0.097          | 200              |
| 14.2      | 16.7      | 0.107          | 200              |
| 17.0      | 16.6      | 0.130          | 200              |
| 15.5      | 15.8      | 0.129          | 200              |
| 10.0      | 12.5      | 0.129          | 200              |
| 11.8      | 13.0      | 0.141          | 200              |
| 18.2      | 16.0      | 0.148          | 200              |
| 14.0      | 14.0      | 0.145          | 200              |
| 16.0      | 14.0      | 0.166          | 200              |
| 10.0      | 10.0      | 0.201          | 3859             |

For each event, the resulting wave evolutions in HOSM and Comflow were compared in terms of the following parameters:

- The maximum wave-crest in the origin during the  $4T_p$  event period.
- The horizontal fluid velocity squared, integrated over the water-column from bottom to still water level, at the time and position of the largest crest
- The horizontal fluid velocity squared, integrated over the water-column from still water level to the surface, at the time and position of the largest crest

The quantities (b) and (c), representative for e.g. drag loads on a vertical structure, can be written in the following form

$$I_{u^2}^{(bot)} = \int_{-h}^0 u^2 dz, \quad I_{u^2}^{(top)} = \int_0^{\eta} u^2 dz.$$

Relevant for the kinematics below and above mean water level, respectively.

The results of this comparison are shown in Figure 2-5, Figure 2-6 and Figure 2-7, showing for each event the values obtained from HOSM versus the ones from Comflow. Corresponding QQ-plots, giving information about the overall distribution of these quantities are also shown. It is evident that both for crest



heights and for kinematics below mean water level the agreement is very good for less steep sea states, with somewhat more scatter for the steepest sea states, but still with a reasonable agreement, in particular if considering the resulting distribution from many events (QQ-plots). It is worth to note that overall HOSM is conservative (gives higher values) in all cases. For  $I_{u_2}^{(bot)}$  HOSM is in some sea states (in particular  $H_s = 17.0$  m,  $T_p = 16.6$  s) consistently above the Comflow results, without any apparent explanation for this deviation.

For  $I_{u_2}^{(top)}$ , relevant for wave kinematics in the crest of large (and possibly breaking) waves, Figure 2-7 shows that the agreement is still quite good in the least steep sea states, but the deterministic agreement is relatively poor in steep sea states. This may be expected since the HOSM is not able to describe the actual breaking process of the waves correctly. It is interesting to note, however, that HOSM results are conservative in the steeper sea states.

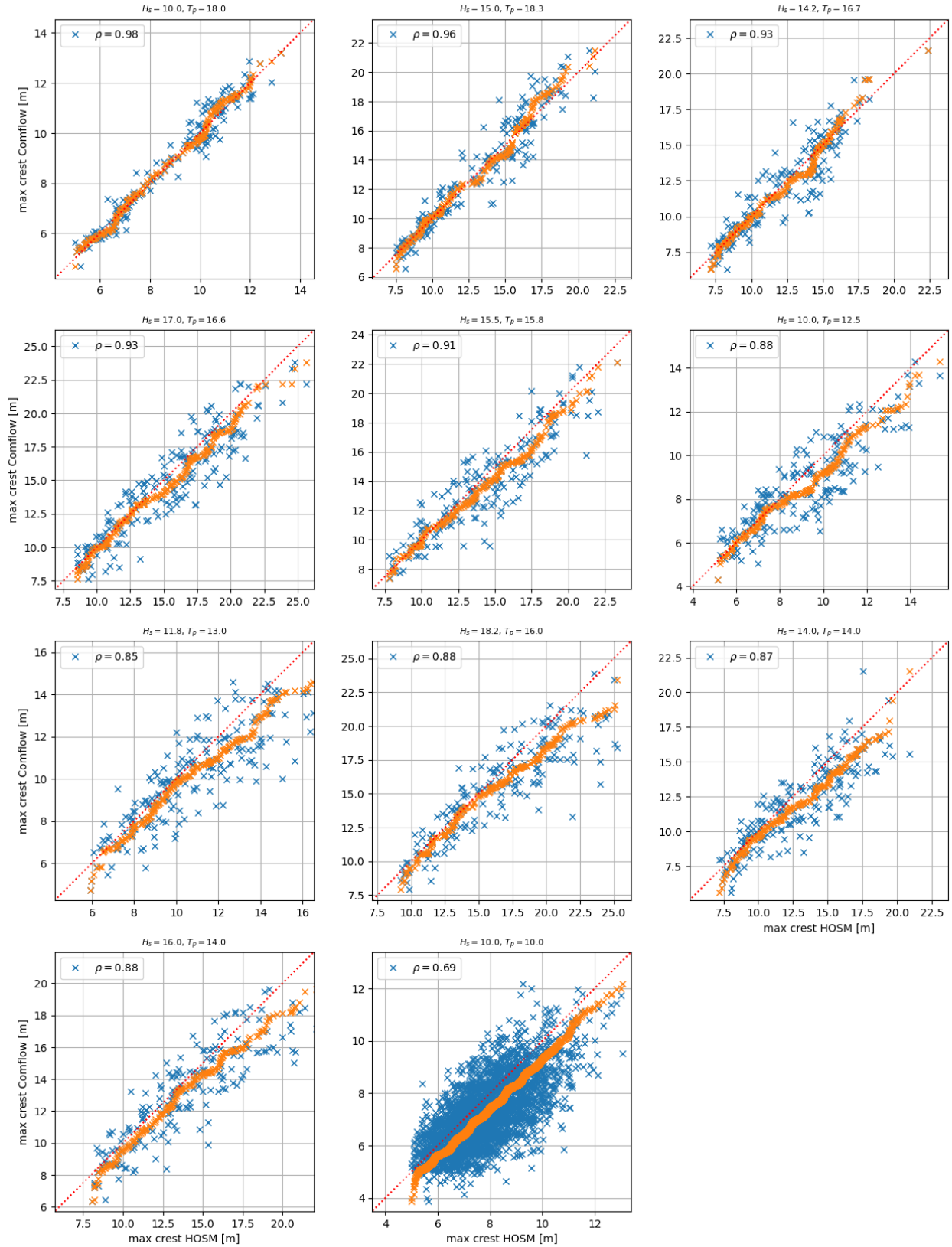


Figure 2-5 Maximum crest in unidirectional Comflow and HOSM simulations of the same event (blue) and corresponding QQ-plot (orange). Linear (Pearson) correlation coefficient between HOSM and Comflow results are shown in legend.

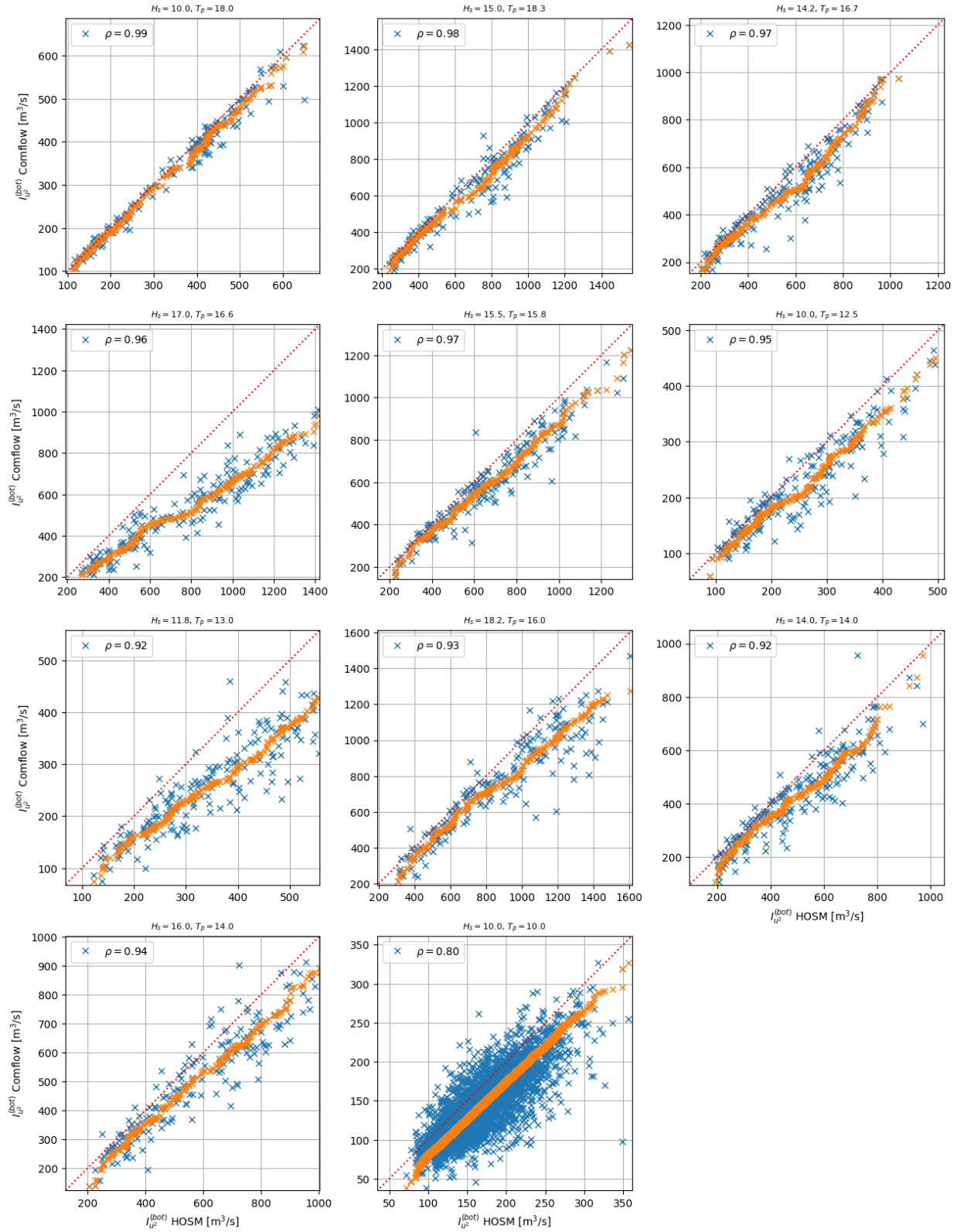


Figure 2-6  $I_{u_2}^{(bot)}$  at time of maximum crest in unidirectional Comflow and HOSM simulations of the same event (blue) and corresponding QQ-plot (orange). Linear (Pearson) correlation coefficient between HOSM and Comflow results are shown in legend.

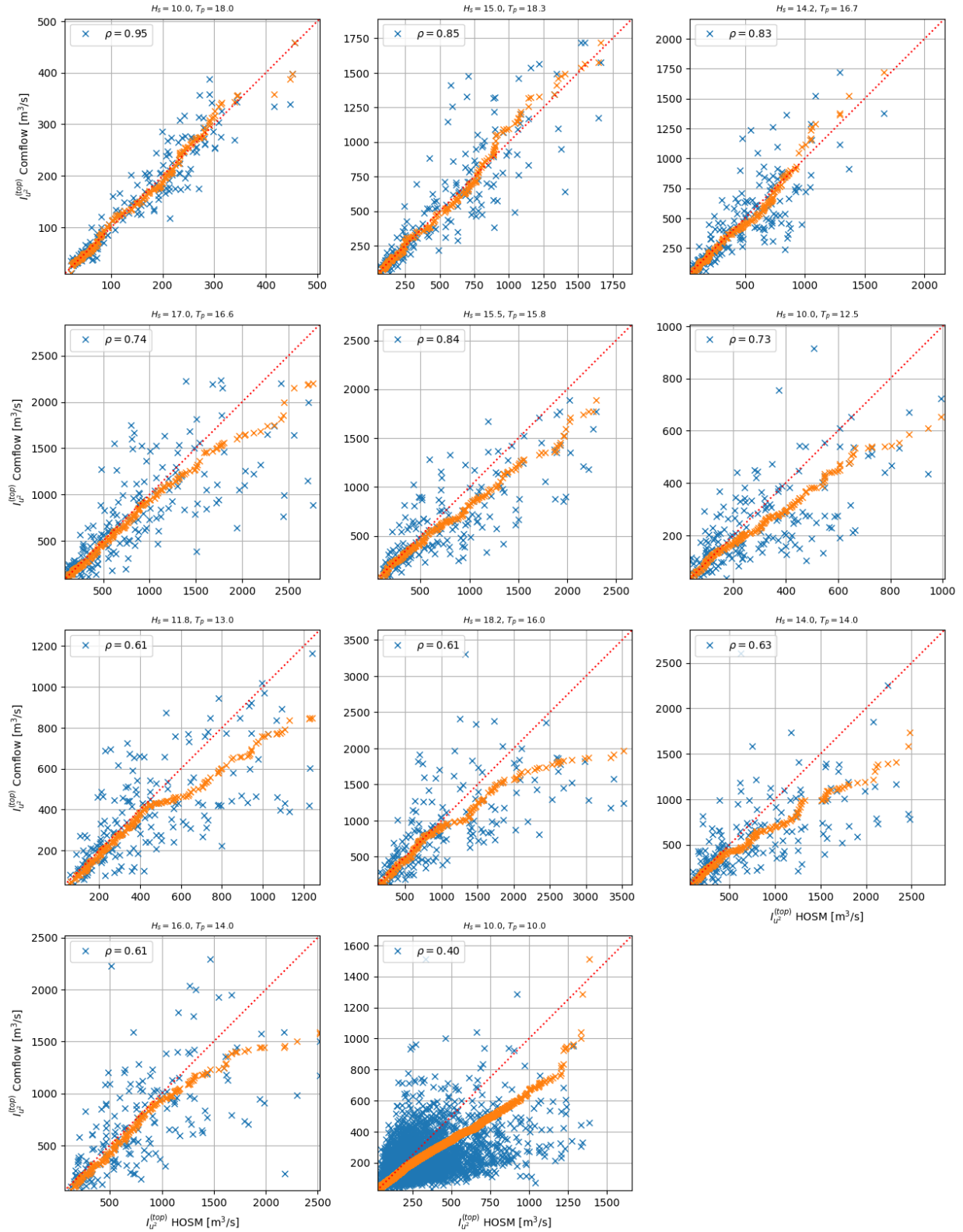


Figure 2-7  $I_{u_2}^{(top)}$  at time of maximum crest in unidirectional Comflow and HOSM simulations of the same event (blue) and corresponding QQ-plot (orange). Linear (Pearson) correlation coefficient between HOSM and Comflow results are shown in legend.

#### 2.5.4. Crest distributions

To further validate HOSM and the implemented wave-breaking model, as well as the event-based approach we have here used HOSM to estimate crest distributions for the 11 sea states listed in Table 2-1, for which we also have access to model-test results, providing empirical crest distributions.

To estimate crest distributions using HOSM in the event-based approach, first a linear time-domain simulation of duration 1 000 hours was carried out for each of the 11 sea states. Then, each time a crest exceeding  $H_s/2$  were encountered, a short-crested linear event with the same crest-height was sampled using the event-sampling method described in [25]. Finally, all these events were simulated in HOSM using the computational setup described in Section 2.5.2.1. Then, from the resulting HOSM-results, distribution of wave crests was estimated. However, since only events having linear crest above  $H_s/2$  we considered, this approach estimates only the tails of the crest distributions.

Estimated crest distributions from HOSM and model tests are shown in Figure 2-8. Reference distributions based on linear (Rayleigh) and second-order (Forristall [30]) theories as well as the recent crest distribution suggested in the Loads JIP [31] are included (Loads-OCG in the figure). The Loads distribution includes the effect of wave breaking, as clearly observed for the steepest sea state ( $H_s = 10$  m,  $T_p = 10$  s) in Figure 2-8.

It is seen from the figure that HOSM predicts crest-distribution is good agreement with the model-tests results in most sea states. Note that it is in good agreement with both model tests and the Loads crest distribution that includes wave breaking for the steep sea states. This clearly confirms the usefulness and validity of the wave-breaking model, also for short-crested simulations.

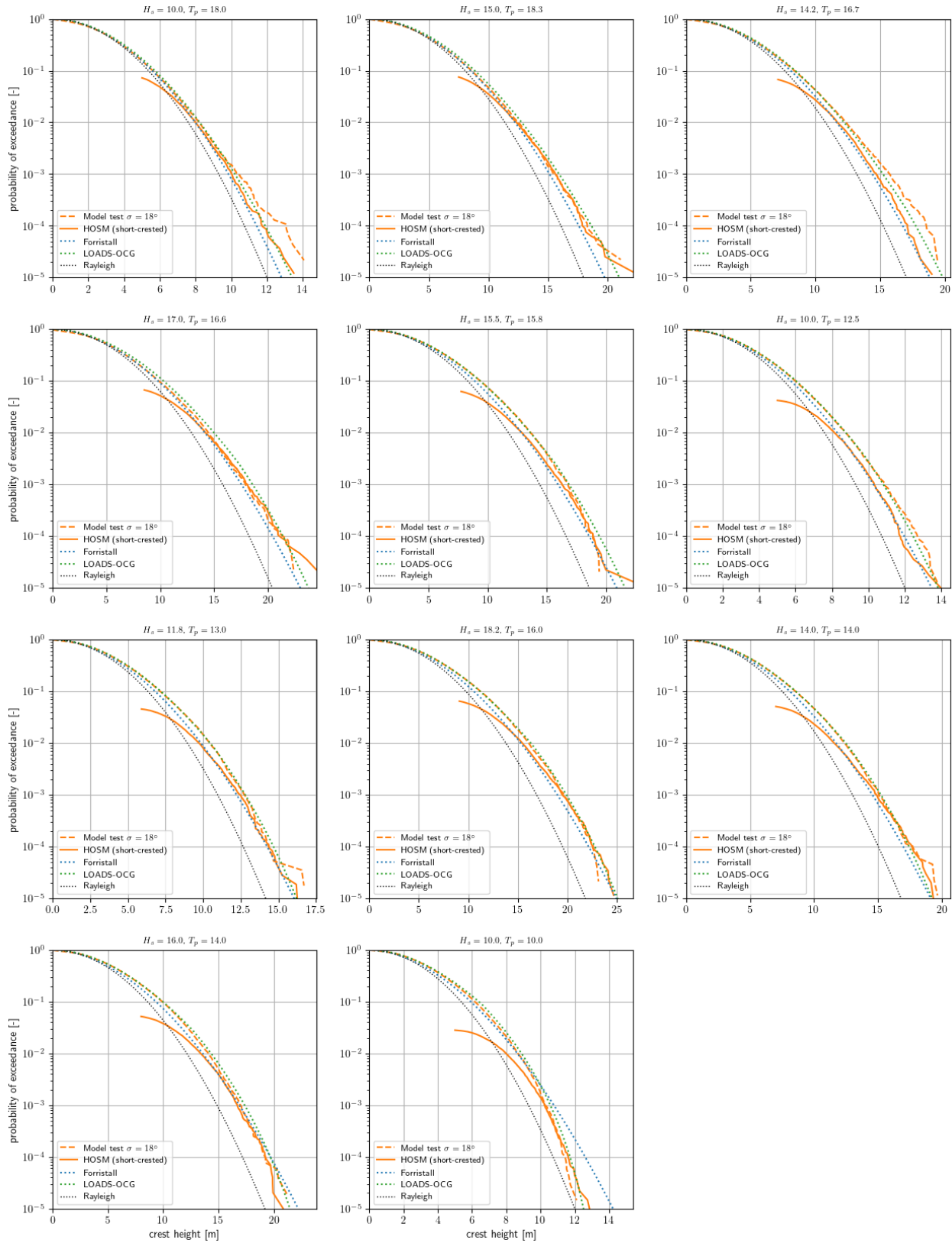


Figure 2-8 Crest distributions from HOSM simulation and model-tests compared with Forristall [30] and Rayleigh crest-distributions.

## 2.6. Simulation of Teesside and Brittany sea states

In the following section, a detailed investigation is carried out for four selected sea states relevant for the Hiperwind project. Two geographical locations are considered: The south French Brittany and the Teesside site (UK). For each site, two sea-state conditions, are considered: one relevant for fatigue and one extreme sea state.

### 2.6.1. Sea states and environmental conditions

Two sea states are selected on each of the geographical locations, depending on the obtained scatter diagrams and the different most severe load cases for different criteria. The aim is to select a severe and a short-wave case, that would be more common in the lifetime of the structure, for each location. We describe here those four selected cases. A summary is given in section 2.6.1.3, Table 2-3.

#### 2.6.1.1. French Brittany: deep water floating platform.

The selected case that will be studied as an example of a case of tempest is of peak period  $T_p = 16.5$  s and significant wave height  $H_s = 12.5$  m, representative of a 50-y storm on this site. The linear dispersion relation yields a peak wavelength of  $\lambda_p = 411$  m, not validating the hypothesis of infinite water depth ( $h/\lambda_p = 0.36$ ), for the peak period with  $h$  the water depth (here  $h = 150$  m). The peak factor  $\gamma$  is selected from the recommendations of [32]:  $\gamma = 1.46$ . This case will be denoted Brittany Severe (BS).

To select a case that is representative of the fatigue load, we combine the site  $H_s$ - $T_p$  scatter diagram with the Response Amplitude Operator (RAO) of the floater, given by Nemoh [33]. In practice, we compute a quantity representative on an equivalent fatigue damage of a given sea state ( $H_s, T_p$ ), denoted  $D(H_s, T_p)$ :

$$D(H_s, T_p) = \frac{p(H_s, T_p)RAO(T_p)}{T_p} \quad (1)$$

where  $p(H_s, T_p)$  is the probability density of occurrence, given by the scatter diagram. Computed values of  $D$  from the scatter diagrams are given in Table 2-2.

Table 2-2. Equivalent damage  $D(H_s, T_p)$  induced by a given state. First row is the RAO at the considered period (second row). The selected case is  $H_s = 2.5$  m and  $T_p = 6.5$  s.

| RAO( $T_p$ )      | 2061100  | 1676970  | 1469820  | 5797960  | 5954800  | 4938060  | 4401020  | 4636960  | 4828360  | 4795880  | 4509560  | 4266015  | 4022470  | 3732730  | 3442990  | 3442990  | 3145495  | 2996747,5 | 2848000  | 2848000  |          |          |
|-------------------|----------|----------|----------|----------|----------|----------|----------|----------|----------|----------|----------|----------|----------|----------|----------|----------|----------|-----------|----------|----------|----------|----------|
| $H_s(m) / T_p(s)$ | 3,50E+00 | 4,50E+00 | 5,50E+00 | 6,50E+00 | 7,50E+00 | 8,50E+00 | 9,50E+00 | 1,05E+01 | 1,15E+01 | 1,25E+01 | 1,35E+01 | 1,45E+01 | 1,55E+01 | 1,65E+01 | 1,75E+01 | 1,85E+01 | 1,95E+01 | 2,05E+01  | 2,15E+01 | 2,25E+01 | SUM      |          |
| 5,00E-01          | 3,75E+04 | 1,65E+05 | 1,26E+05 | 4,94E+05 | 6,96E+05 | 6,82E+05 | 3,57E+05 | 1,80E+05 | 6,16E+04 | 2,94E+04 | 1,92E+04 | 7,33E+03 | 1,67E+03 | 5,20E+02 | 7,23E+01 | 3,42E+01 | 0,00E+00 | 0,00E+00  | 0,00E+00 | 0,00E+00 | 0,00E+00 | 2,86E+06 |
| 1,50E+00          | 6,66E+03 | 6,00E+05 | 1,79E+05 | 7,01E+05 | 4,78E+06 | 4,96E+06 | 4,36E+06 | 3,08E+06 | 1,66E+06 | 7,03E+05 | 2,50E+05 | 6,82E+04 | 1,65E+04 | 5,26E+03 | 1,44E+03 | 0,00E+00 | 0,00E+00 | 0,00E+00  | 0,00E+00 | 0,00E+00 | 0,00E+00 | 3,11E+07 |
| 2,50E+00          | 0,00E+00 | 3,42E+02 | 1,08E+03 | 5,19E+06 | 2,29E+06 | 2,92E+06 | 2,57E+06 | 2,85E+06 | 4,20E+06 | 4,38E+06 | 2,90E+06 | 9,55E+05 | 1,90E+05 | 4,82E+04 | 1,17E+04 | 1,37E+03 | 1,04E+03 | 0,00E+00  | 0,00E+00 | 0,00E+00 | 0,00E+00 | 3,06E+07 |
| 3,50E+00          | 0,00E+00 | 0,00E+00 | 0,00E+00 | 0,00E+00 | 1,74E+06 | 1,69E+06 | 1,87E+06 | 1,90E+06 | 2,00E+06 | 2,62E+06 | 2,94E+06 | 1,95E+06 | 5,80E+05 | 9,79E+04 | 1,19E+04 | 1,08E+03 | 7,26E+02 | 0,00E+00  | 0,00E+00 | 0,00E+00 | 0,00E+00 | 1,75E+07 |
| 4,50E+00          | 0,00E+00 | 0,00E+00 | 0,00E+00 | 0,00E+00 | 5,32E+04 | 3,91E+05 | 8,55E+05 | 1,43E+06 | 1,46E+06 | 1,40E+06 | 1,50E+06 | 1,29E+06 | 6,89E+05 | 2,15E+05 | 2,77E+04 | 5,08E+03 | 1,33E+02 | 0,00E+00  | 0,00E+00 | 0,00E+00 | 0,00E+00 | 9,32E+06 |
| 5,50E+00          | 0,00E+00 | 0,00E+00 | 0,00E+00 | 0,00E+00 | 0,00E+00 | 1,70E+04 | 1,25E+05 | 5,82E+05 | 1,10E+06 | 9,96E+05 | 9,52E+05 | 7,37E+05 | 3,93E+05 | 9,92E+04 | 3,60E+04 | 7,15E+03 | 2,61E+03 | 1,48E+02  | 4,02E+02 | 0,00E+00 | 0,00E+00 | 5,04E+06 |
| 6,50E+00          | 0,00E+00 | 0,00E+00 | 0,00E+00 | 0,00E+00 | 0,00E+00 | 0,00E+00 | 6,09E+03 | 9,86E+04 | 4,66E+05 | 6,70E+05 | 6,79E+05 | 5,20E+05 | 2,89E+05 | 9,11E+04 | 2,07E+04 | 3,33E+03 | 1,54E+03 | 0,00E+00  | 0,00E+00 | 0,00E+00 | 0,00E+00 | 2,85E+06 |
| 7,50E+00          | 0,00E+00 | 0,00E+00 | 0,00E+00 | 0,00E+00 | 0,00E+00 | 0,00E+00 | 6,38E+02 | 4,87E+03 | 8,91E+04 | 3,42E+05 | 4,31E+05 | 3,15E+05 | 1,54E+05 | 4,40E+04 | 1,03E+04 | 3,08E+03 | 2,89E+03 | 0,00E+00  | 3,65E+02 | 0,00E+00 | 0,00E+00 | 1,40E+06 |
| 8,50E+00          | 0,00E+00 | 6,90E+02 | 1,18E+04 | 7,91E+04 | 1,99E+05 | 2,15E+05 | 7,74E+04 | 2,47E+04 | 9,22E+03 | 3,20E+03 | 1,26E+03 | 6,85E+02  | 0,00E+00 | 0,00E+00 | 0,00E+00 | 6,22E+05 |
| 9,50E+00          | 0,00E+00 | 7,33E+02 | 1,67E+04 | 1,05E+05 | 8,58E+04 | 6,48E+04 | 2,17E+04 | 9,62E+03 | 0,00E+00 | 5,63E+02 | 2,30E+03  | 0,00E+00 | 0,00E+00 | 0,00E+00 | 3,07E+05 |
| 1,05E+01          | 0,00E+00 | 1,48E+03 | 1,74E+04 | 3,97E+04 | 3,30E+04 | 1,92E+04 | 2,28E+03 | 0,00E+00 | 0,00E+00 | 0,00E+00  | 0,00E+00 | 0,00E+00 | 0,00E+00 | 1,13E+05 |
| 1,15E+01          | 0,00E+00 | 2,12E+03 | 8,70E+03 | 2,52E+04 | 6,69E+03 | 0,00E+00 | 0,00E+00 | 0,00E+00  | 0,00E+00 | 0,00E+00 | 0,00E+00 | 4,27E+04 |
| 1,25E+01          | 0,00E+00 | 1,53E+03 | 6,08E+03 | 3,58E+03 | 5,72E+03 | 0,00E+00 | 0,00E+00 | 0,00E+00  | 0,00E+00 | 0,00E+00 | 0,00E+00 | 1,69E+04 |
| 1,35E+01          | 0,00E+00 | 2,19E+03 | 1,29E+03 | 0,00E+00 | 0,00E+00 | 0,00E+00 | 0,00E+00 | 0,00E+00  | 0,00E+00 | 0,00E+00 | 0,00E+00 | 3,48E+03 |
| 1,45E+01          | 0,00E+00  | 0,00E+00 | 0,00E+00 | 0,00E+00 | 0,00E+00 |
| 1,55E+01          | 0,00E+00  | 0,00E+00 | 0,00E+00 | 0,00E+00 | 0,00E+00 |
| SUM               | 4,42E+04 | 7,65E+05 | 2,02E+06 | 1,05E+07 | 1,08E+07 | 1,05E+07 | 1,07E+07 | 1,14E+07 | 1,25E+07 | 1,22E+07 | 1,05E+07 | 6,38E+06 | 2,57E+06 | 6,90E+05 | 1,45E+05 | 2,58E+04 | 1,08E+04 | 3,13E+03  | 1,24E+03 | 0,00E+00 | 0,00E+00 | 1,02E+08 |

The selected case corresponds to the highest value of  $D$  detected, *i.e.*,  $H_s = 2.5$  m and  $T_p = 6.5$  s. The peak factor has been classically selected at 3, while the DNV standard formula [32] yields 2.77.

#### 2.6.1.2. Teesside: shallow water monopile foundation.

For the storm case, we base our selection on [34], table 2-5. The 50-years return period is chosen with a water depth of 17 m: This corresponds to a low tide at large LAT or to a high time in regions with the

shallowest waters. We also select  $H_s = 10$  m and  $T_p = 15$  s. Note that this selection is very close to the “Severe case” selected on the report (table 2-12).

We apply the same methodology as in the previous section to select our “Fatigue” case: the “equivalent damage” over a lifetime is approximated by (1). The RAO are computed for a vertical circular cylinder that extend from the sea bottom to the free surface. We finally selected a sea state that both exhibit a high value of  $D(H_s, T_p)$ , but also with a similar value of  $H_s/\lambda_p$  as the Brittany Fatigue case. This way, the main observed difference will be due to the shallow water depth ( $h/\lambda_p$ ). The selected sea state is characterized by  $(H_s, T_p) = (2$  m, 15 s), for a peak steepness of 3.7% and a water depth relative to the peak wavelength of approximately 0.31. The peak factor is kept constant compared to the other “Fatigue” case, i.e.,  $\gamma = 3$ .

### 2.6.1.3. Summary of the selected cases

The sea state parameters for the four considered case are summarized in Table 2-3. The three first sea states in Table 2-3 (BF, BS and TF) are moderately steep sea states in relatively deep water (BF is essentially infinite depth). According to the validation and testing of the wave breaking model presented in Section 2.4 and Section 2.5, it is expected that these sea states are not significantly affected by wave breaking, and HOSM may be a suitable model even without wave breaking model (this is further confirmed/discussed in the subsections below).

The extreme sea state for the Teesside site (TS), however, is a quite extreme sea state in quite shallow water, in which wave breaking is expected to play an important role. Moreover, simplified theories such as linear and second-order theories are expected to be invalid in this regime.

In the following these four sea states are simulated using HOSM in an event-based simulation to investigate crest height statistics, where focus is to evaluate the effect of various modelling choices related to wave breaking, nonlinear order, directionality, and initialization method. The different results are compared to the relevant reference distributions representing linear theory (Rayleigh distribution and second-order theory (Forristall distribution [30]) as well the recent crest distribution suggested in the Loads JIP, which aims to incorporate effects of both shallow water effects, wave breaking as well as the effect of directional spreading [31].

Table 2-3 Parameters of the sea states considered in this study. Here  $\gamma$  refers to the peak-enhancement parameter of the JONSWAP spectrum, and  $k_p$  and  $\lambda_p$  are calculated from the peak period  $T_p$  using the linear dispersion relation.

|                              | $H_s$ [m] | $T_p$ [s] | $\gamma$ [-] | $h$ [m] | $\lambda_p$ [m] | $k_p h$ [-] | $H_s/h$ [-] | $H_s k_p/2$ [-] |
|------------------------------|-----------|-----------|--------------|---------|-----------------|-------------|-------------|-----------------|
| <b>Brittany Fatigue (BF)</b> | 2.5       | 6.5       | 3.00         | 150     | 66.0            | 14.29       | 0.017       | 0.119           |
| <b>Brittany Severe (BS)</b>  | 12.5      | 16.5      | 1.46         | 150     | 416.0           | 2.27        | 0.083       | 0.094           |
| <b>Teesside Fatigue (TF)</b> | 2.0       | 6.0       | 3.00         | 17      | 54.1            | 1.97        | 0.118       | 0.116           |
| <b>Teesside Severe (TS)</b>  | 10.0      | 15.0      | 1.34         | 17      | 183.9           | 0.58        | 0.588       | 0.171           |

### 2.6.2. Simulation setup

In the following HOSM is used in the event-based approach described in Section 2.5.1 using the same simulation setup as described in Section 2.5.2.1.

Each sea state is simulated for a total duration of 1 000 hours, and the results are presented in terms of the distribution of hourly-maximum crest height. The cut-off threshold on linear crest height employed in the

event-selection was set to  $H_s/4$ , which is sufficiently low to obtain a good estimate of the entire distribution of hourly maximum crest heights.

### 2.6.3. Long-crested simulations

In the case of purely unidirectional waves, HOSM was run in a one-dimensional domain, and the initial conditions were generated from a JONSWAP spectrum using the parameters in Table 2-3. Initialization according to second-order theory [26], [27] was employed for the BF, BS and TF cases, while linear initialization was used for the TS case because this sea state is outside the validity-range of second-order theory. The effects of linear versus second-order initialization are briefly discussed in Section 2.6.6.

Two different nonlinear orders ( $M = 3$  and  $M = 5$ ), with and without breaking model (breaking = True and breaking = False) were considered in each case. Resulting distributions of hourly maximum crest height are shown in Figure 2-9.

It is observed that for the three moderately severe sea states (BF, BS and TF) the breaking model has minor effect, although small differences are observed for BF and TF. This is very consistent with results in Section 2.4, showing that breaking model is not important for sea state steepness  $H_s k_p / 2 < 0.12$ . Also the difference between nonlinear order  $M = 3$  and  $M = 5$  is small for these three sea states. It should however be noted that in both the BF and TF sea states, the crest statistics from HOSM are clearly above results from e.g. Forristall distribution. This is expected in unidirectional simulations due to well-known effects of modulational instability [35], as also well documented in numerous experimental and numerical studies (see e.g. [36]).

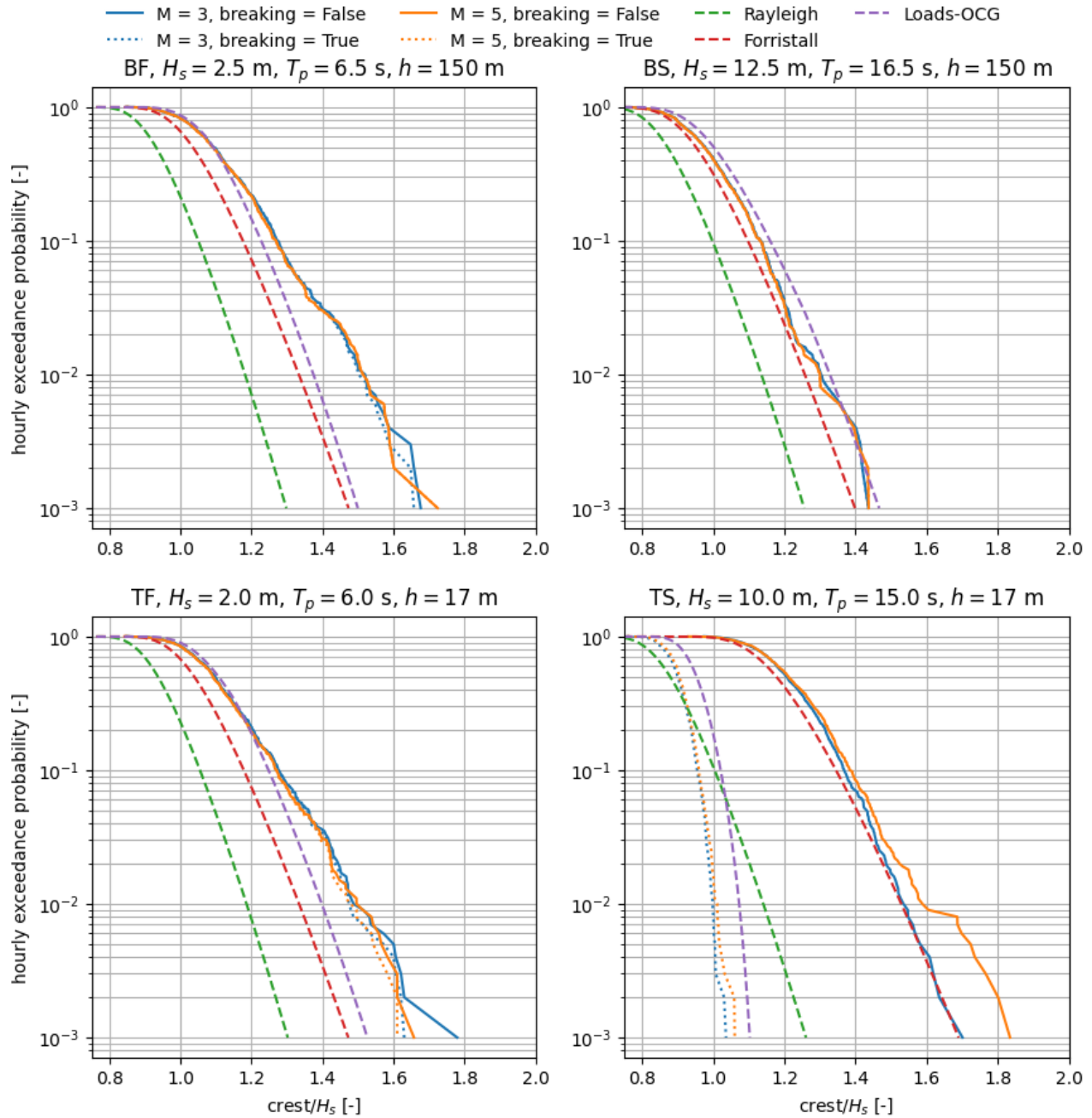


Figure 2-9 Estimated distributions of hourly maximum crest heights from long-crested HOSM simulations, compared to relevant reference distributions.

For the TS sea state (lower right subplot in Figure 2-9), there are large differences between runs with and without breaking model. There are also clear differences between runs with nonlinear order  $M = 3$  and  $M = 5$ , in particular in the tail of the crest distribution. It is quite clear that the results without wave-breaking model cannot be trusted in this case. Neither can the Forristall distribution, as this is clearly outside the validity region for second-order theory and does not incorporate wave breaking. The HOSM-results with breaking model seem more reasonable, but underestimates crest heights compared to the Loads-OCG

crest distribution (this is consistent with the effect of directional spreading observed for the short-crested simulations in Figure 2-11).

#### 2.6.4. Short-crested simulations

To extend the results presented in Section 2.6.3 to include effects of wave directionality, corresponding simulations as described in Section 2.6.3 are performed using simulation of short-crested wave events. The events were sampled from a JONSWAP spectrum with parameters according to Table 2-3, with a directional distribution of the  $\cos^N(\theta)$  type (see e.g. [36]). Here  $N = 10$  was used, which corresponds to a directional spreading of about 17 degrees. The effect of the directional distribution is further investigated in Section 2.6.5.

The estimated distributions of hourly maximum crest heights from the short-crested simulations are shown in Figure 2-10. First, we note that the result observed for the long-crested simulations that the effects of breaking model and nonlinear are minor in the three moderate sea states (BF, BS and TF), is also valid for the short-crested case. However, it is noted that the significant deviation from the Forristall distribution that was observed in the long-crested simulations, is not reproduced in the short-crested simulations. This is expected since effects of modulational instability is significantly suppressed by directional spreading, as shown in numerous theoretical, experimental and numerical studies (see e.g. [37], [38], [12], [39]). Overall, the crest statistics in these moderate sea states are in good agreement with the Forristall and Loads-OCG crest distributions.

For the TS sea state (lower right subplot in Figure 2-10), there is (as for the unidirectional case) a major difference between results with and without breaking model. It is noticed that HOSM with breaking model is in remarkable good agreement with the Loads-OCG crest distribution, which includes effects of breaking and shallow water.

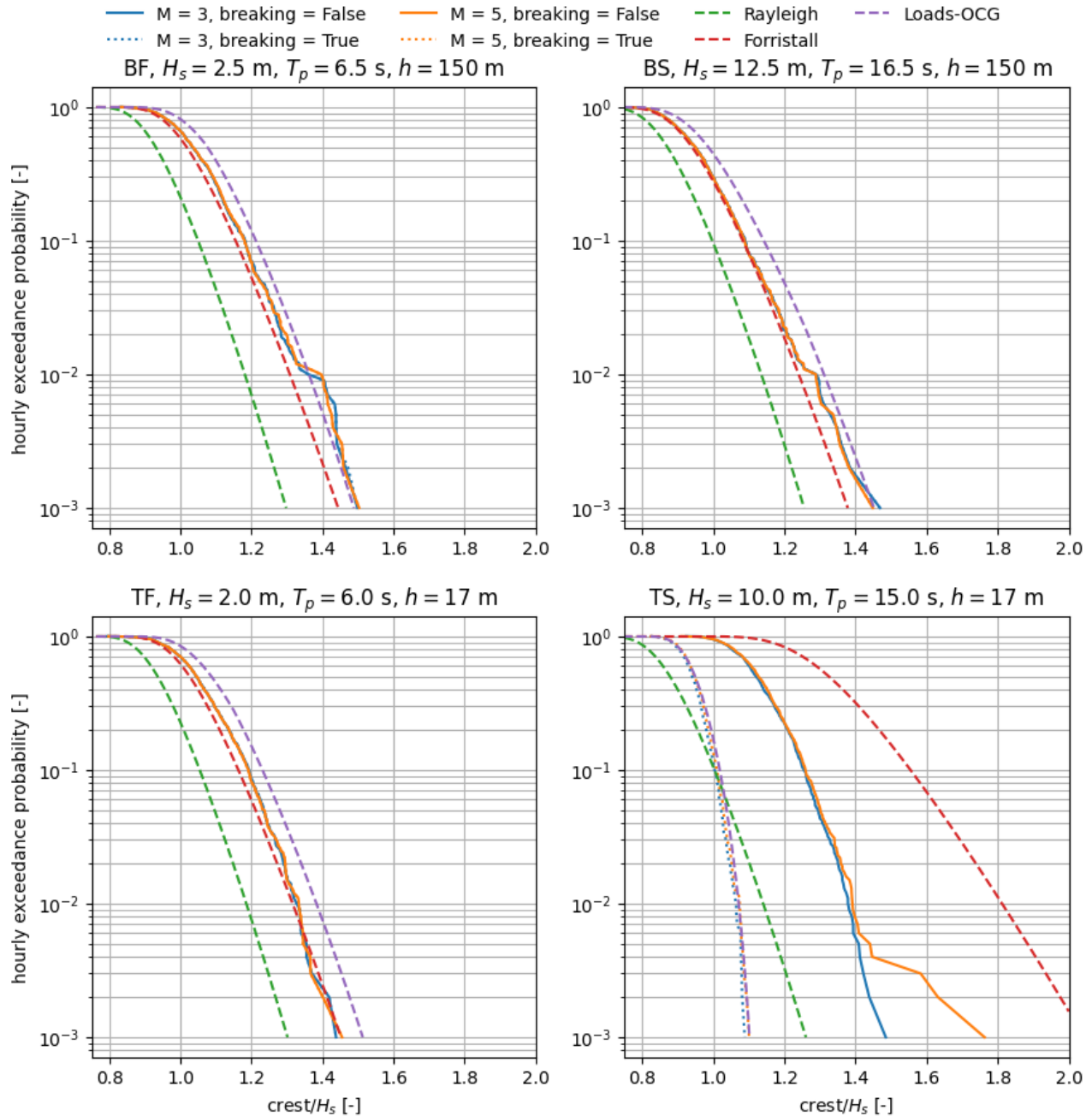


Figure 2-10 Estimated distributions of hourly maximum crest heights from short-crested HOSM simulations, compared to relevant reference distributions.

### 2.6.5. Effect of directional spreading

To further investigate the effect of the directional distribution on the results, the short-crested simulation described in Section 2.6.4 were repeated with three different directional spreading parameters in the  $\cos^N(\theta)$  type directional distribution:  $N = 2$ ,  $N = 10$  and  $N = 40$ , corresponding to a directional

spreading of  $\sigma_\theta = 31.5^\circ$ ,  $\sigma_\theta = 17.1^\circ$  and  $\sigma_\theta = 8.9^\circ$ , respectively. Here, HOSM was run using nonlinear order  $M = 3$  and with breaking model.

The resulting crest-distributions are shown in Figure 2-11. It is noted that for the BF, BS and TF cases, the effect of the directional spreading is moderate. However, the narrowest spreading yields somewhat larger crests, consistent with the effect of increased modulational instability with more narrow directional spreading, as also observed in the purely unidirectional simulations. For the BF case, the broadest directional spreading ( $N = 2$ ) gives somewhat larger crests than the two narrower cases. The reason for this is not clear, but it may be mainly due to statistical variability, but to investigate this further, the analysis should be extended beyond 1 000 hours.

For the shallow-water case (TS), the influence of the directionality is much stronger, with the effect that wave crests are larger with increased directional spreading. This is expected since the effect of wave breaking is reduced in more directional spread wave fields in shallow water.

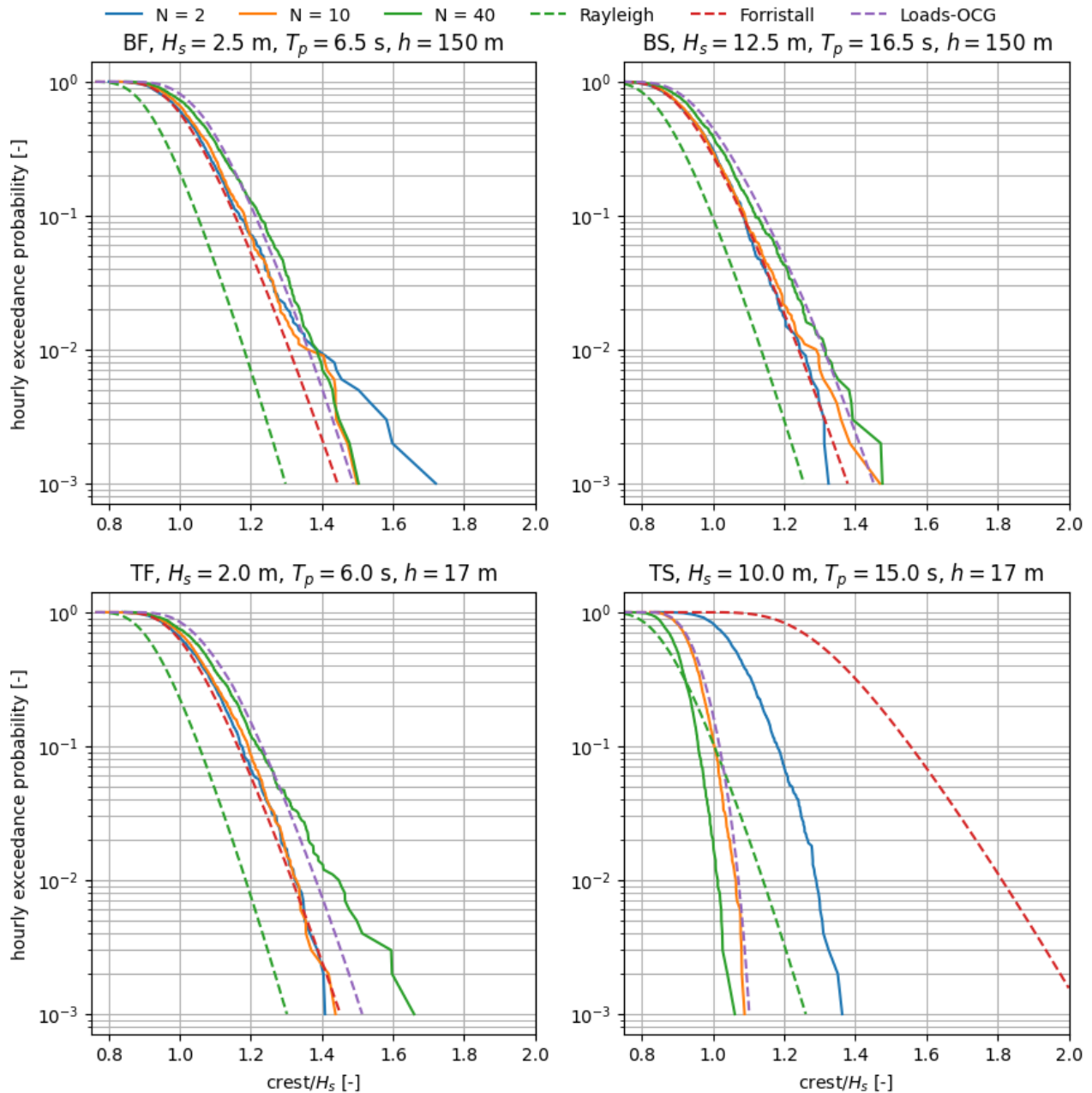


Figure 2-11 Estimated distributions of hourly maximum crest heights from short-crested HOSM simulations with three different directional spreading parameters.

## 2.6.6. Effect of second order versus linear initialization

As discussed in Section 2.3.1, it is in principle preferred to initialize HOSM with surface elevation and surface potential according to their nonlinear relationships (that is, the canonical transformation [27] expressing bound waves in terms of the free waves). In practice it is troublesome to do this initialization beyond second order. To investigate the sensitivity of the results with respect to whether linear or second-order initialization is used, the short crested runs described in Section 2.6.4, were repeated (nonlinear order

$M = 3$  with breaking model was used) using both linear and second-order initial condition in HOSM. The resulting crests distributions are shown in Figure 2-12, showing that the effect of the choice of initialization is relatively small, but still with some underestimation if linear initialization is used. In the TS-case the results should be taken with some scepticism since the validity of the second-order expansion is questionable in this case.

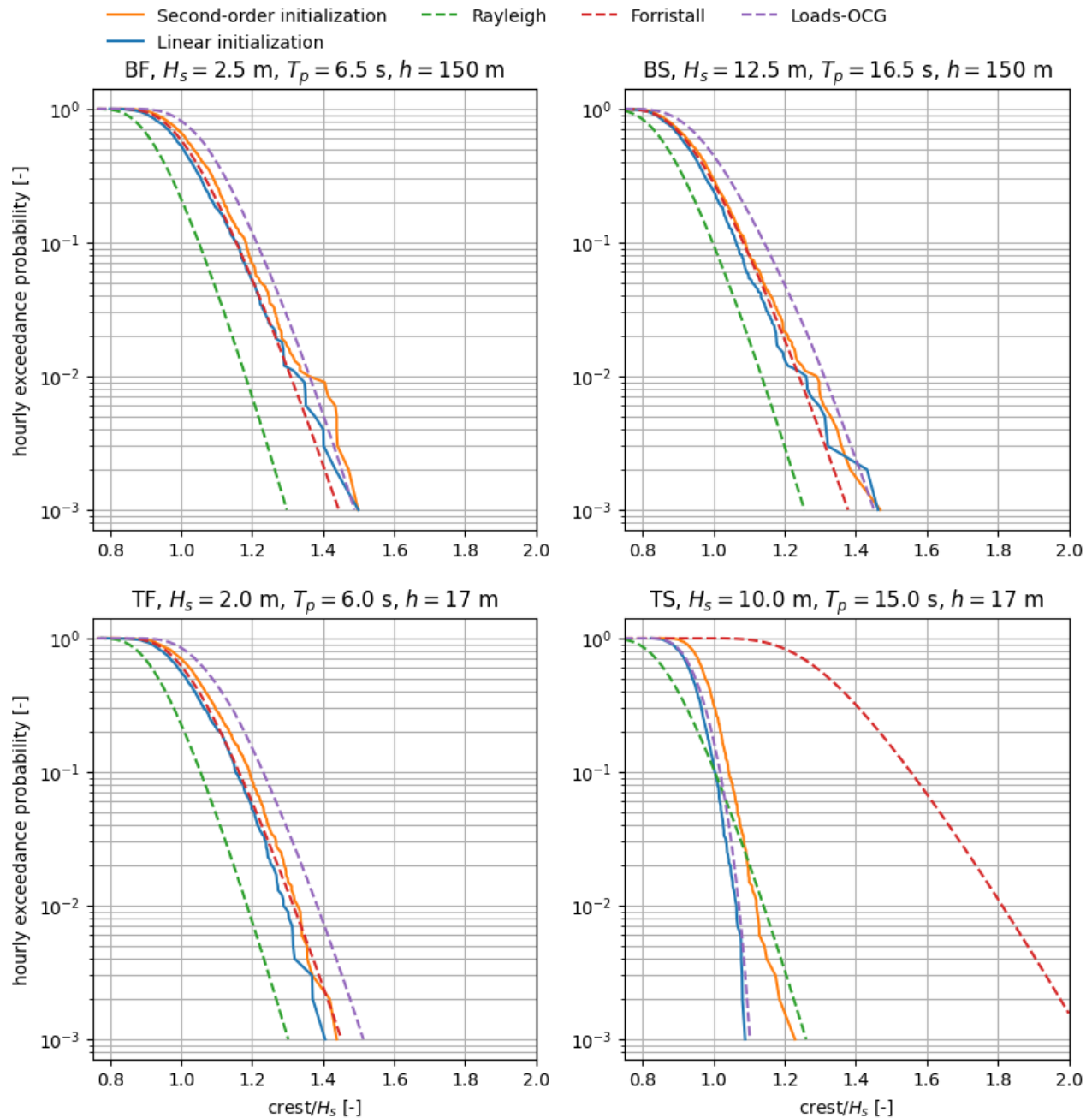


Figure 2-12 Estimated distributions of hourly maximum crest heights from short-crested HOSM simulations with linear- and second-order initial condition.

## 2.7. Summary and conclusions

In this work HOSM has been enhanced with a wave breaking model that introduces the effect of breaking of steep waves that naturally occurs in a random wave field of a certain sea-state wave steepness. Through extensive validation against model-test results of long- and short-crested irregular waves it is shown that HOSM with breaking model predicts crest statistics in good agreement with model-tests. Moreover, it is shown through comparison with full CFD simulations that HOSM describes wave kinematics in reasonable agreement with CFD results. However, for wave kinematics in very steep and breaking crests the agreement with CFD results is less good, which is expected due to the complex nature of wave breaking.

As a case study, HOSM with breaking model, has been used in long- and short-crested simulations of four sea states relevant for the Teesside and Brittany sites considered in the HIPERWIND project. Resulting crests wave elevation statistics (considering return periods up to 1000 hours for each sea state) have been compared with commonly used reference distributions based on linear and second-order theories as well as to recent distributions taking wave-breaking and shallow water depth into account. It is shown that HOSM predicts results in good agreement with the relevant reference distributions. For relatively shallow water conditions, a strong dependence on the directional spreading of the waves are observed on the crest statistics, highlighting the importance of running directional/short-crested analyses using wave spectra with realistic directional spreading.

We conclude that HOSM represents a relatively simple and numerically efficient way to analyze long-term wave statistics, such as crest heights and wave kinematics, that in turn can be used to estimate long-term statistics of wave induced responses. Thus, HOSM represents an attractive alternative to traditional approaches based on linear- or second-order theories. However, for structural responses highly sensitive to breaking-wave kinematics it is anticipated that results based on HOSM may not be very accurate, although likely significantly more accurate than e.g. linear or second-order methods.

## 3. HOS vs linear prediction of kinematics.

### 3.1. Selection of the sea states, models, and variables

#### 3.1.1. Selections of the cases: sea states and locations.

The selection of the different sea states, along with the presentation of the geographical location, along with the acronyms used to refer to the different cases are available in section 2.6.1. We simply recall in Table 3-1 the different cases and the main associated parameters.

*Table 3-1. Summary of the selected study cases for the influence of the different parameters. Note that the linear hypothesis is invoked for the computation of the peak wavelength.*

| Case name             | $H_s$ [m] | $T_p$ [s] | $\gamma$ [-] | $h$ [m] | $H_s/\lambda_p$ [%] | $h/\lambda_p$ [-] |
|-----------------------|-----------|-----------|--------------|---------|---------------------|-------------------|
| Brittany Fatigue (BF) | 2.5       | 6.5       | 3.0          | 150     | 3.7                 | 2.27              |
| Brittany Severe (BS)  | 12.5      | 16.5      | 1.46         | 150     | 3.0                 | 0.36              |
| Teesside Fatigue (TF) | 2.0       | 6.0       | 3.0          | 17      | 3.7                 | 0.31              |
| Teesside Severe (TS)  | 10        | 15        | 1.34         | 17      | 5.4                 | 0.092             |

### 3.1.2. Selection of studied variables

The study of the kinematics within the fluid is of primary importance in the design chain of both floating platform and fixed structures submitted to waves. The statistical distribution for wave heights and horizontal kinematics at crests – both accelerations and velocities – will be studied. The reasoning is that those variables are of prime importance when one wants to model the wave loads applied on a structure with the use of a Morison formulation. This is the classical approach in the design phase, especially for the drag contribution.

### 3.1.3. Model selections and presentations

A different implementation of the same HOS model (presented in section 2) is used in this part of the report (section 3). This implementation is denoted “cosmos” in the following. The same methodology is also applied to model wave breaking (see section 2.2), with the same parameters ( $\alpha = 0.02$ ,  $U_c = 0.85$ ).

#### 3.1.3.1. Cosmos

The method is based on a HOS formulation of the problem [40], [41]. The acceleration is computed with a backward finite difference of order 3. From a linear JONSWAP spectrum, and a random phase for each of the selected modes, a time-domain simulation is computed, and we let the wave field evolve for a certain duration. Note that a horizontal two-dimensional version of this model has been developed but is not used here. For further details, the reader is referred to section 2.1.

##### 3.1.3.1.1 Filtering and anti-aliasing process

To ensure the stability and accuracy of the model, a filter is applied on the free surface elevation and free surface potential at every time step. This filter is expressed as

$$f_{\beta_1, \beta_2}(k) = \exp\left(-\left(\frac{k}{k_p \beta_1}\right)^{\beta_2}\right), \quad (2)$$

where  $\beta_1$  and  $\beta_2$  are filters parameters and  $k_p$  is the wave number of the peak frequency. A representation of the filter and its consequence on a wave spectrum is shown in Figure 3-1.

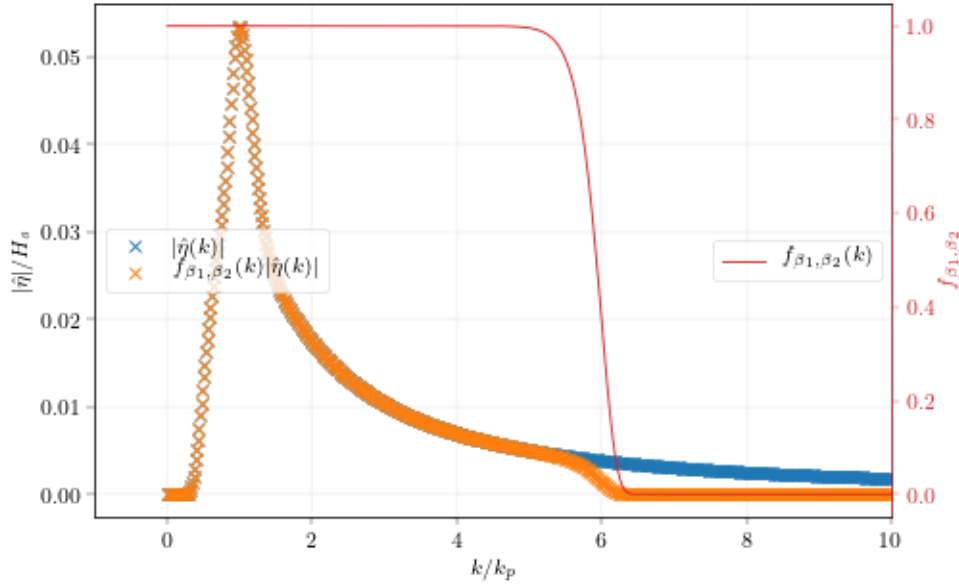


Figure 3-1. Amplitudes of the modes of the free surface elevation used for initialization with and without filter. In this example  $\beta_1 = 6$ ,  $\beta_2 = 30$  and  $\gamma = 3.0$ , for a total energy loss of 2.54%.

A simple anti-aliasing is used for every 2 terms product to avoid the generation or amplification of high frequency spurious modes. The dealiased number of modes is chosen as  $n = 3/2$ . See e.g., [43] for more information.

### 3.1.3.1.2 Breaking model

A breaking model is implemented, following the work of [44], [45]. The onset criteria is based on the relative value of the velocity at crest to the local phase velocity  $B_x = u_c/c_\phi$ . When  $B_x > 0.85$  a wave is considered as breaking, and the breaking is continued until  $B_x < 0.3$ . The energy dissipation is applied in the same manner as [45]: a modeled eddy viscosity computed following [46], [47], with  $\alpha = 0.02$ , is computed and enforced in both equations of the free surface evolution. Note that the breaking model is only activated in section 3.5: other calculations are simulated without energy dissipation due to breaking. For further detail, the same model is used in the previous section, where the breaking model is presented in section 2.2.

### 3.1.3.2. Calhypso

Calhypso computes in the temporal domain the prediction of the linear theory (Airy waves), basing on input spectrum parameters. Because the Airy wave theory is valid only up to  $z = 0$  (still water level), several stretching models are implemented, in order to access a modeled value of the kinematics at  $z = \eta$  (free surface elevation).

#### 3.1.3.2.1 Stretching models

Several stretching models have been proposed in the literature and reported by different authors (see [48]–[50] for instance). Because it was not possible to test (or even to list) all the existing stretching model in this report, it was decided to focus on the most common one (Wheeler stretching [51]) with some variations of this model, and on simple models that would give the maximum and minimum boundaries of the kinematics predictions. The different models and variations used in this report are described below, given the free surface written as:

$$\eta = \sum_i c_i \cos(\omega_i t + \varphi_i),$$

with  $c_i$  the amplitude of the  $i$ th wave component.

(Note: Only the horizontal velocity is given, but the same correction of the vertical profile applies on the accelerations).

- NONE: no stretching used, the kinematics are simply extrapolated following the linear theory above the mean sea level and until the crest. For example, for the horizontal velocity  $u_x$  is expressed as:

$$u_x(z, t) = \sum_i \frac{c_i g k_i}{\omega_i} \cos(\omega_i t + \varphi_i) \frac{ch(k_i(z+h))}{ch(k_i h)},$$

where  $k_i$  is the wavenumber of the  $i$ th component.

- VERT: vertical stretching, the kinematics in the crest are the same as at the mean sea level:

$$u_x(z, t) = \sum_i \frac{c_i g k_i}{\omega_i} \cos(\omega_i t + \varphi_i) \frac{ch(k_i(\min(z, 0) + h))}{ch(k_i h)}.$$

- WHEL: Wheeler stretching [51], the kinematics are stretched such that kinematics at the instantaneous free surface follow the value it would have at mean sea level according to the linear theory:

$$u_x(z, t) = \sum_i \frac{c_i g k_i}{\omega_i} \cos(\omega_i t + \varphi_i) \frac{ch\left(k_i(z+h) \frac{h}{h+\eta}\right)}{ch(k_i h)}.$$

- WHEP: a correction of the Wheeler model (sometimes called “Wheeler +”) proposed by [52] for which kinematics at the free surface level are computed instead at  $z = \eta_i$  for the  $i$ th wave component as:

$$u_x(z, t) = \sum_i \frac{c_i g k_i}{\omega_i} \cos(\omega_i t + \varphi_i) \frac{ch\left(k_i(z+h) \frac{h+\eta_i}{h+\eta}\right)}{ch(k_i h)},$$

with

$$\eta_i = c_i \cos(\omega_i t + \varphi_i).$$

- WHEM: another correction of the Wheeler model (sometimes called “Wheeler Modified”) described in [49], for which the short waves are considered riding on the long waves, changing the reference level for each wave frequency:

$$u_x(z, t) = \sum_i \frac{c_i g k_i}{\omega_i} \cos(\omega_i t + \varphi_i) \frac{ch\left(k_i(z+h) \frac{h}{h+\eta_i}\right)}{ch(k_i h)},$$

with

$$\eta_i = \sum_{j < i} c_j \cos(\omega_j t + \varphi_j).$$

- ZERO: The free surface level is always taken as the plane  $z = 0$  and the kinematics are computed at  $z = 0$ :

$$u_x(z = \eta, t) = \sum_i \frac{c_i g k_i}{\omega_i} \cos(\omega_i t + \varphi_i) \frac{ch(k_i(z_z + h))}{ch(k_i h)},$$

with

$$z_z = 0.$$

None of these models is strictly speaking consistent with the potential flow set of equations, but they are systematically used in offshore wind engineering to avoid too high kinematic predictions. Comparing these linear predictions with nonlinear kinematics is thus useful from the design point of view.

A sketch of different stretching models is shown in Figure 3-2.

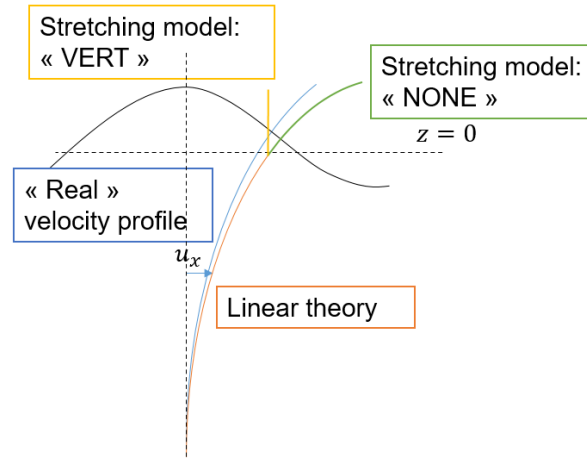


Figure 3-2. Sketch of different stretching models.

### 3.1.3.2.2 Random phases and amplitudes

The free surface elevation is given as a summation of the different considered modes:

$$\eta = \sum_i a_i \cos(\omega_i t) + b_i \cos(\omega_i t) = \sum_i c_i \cos(\omega_i t + \varphi_i), \quad (3)$$

where  $i$  represents the index of the modes.  $\varphi_i$  is randomly selected with a uniform distribution in the interval  $[-\pi, \pi]$ . The amplitudes  $a_i$  and  $b_i$  should theoretically be selected following Gaussian distributions, leading to a Rayleigh distribution for  $c_i$  [53]. However, the selection of deterministic  $c_i$ , based only on the spectrum energy content, is a classical approach in the engineering field. Its influence is investigated in section 3.3.

### 3.1.4. Methodology and parameters

#### 3.1.4.1. Cosmhos

The length of the domain is fixed at  $L_x = 64\lambda$ . The number of points is chosen as 8192 for all cases, yielding a horizontal spatial discretization of  $dx = \lambda/128$ . All modes (4096) are conserved, but the filter described in section 3.1.3.1.1 is applied with  $\beta_1 \in [6,8,10]$  and  $\beta_2 = 30$ . This means that the cut-off mode is located at [384, 512, 640] respectively. A linear theory is used to initialize the wave field, and the nonlinear part is gradually included in time over the course of 8 peak periods (10 peak periods are excluded from the statistics during the post-treatment phase). The temporal discretization is chosen as  $dt = T_p/100$ . For each case, ten runs are computed, each simulating 1000 periods. A nonlinearity order of 5 is chosen in this work, and the dealiasing is only performed on 6144 modes. The filtering process is however used to remove the aliased high frequencies.

#### 3.1.4.2. Calhypso

Here again the different variables are extracted at a given point 100 times per period for 1000 period per run. A minimum of 10 runs is performed. The spectrum is discretized into 256 modes, regularly distributed in period, from  $\sim T_p/4$  to  $2 T_p$ .

For the multidirectional studies (see section 3.4), the spreading parameter  $s$  has been varied, with 256 modes in each of the different directions. These directions are uniformly distributed within an angle range depending on  $s$  to capture most of the energy of the spectrum. The number of directions is fixed at 30 while the range varies from  $[-60^\circ, 60^\circ]$  to  $[-40^\circ, 40^\circ]$  for  $s = 5$  and  $s = 20$  respectively.

#### 3.1.4.3. Summary

For each case defined above (BF, BS, TF, TS), different simulations are computed. Each simulation is composed of a minimum of 10 runs representing a sea state ( $\sim 1000$  waves periods) to account for the randomness of the phase selection.

Table 3-2. Case setup for the different model used.

|  | <b>Cosmhos</b> | <b>Calhypso</b>   |
|--|----------------|---|
| Assumptions                                | Potential      | Potential linear  |
| Number of random phase runs                | $\geq 10$      | $\geq 10$   |
| Number of periods per run                  | 1000           | 1000  |
| Model in above $z = 0$                     | resolved       | Stretching  |
| Varying parameters (different simulations) | $\beta$        | Stretching model, directionality, random amplitudes, random phases. |

The different variables of interest are extracted as a function of the time  $t$  at the center of the domain ( $x = L_x/2$ ), and the temporal density probabilities of those variables are compared to one another for the different simulation

Note that the probability at  $10^{-4}$  will be studied in more detail, and as  $dt = T_p/100$ , this represents a  $1/100^{\text{th}}$  of the waves. In other words, we encounter this value or above in average 10 times in each run. Note that they may be located on the same wave. Across the 10 runs, we should encounter this value or higher  $\sim 100$  times.

## 3.2. Influence of the nonlinearities – stretching models.

The nonlinearity is most of the time not accounted for in the engineering process of design. However, it is known that this hypothesis underestimates the crest height and overestimate the crest trough for regular waves. This has a first influence: the wet surface of a free surface piercing object is underestimated at both crest and trough. The associated load might not be correctly predicted. In addition, the linear theory provides a formulation of the velocity and acceleration fields, but only up to  $z = 0$  (Still Water Level, SWL). Multiple simple stretching models, presented in section 3.1.3.2.2, exists and are often use by engineers to account for this shortcoming. This section aims to quantify the errors and uncertainties committed when using those kinds of theory and models. Each case (i.e. location + sea state) is presented in a different figure (Figure 3-3, Figure 3-4, Figure 3-5 and Figure 3-6 for respectively BF, BS, TF and TS) thereafter. Results are discussed in the following subsection 3.2.5.

### 3.2.1. Brittany Fatigue (BF)

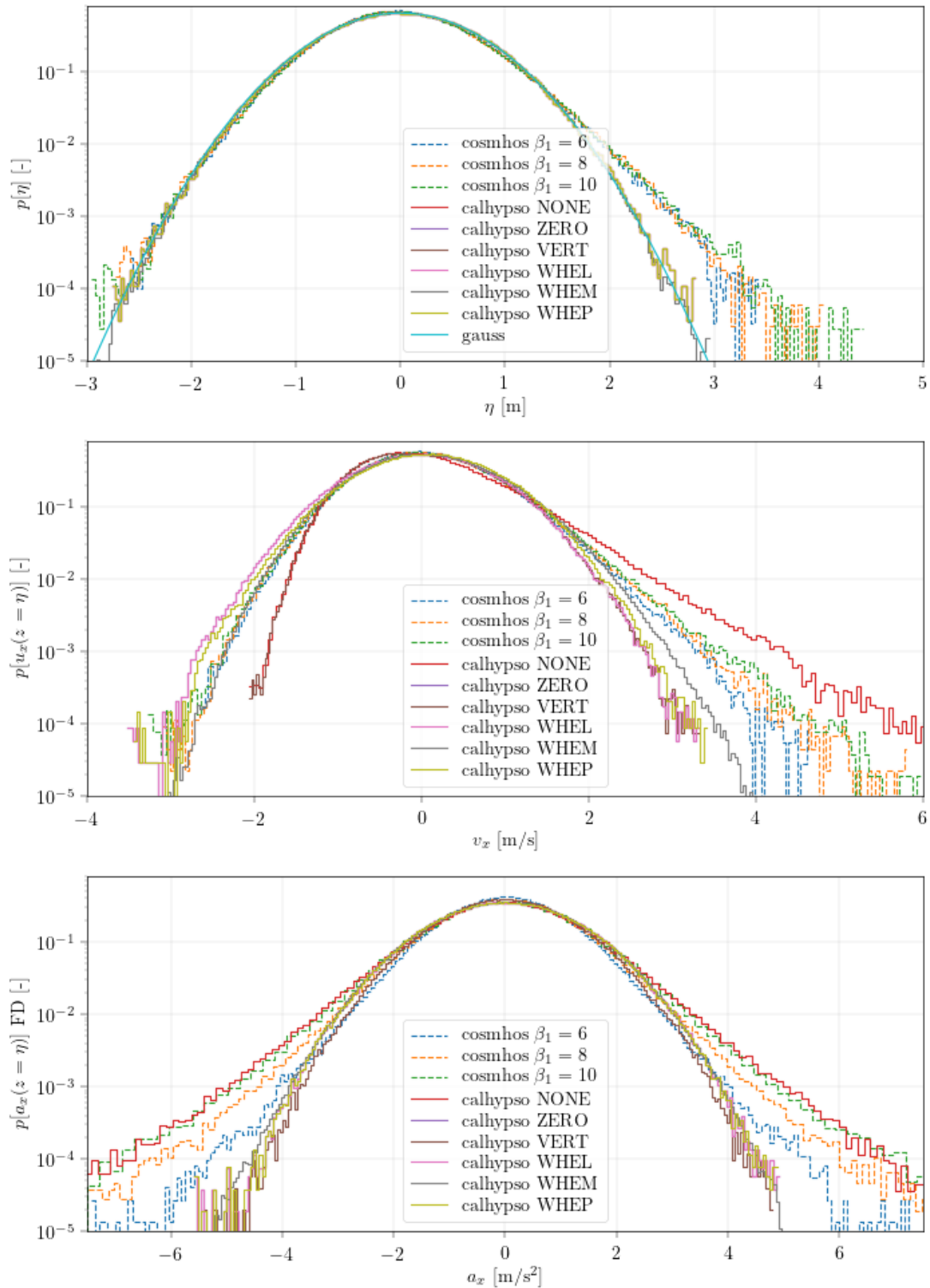


Figure 3-3. PDF of the free surface elevation (top panel), horizontal velocity (middle panel) and horizontal acceleration (bottom panel), HOS simulation (Cosmhos, dashed) with different high frequency filters, and Linear potential model (Calhypso) with different stretching models. Bretagne fatigue.

### 3.2.2. Brittany Severe (BS)

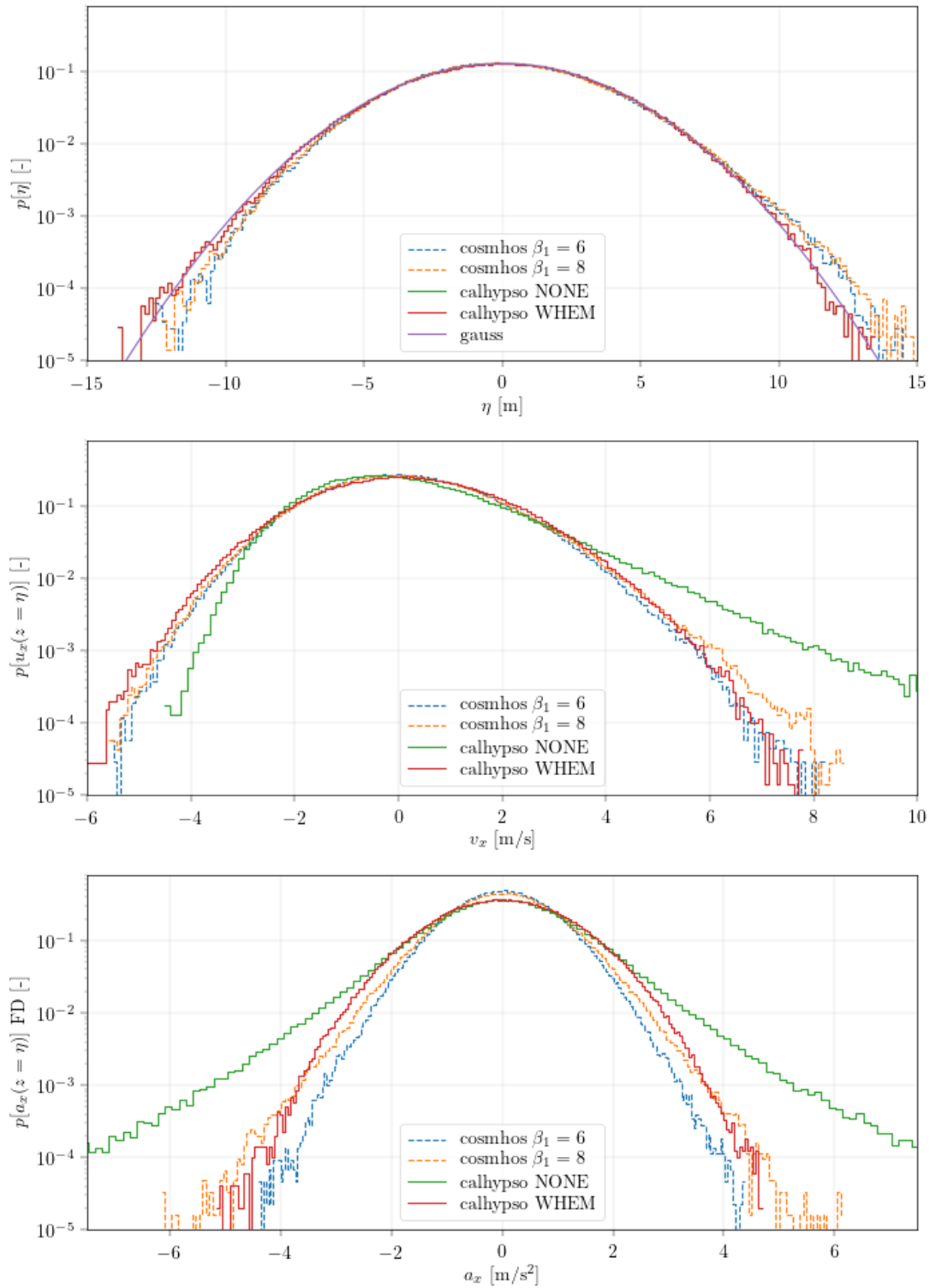


Figure 3-4. PDF of the free surface elevation (top panel), horizontal velocity (middle panel) and horizontal acceleration (bottom panel), HOS simulation (Cosmhos, dashed) with different high frequency filters, and Linear potential model (Calhypso) with different stretching models. Bretagne severe case

### 3.2.3. Teesside Fatigue (TF)

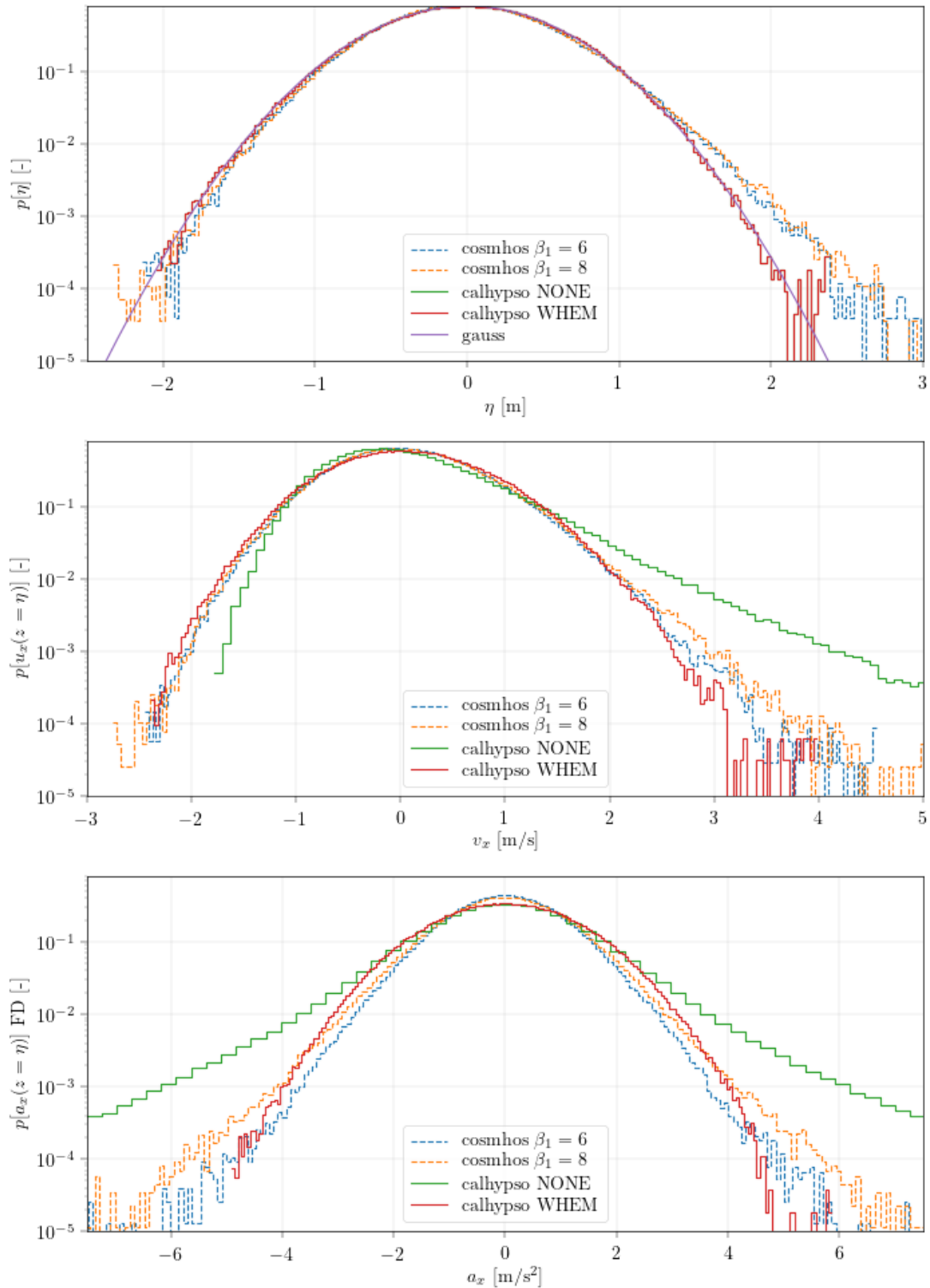


Figure 3-5. PDF of the free surface elevation (top panel), horizontal velocity (middle panel) and horizontal acceleration (bottom panel), HOS simulation (Cosmhos, dashed) with different high frequency filters, and Linear potential model (Calhypo) with different stretching models. Teesside fatigue case.

### 3.2.4. Teesside Severe (TS)

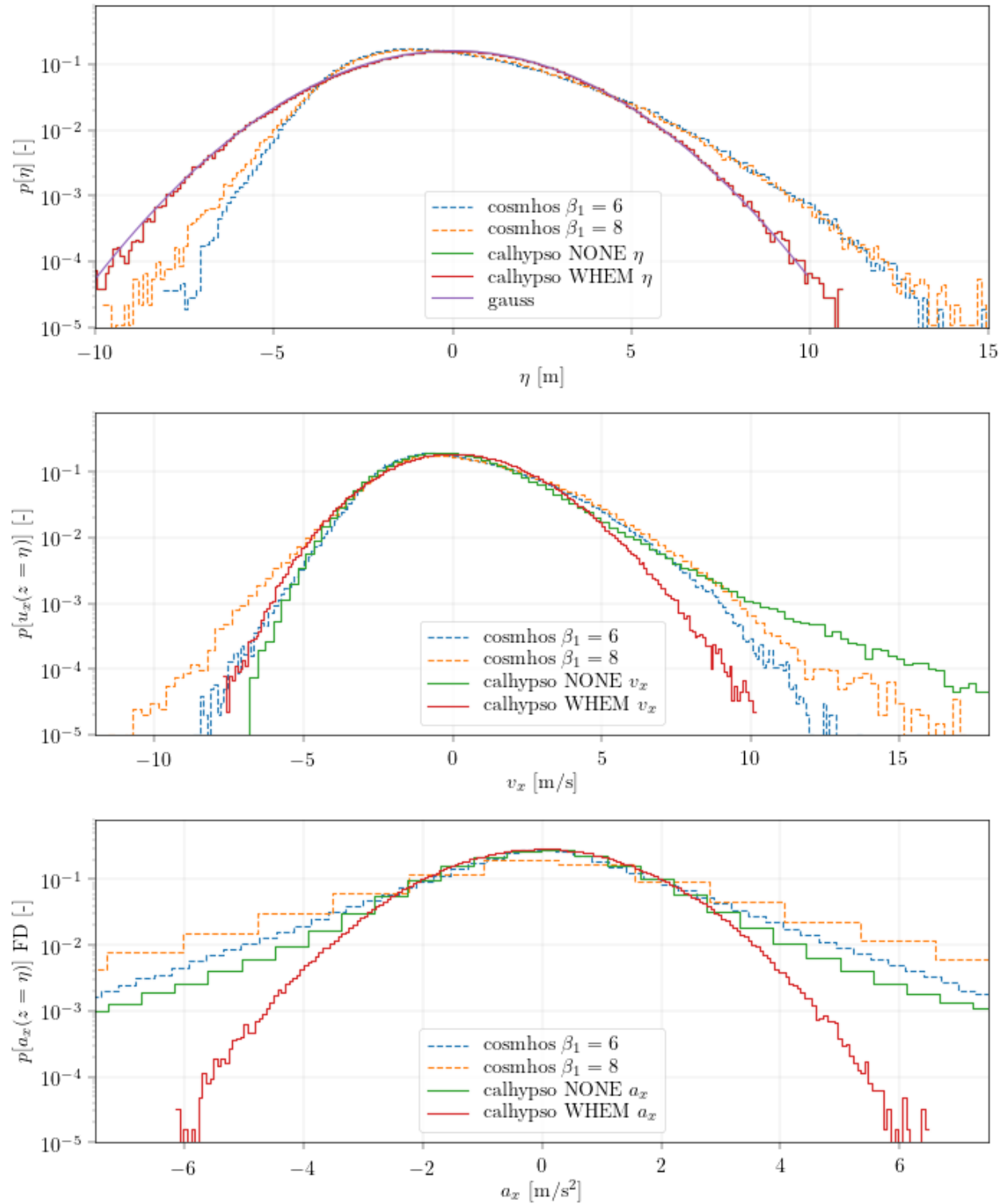


Figure 3-6. PDF of the free surface elevation (top panel), horizontal velocity (middle panel) and horizontal acceleration (bottom panel), HOS simulation (Cosmhos, dashed) with different high frequency filters, and Linear potential model (Calhypso) with different stretching models. Teesside severe case

### 3.2.5. Discussions

Figure 3-3 shows the probability density function (PDF) of the time series of different variables of interest ( $\eta$ ,  $v_x$ ,  $a_x$ ) at the center of domain, predicted by several simulations. Namely, the prediction of calhypso different stretching models (presented in section 3.1.3.2.2) and of coshmos with different  $\beta_1$  are compared. The theoretical linear distribution in terms of free surface elevation is also added, as the corresponding Gaussian curve.

Because the stretching model is applied on the kinematics, the free surface elevations are the same for all potential linear simulation. Note that this is because, while the phases of the different runs are random, they are the same for the different simulations. In other words, the phases of the “sea state 1” (run 1) are the same for all calhypso simulations (whatever the stretching model), and the same is true for “sea state 2” etc.

Thus, all linear simulations underpredict the free surface elevation, by about 7 to 16%, depending on the case, at the probability  $10^{-4}$  the same order of magnitude of the effect is found for the two “fatigue” cases, which suggests that the relative water depth is not of significant effect, while the larger underpredictions are encountered for the TS case: the wave height nonlinear parameter  $H/\lambda$  (steepness) seems to be the first driver of the discrepancy in terms of maximum free surface elevations. Remark that the underprediction is sorted by this nonlinearity parameter.

Also note that, as shown in section 2.6.3, the wave breaking model is of significant influence on the TS case, while it is not on the three other cases. Thus, using a non-breaking coshmos simulation with  $\beta_1 = 6$  as a “reference” for the TS case leads to a larger underprediction of the different variables than what could be expected in a real sea state.

*Table 3-3. Underprediction at  $1e^{-4}$  of the different variables of interest for the different cases with the linear potential model (calhypso). Reference simulations are coshmos with  $\beta_1 = 6$ . Linear values for the BF case are given for two different types of stretching models: those using the values obtained at  $z = 0$  directly at  $z = \eta$  and WHEM.*

| Relative difference<br>at $1e^{-4}$ of | BF    |      | BS WHEM | TF WHEM | TS WHEM |
|--|-------|------|---------|---------|---------|
|  | $z=0$ | WHEM |         |         |         |
| $\eta$ [-]                             | -13%  |      | -7%     | -13%    | -16%    |
| $v_x$ [-]                              | -20%  | -13% | 3%      | -7%     | -18%    |
| $a_x$ [-]                              | -18%  | -17% | 10%     | -4%     | -51%    |
| $H_s/\lambda$ [-]                      | 3.7%  |      | 3.0%    | 3.7%    | 5.4%    |
| $h/\lambda$ [-]                        | 2.27  |      | 0.36    | 0.31    | 0.092   |

Concerning the velocities, it seems that, once again, the nonlinear model yields maximum values above of what is possible to obtain with the linear potential assumption. Only the “NONE” stretching model (see section 3.1.3.2.2), which overpredicts any kinematics when  $\eta > 0$ , predicts higher values than the coshmos model. This model will not be discussed in the following, given its very rare use in practical applications for its well-known overpredictions. “WHEL”, “VERT”, and “ZERO” all predicts the same velocities at crests  $z = \eta$ : exactly the one predicted at  $z = 0$ . This is well known to underpredict the velocity at crest, given that, under the crest, the velocity profile is strictly increasing with  $z$ , up to  $z = \eta$ . “WHEP” and “WHEM”, modified versions of the Wheeler model are developed to overcome this shortcoming. It seems however that both “WHEP” and “WHEM” still underpredict the velocities at the wave crest. This might also be due to the elevation at which the velocity is given (computed from the linear theory), instead of the

real one, which is significantly higher. Note that the underprediction in velocities by those modified models is of the same order of magnitude than the underprediction on the free surface elevation. An interesting continuation, out of the scope of this work, would be to calculate the kinematics at the nonlinear free surface elevation to estimate the relative error.

Also note here that the relative water depth  $h/\lambda$  seems to be of large influence: a better agreement is found between cosmhos and calhypro for BS and TF than for BF, both being at lower relative water depth. One of the explanations might be the sensitivity of the stretching model WHEM to the water depth, through the use of the wave number  $k$  in the reconstruction of the kinematics. This wavenumber is obtained from the cyclic frequency through the linear finite water depth dispersion relation. The relative wave height remains also of course of significant influence, leading to a large underprediction of the velocity for the TS case. Note that the absence of breaking model within cosmhos might explain part of this underprediction.

In the following, only the “WHEM” model will be simulated, given its larger prediction, seemingly in better agreement with the nonlinear potential model cosmhos.

For the accelerations, a large impact of the filter  $\beta_1$  is denoted in cosmhos simulations. This was expected given that the higher modes contribute in a larger manner to the acceleration than the lower modes ( $\hat{a}(k) \propto k^2$ ). However, for large values of  $\beta_1$  ( $\geq 8$ ), the computation of the acceleration quickly becomes unstable, or at least, produce spurious values that pollute the maxima of the distribution. It seems to be difficult to find a range of  $\beta_1$  large enough to capture enough modes to correctly compute the accelerations while avoiding the appearance of those spurious values. While with  $\beta_1 = 6$  spurious waves of velocity are not observed (except for TS), we expect the filter to lead to an underestimation of the accelerations, and to a lesser extent, of the velocities.

In conclusion, the linear model only gives an estimate of the velocities at the crest. Stretching models are necessary not to commit a large underestimation (if the kinematics at  $z = 0$  are assumed at the crest) or a large overestimation (if the profile function is extended up to  $z = \eta$ ) of the kinematics at the free surface. The model that best fits the results given by the nonlinear simulation is a modified version of the Wheeler stretching method, see section 3.1.3.2.2 for details. However, the results are still found to be non-conservative in terms of predicted surface elevation, velocities, and accelerations at the crest, by a factor up to 30%. Note that this large underprediction is only expected to be of significant magnitude at the crest, and the discrepancies are expected to reduce in the water column. Thus, the total error on, for instance, a monopile is expected to be lower than the value mentioned above, and after integration over the water depth, the linear model is expected to yield valuable information, despite not being accurate for  $z > 0$ .

### 3.3. Influence of random amplitude

As discussed in section 3.1.3.2.2, selection of deterministic amplitudes when generating a sea state from a spectrum does not yield a Gaussian distribution of the free surface elevation. A more rigorous approach is to use a Rayleigh distribution for the choice of the mode amplitudes. This section aims at investigating the consequence of such often made simplifications.

In the simulation denoted with “RAYL”, the amplitudes of the modes are chosen randomly, following a Rayleigh distribution. The phases are also chosen randomly but are the same for different simulations. We perform between 100 and 500 runs for each simulation in order to ensure a convergence of the amplitudes throughout the different runs. One run consists of 1000 periods described with  $10^5$  time steps.

### 3.3.1. Brittany Fatigue

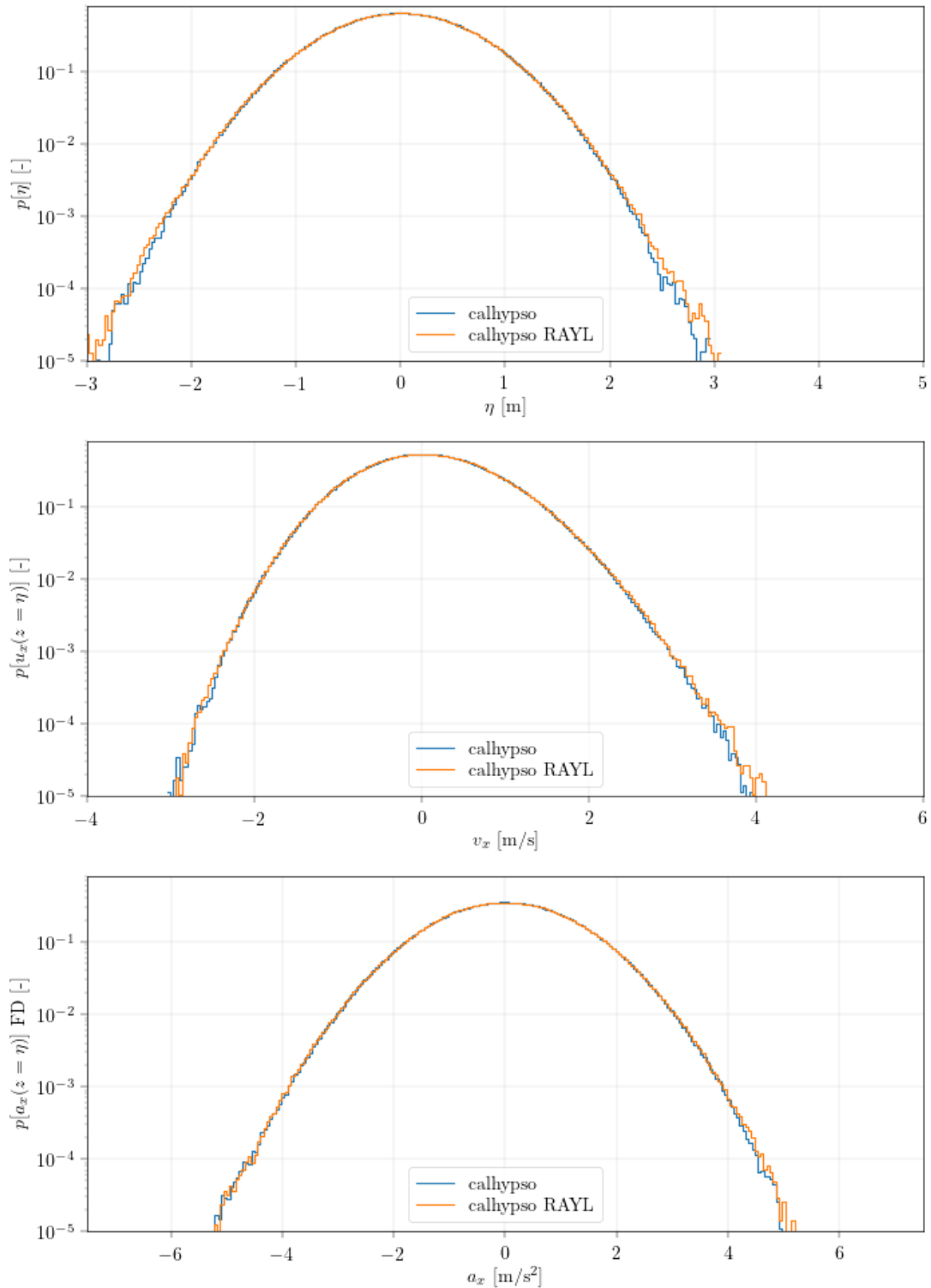


Figure 3-7. PDF of the free surface elevation (top panel), horizontal velocity (middle panel) and horizontal acceleration (bottom panel), the WHEM stretching model is selected. The amplitudes are random in the RAYL case. Phases are also random but chosen equal for the two simulations. Brittany Fatigue.

### 3.3.2. Brittany severe

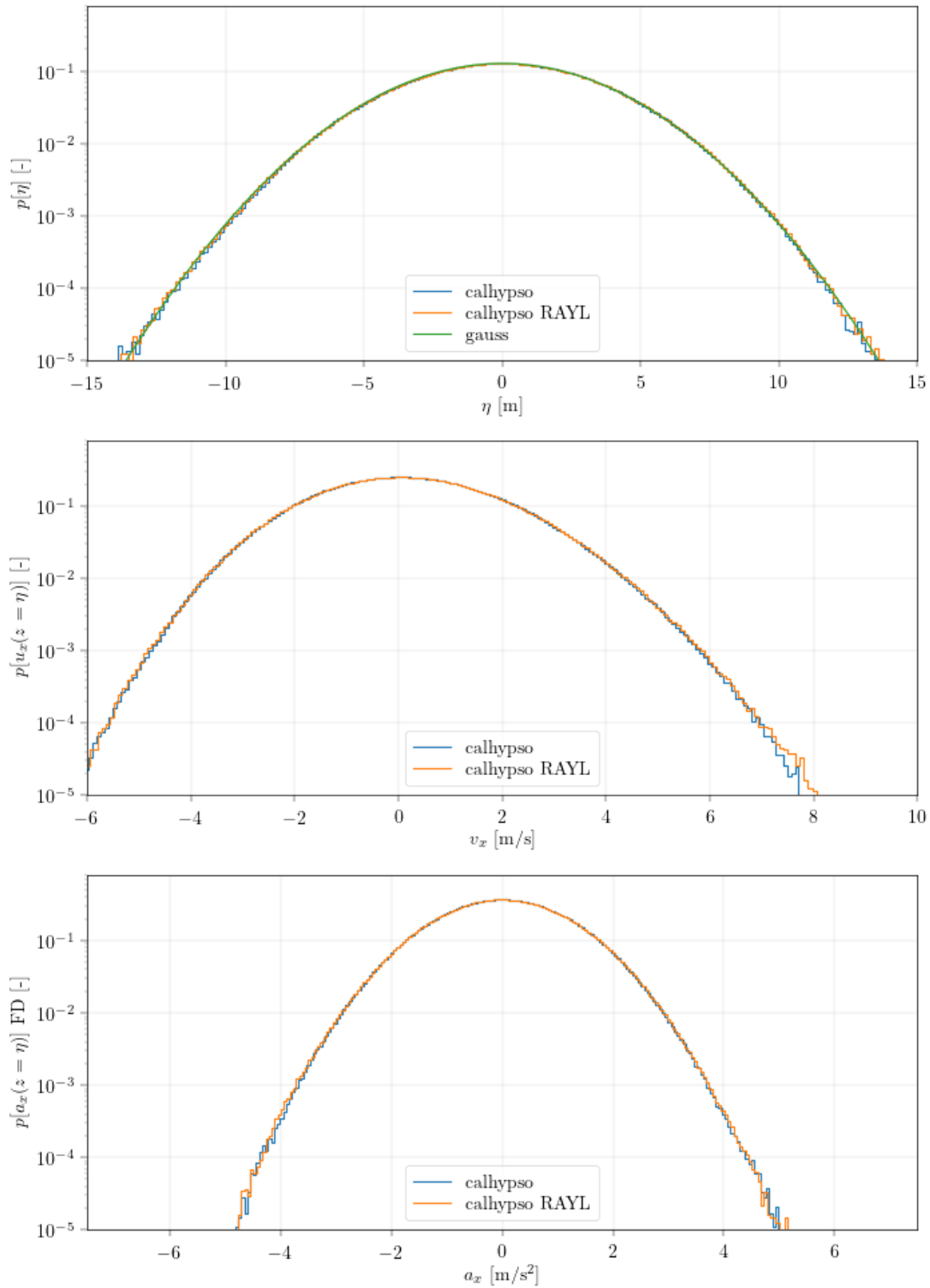


Figure 3-8. PDF of the free surface elevation (top panel), horizontal velocity (middle panel) and horizontal acceleration (bottom panel), the WHEM stretching model is selected. The amplitudes are random in the RAYL case. Phases are also random but chosen equal for the two simulations. Brittany Severe.

### 3.3.3. Teesside Severe

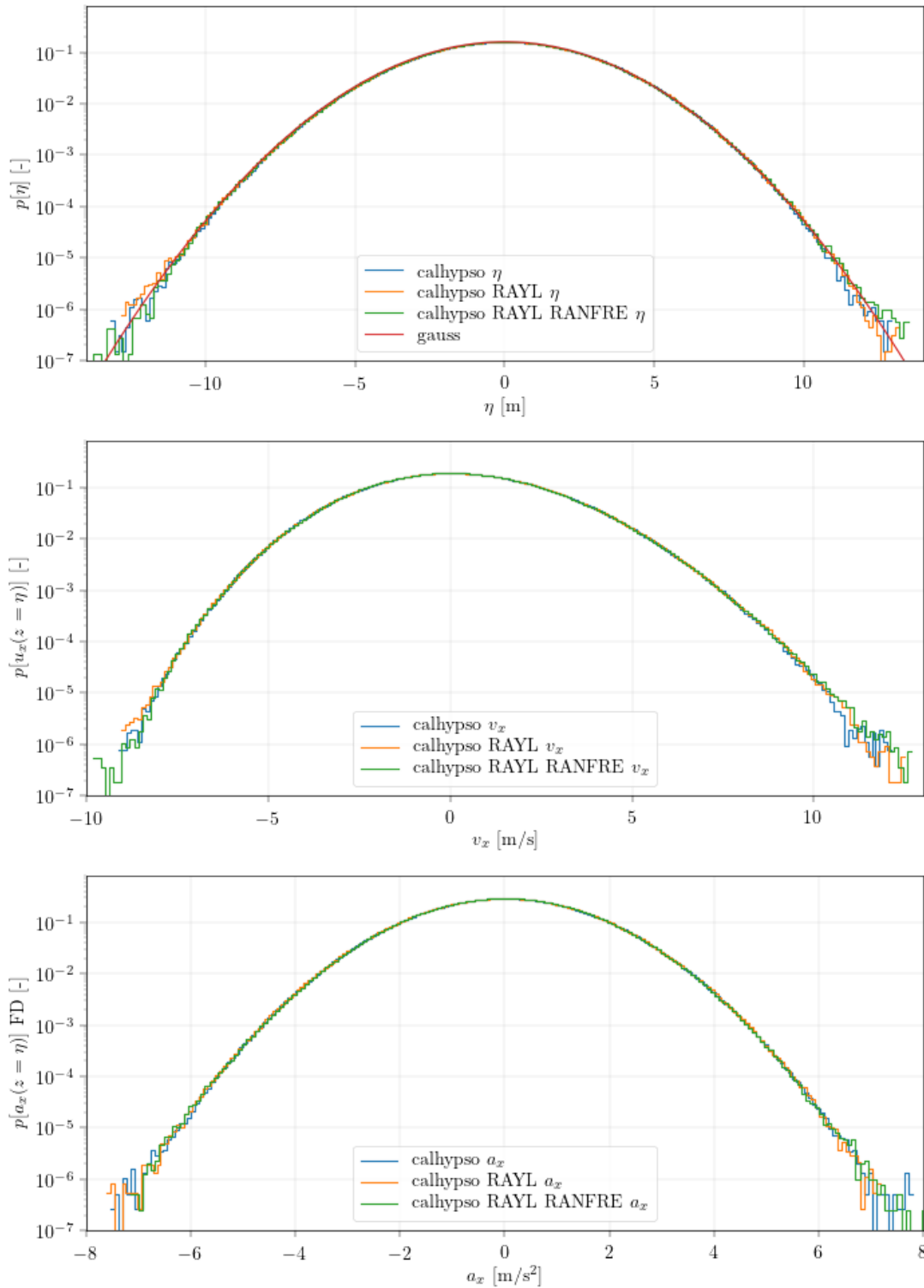


Figure 3-9. PDF of the free surface elevation (top panel), horizontal velocity (middle panel) and horizontal acceleration (bottom panel), the WHEM stretching model is selected. The amplitudes are random in the RAYL case. Phases are also random but chosen equal for the two simulations. Teesside Severe.

### 3.3.4. Teesside Fatigue

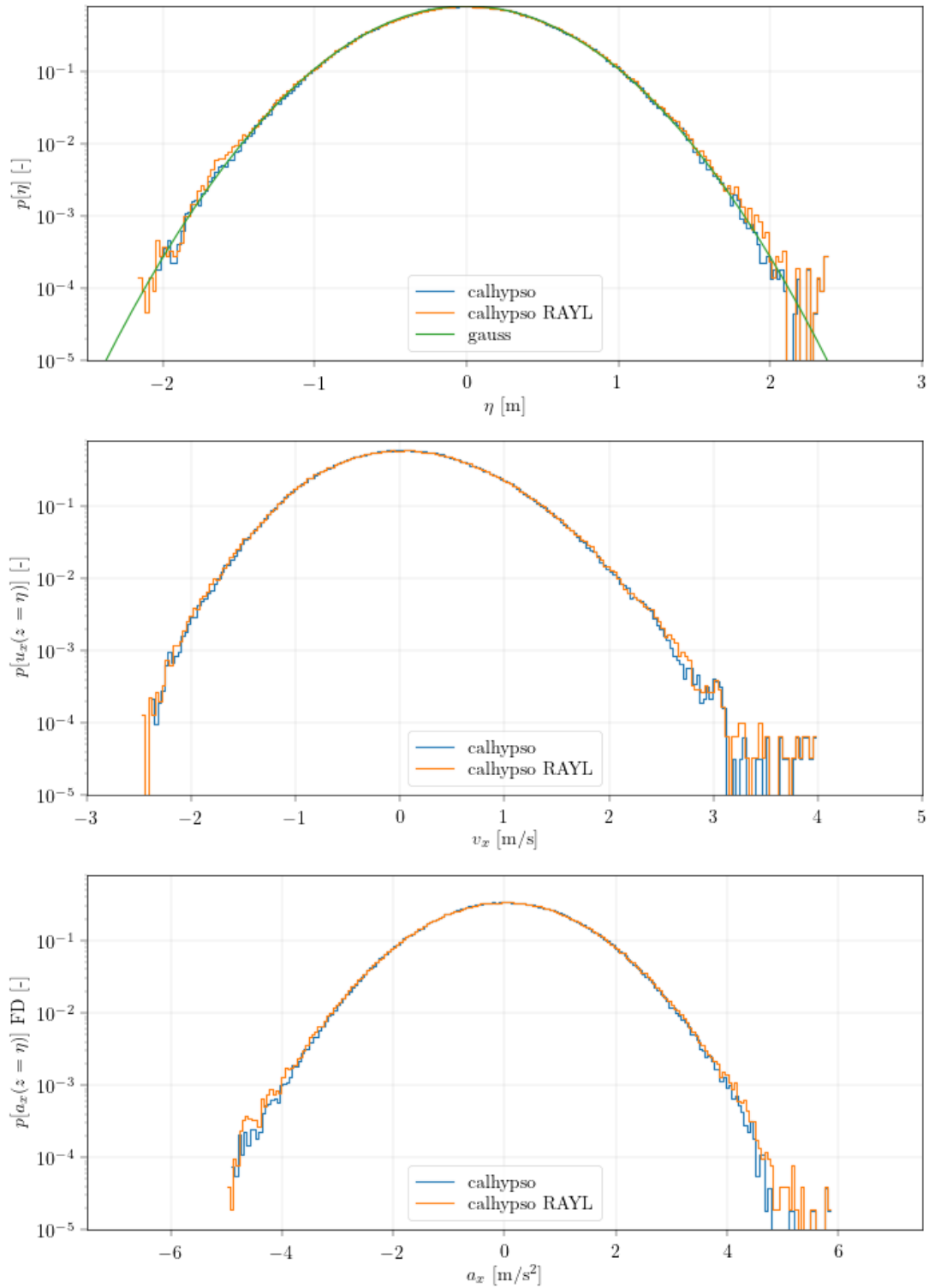


Figure 3-10. PDF of the free surface elevation (top panel), horizontal velocity (middle panel) and horizontal acceleration (bottom panel), the WHEM stretching model is selected. The amplitudes are random in the RAYL case. Phases are also random but chosen equal for the two simulations. Teesside Fatigue.

### 3.3.5. Discussions

For all the selected cases, the two simulations (random phases and random phases+Rayleigh distribution of the amplitudes) yield very equivalent results. Indeed, it is difficult to separate both simulations except for probabilities lower than  $10^{-4}$  and thus expected not to be converged. To further investigate this assumption, two longer simulations (500 runs of 1000 periods) were computed on the TS case. Another case is also added, which, instead of selecting the modes uniformly in terms of period, uses modes distributed randomly close to a uniform discretization of the spectrum in frequencies (RANFRE). Up to  $10^{-6}$  the three simulations are difficult to distinguish, leading us to conclude that the influence of both the selection of a Rayleigh distribution for the amplitudes or the selection of the spectrum discretization method are not of prime importance.

In conclusion, while using a simple deterministic model for the mode amplitude that miss part of the distribution physics, the consequence on the extrema of the free surface elevation, velocities and accelerations are not of significant importance. In addition, the added complexity of ensuring a convergence throughout the runs of the phases and amplitudes does not seem to be worth the cost.

## 3.4. Influence of directionality

Computing the linear theory with different spreading parameters, such that the spectrum is given as:

$$S(\omega, \beta) = S(\omega)G(\omega, \beta), \quad (4)$$

where  $S(\omega)$  is the classical JONSWAP spectrum and the spreading function  $G$  is defined as

$$G(\omega, \beta) = C_1(s) \cos^{2s} \left( \frac{\beta}{2} \right). \quad (5)$$

The function  $C_1$  is there to ensure that the total energy is respected at each frequency, i.e.  $\int_0^{2\pi} G(\omega, \beta) d\beta = 1$ .

Different values of  $s$  are tested and its effect on the distribution of free surface elevation, horizontal velocities and horizontal accelerations is assessed.

### 3.4.1. Brittany Fatigue

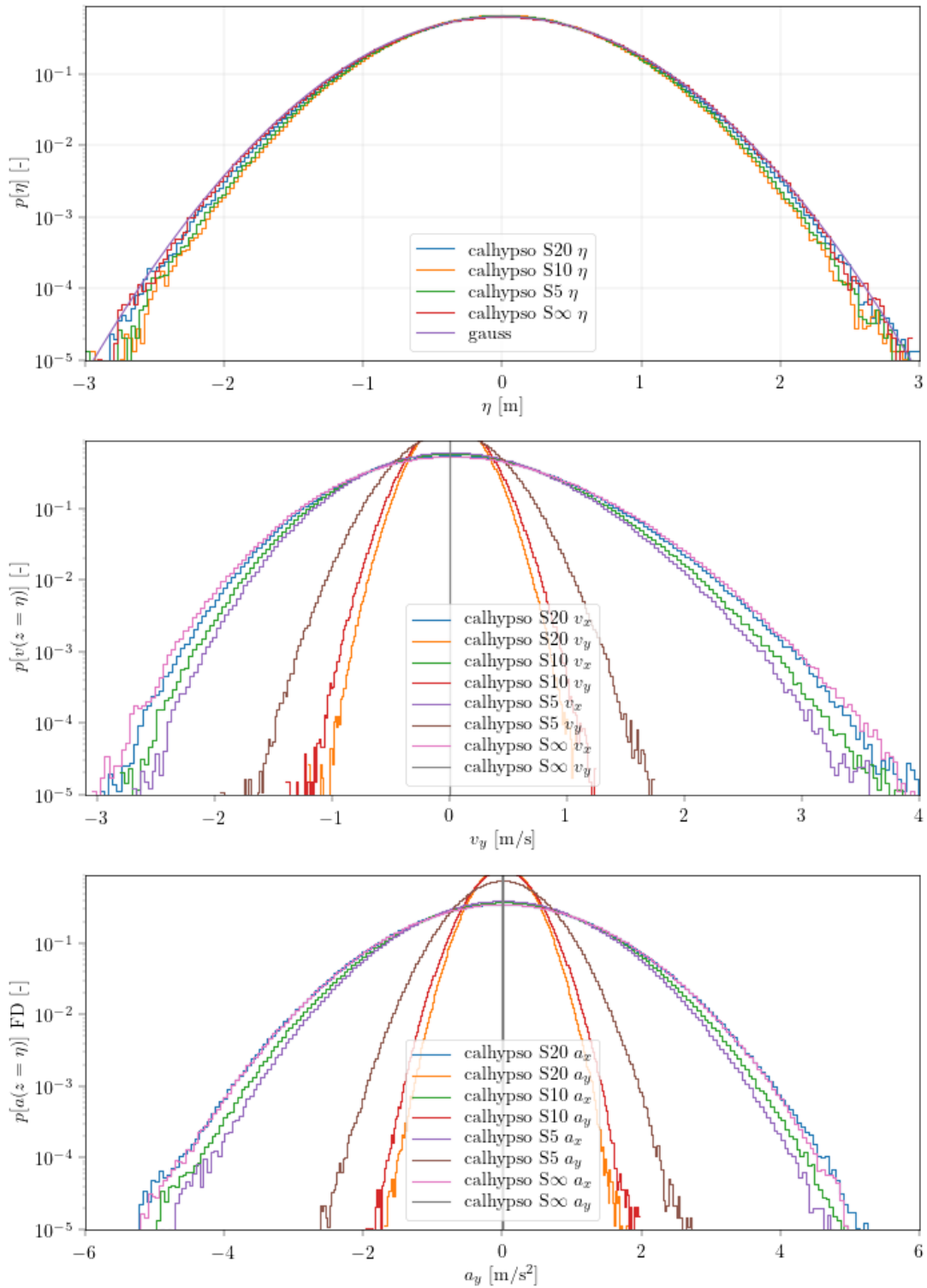


Figure 3-11. PDF of the free surface elevation (top panel), horizontal velocity (middle panel) and horizontal acceleration (bottom panel), the WHEM stretching model is selected. Bi-directional spectra parametrized by the value of  $S$ . Brittany Fatigue.

### 3.4.2. Brittany Severe

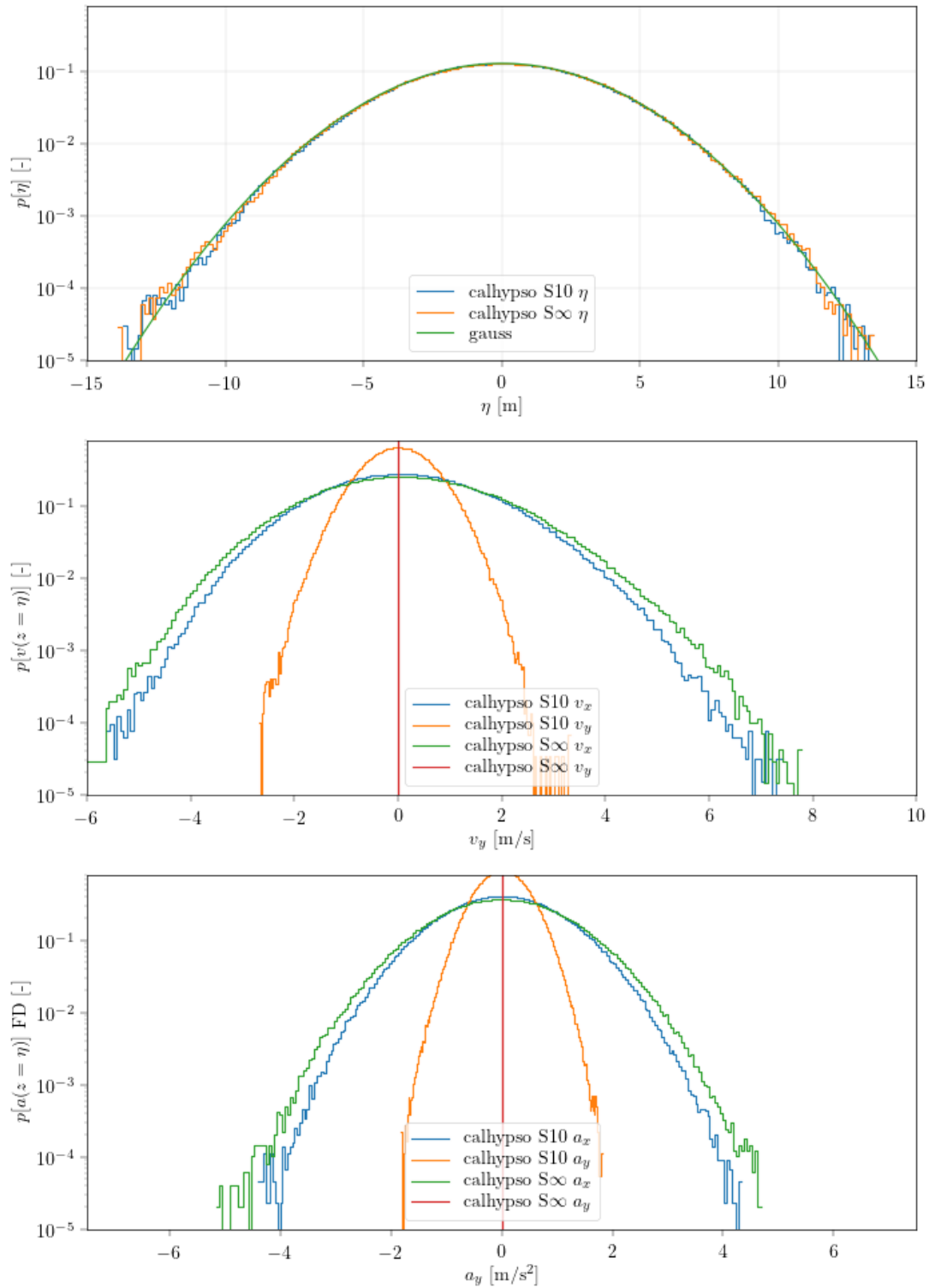


Figure 3-12. PDF of the free surface elevation (top panel), horizontal velocity (middle panel) and horizontal acceleration (bottom panel), the WHEM stretching model is selected. Bi-directional spectra parametrized by the value of  $S$ . Brittany Severe.

### 3.4.3. Teesside Fatigue

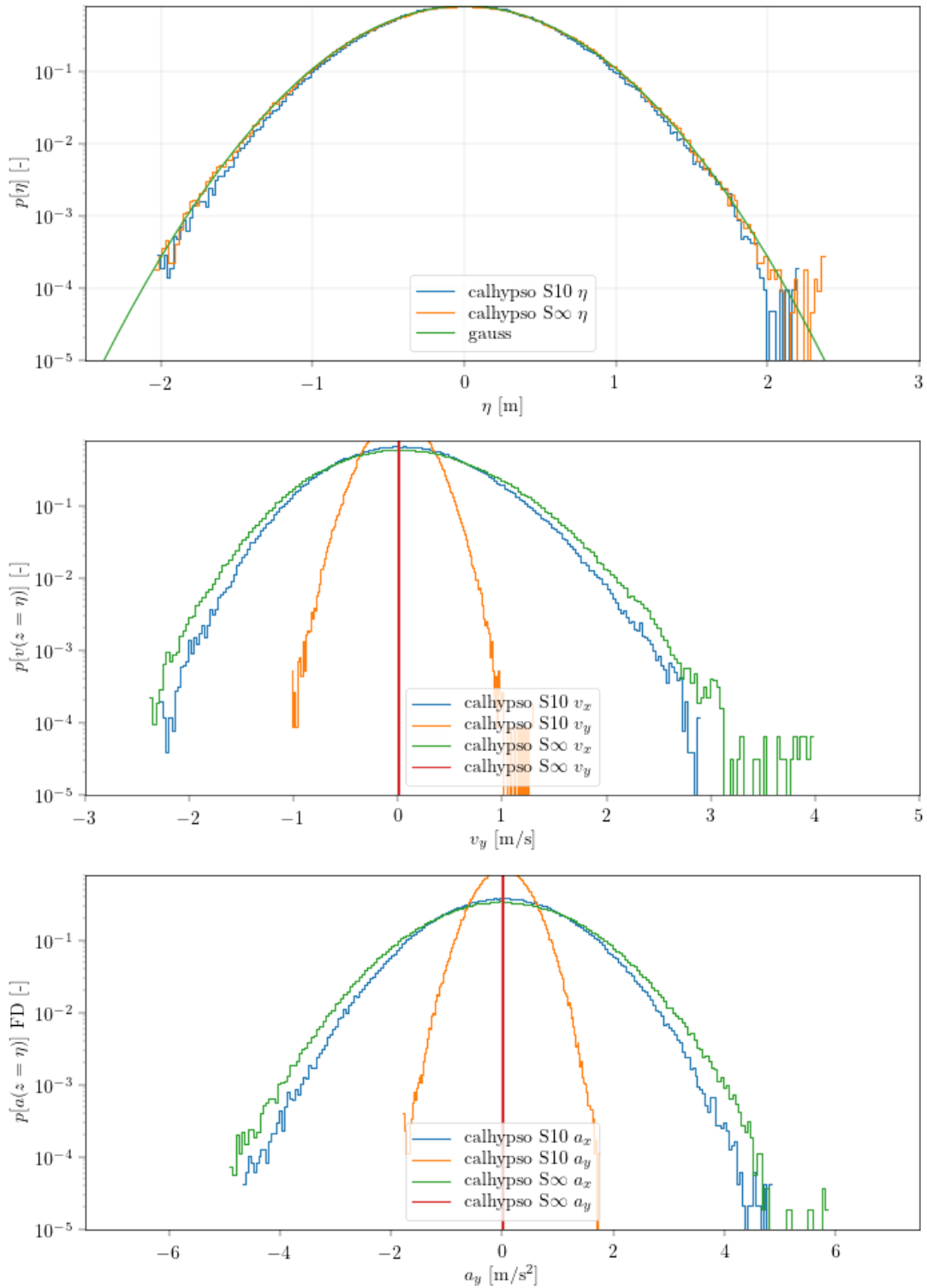


Figure 3-13. PDF of the free surface elevation (top panel), horizontal velocity (middle panel) and horizontal acceleration (bottom panel), the WHEM stretching model is selected. Bi-directional spectra parametrized by the value of  $S$ . Teesside Fatigue.

### 3.4.4. Teesside Severe

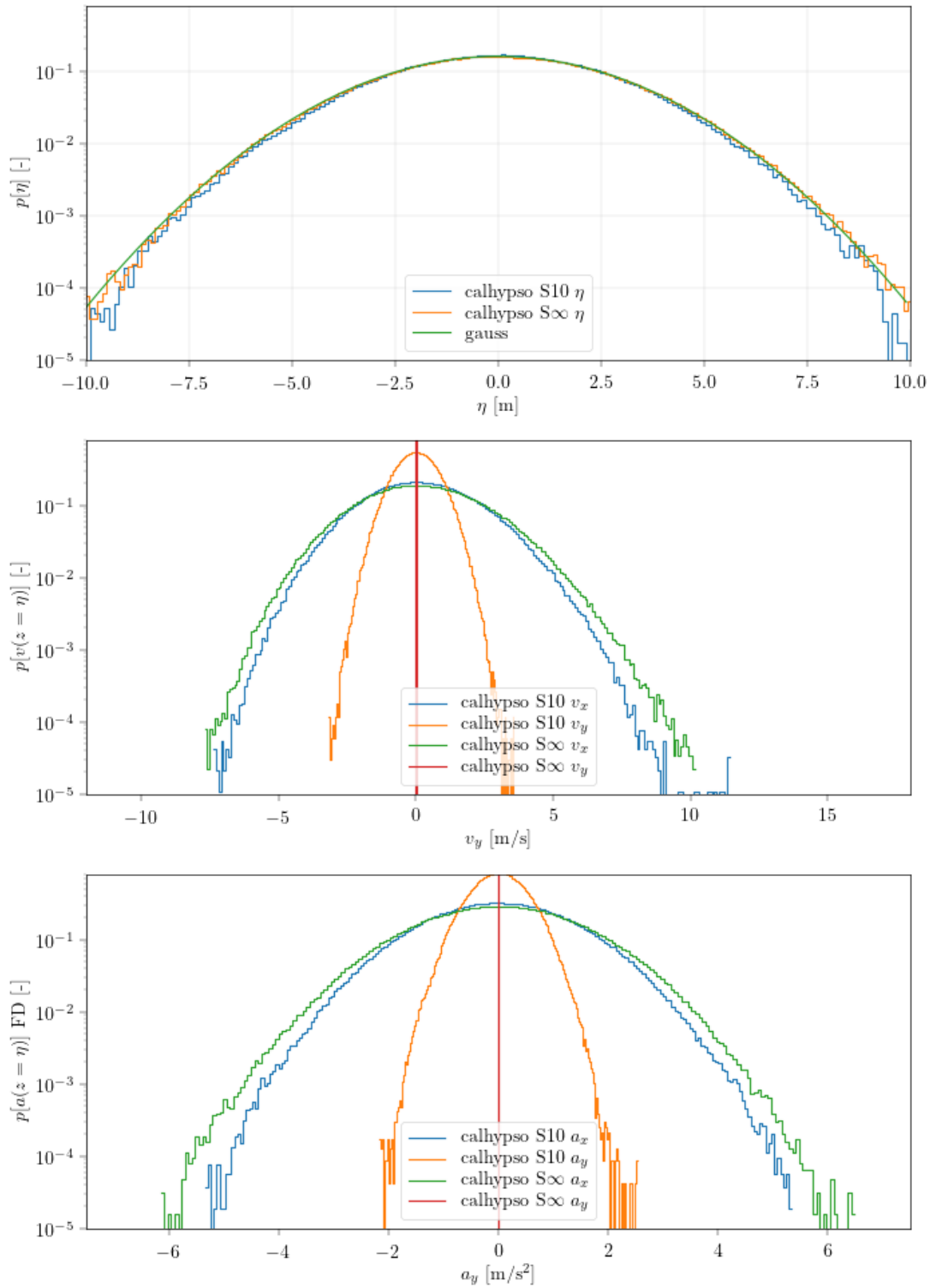


Figure 3-14. PDF of the free surface elevation (top panel), horizontal velocity (middle panel) and horizontal acceleration (bottom panel), the WHEM stretching model is selected. Bi-directional spectra parametrized by the value of  $S$ . Teesside Severe.

### 3.4.5. Discussions

Considering the bidirectionality of a wave spectrum of same total energy leads, as expected, to a lower velocity in the main wave direction (here taken as  $x$ ). Table 3-4 is a summary of the difference obtained between the unidirectional case (equivalent of a scalar  $s = \infty$ ), and the two directional wave spectra.

*Table 3-4 Relative difference of the higher values of probability  $1e^{-4}$  for different cases, compared to the reference, unidirectional simulation ( i.e.  $s = \infty$ ). Note that the values along “y” are not an error but a value relative to the unidirectional values along “x”.*

| Relative difference<br>at $1e^{-4}$ of | BF       |          |         | BS       | TF       | TS       |
|--|----------|----------|---------|----------|----------|----------|
|  | $s = 20$ | $s = 10$ | $s = 5$ | $s = 10$ | $s = 10$ | $s = 10$ |
| $\eta$ [-]                             | 1%       | -2%      | -0%     | -3%      | -6%      | -6%      |
| $v_x$ [-]                              | -2%      | -8%      | -11%    | -9%      | -13%     | -13%     |
| $v_y$ [-]                              | 27%      | 31%      | 43%     | 36%      | 32%      | 34%      |
| $a_x$ [-]                              | 5%       | -2%      | -6%     | -11%     | -7%      | -8%      |
| $a_y$ [-]                              | 32%      | 36%      | 50%     | 40%      | 38%      | 37%      |

As expected, part of the energy and thus kinematics are forwarded to the “y” direction, yielding a net reduction of the kinematics along “x”, while leaving the free surface elevation untouched. We also note that the results seem to not be largely dependent on the case of interest: the same order of magnitude of the bidirectionality can be observed for the different regions and sea states. Note that the wave breaking is not considered here. It was shown, see section 2.6.4, that the free surface elevation is impacted when studying short-crested waves on the TS case, due to the modification of the wave breaking.

## 3.5. Influence of wave breaking

The following study, assessing the influence of the wave breaking on the free surface elevation and kinematics, is conducted differently: a modified version of the Brittany Fatigue case is selected, in order to force wave breaking to be of significant influence.

### 3.5.1. Breaking Brittany Fatigue, moderate steepness.

The breaking criterion (see section 3.1.3.1.2) is never reached on the Brittany Fatigue case under the condition presented above ( $H_s = 2.5$  m,  $T_p = 6$  s). For that reason and to evaluate the influence of the wave breaking, the wave height has been increased. At  $H_s = 3.5$  m,  $T_p = 6$  s ( $H_s/\lambda_p = 5.3\%$ ), several waves break, and the influence of the breaking is noticeable on both the energy and the PDF.

The methodology is slightly modified here: a larger domain span of  $L_x = 128\lambda_p$  is selected, while we maintain the same spatial discretization  $dx$ . The frequency discretization and bounds are also maintained. The evolution is set to 10 periods and the statistics are computed on the obtained free surface after those 10 periods. 20 equivalent runs are performed with different (random) initial phases, for a total of 2560 peak waves composed of 327 680 points.

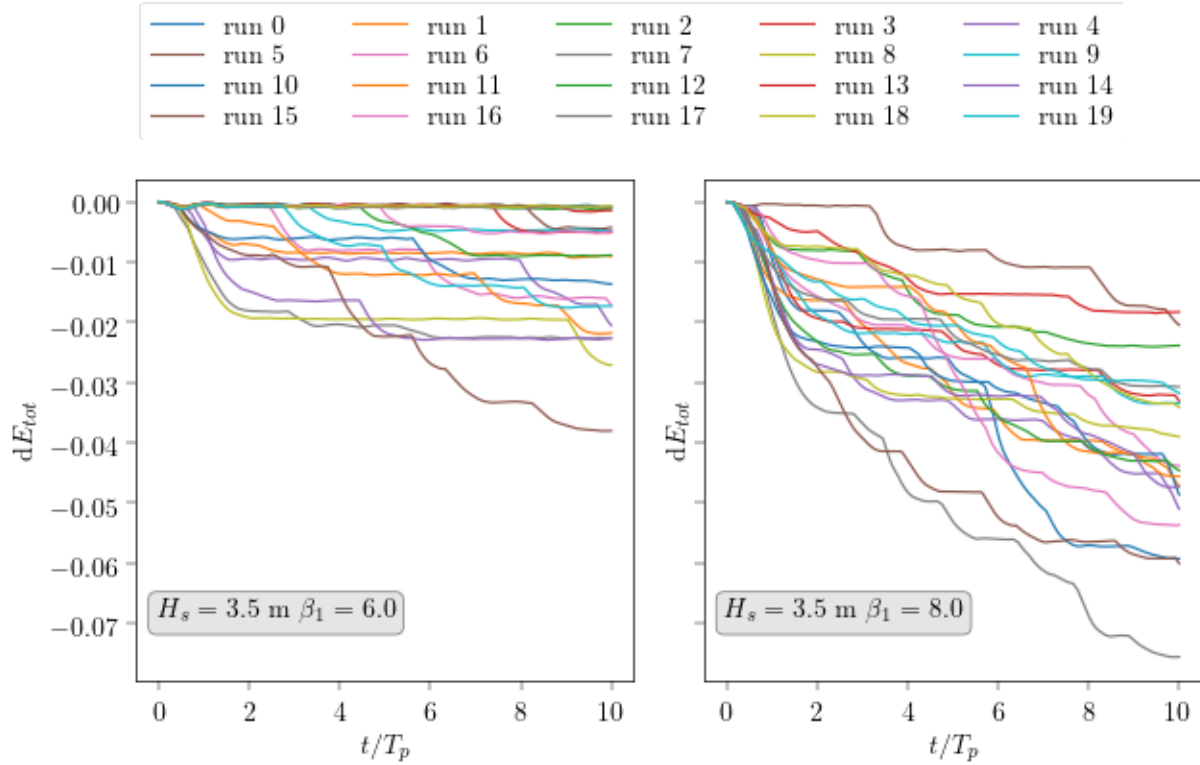


Figure 3-15. Relative energy loss during the 20 different runs, for  $\beta_1 = 6$  (left panel) and  $\beta_1 = 8$  (right panel).

Figure 3-15 shows the energy loss during the 20 runs performed with cosmhos, where the initial conditions differ due to the random phases of the selected modes. Note that the energy at  $t = 0$  is computed after the first application of the  $\beta_1$  filter which corresponds to an energy loss of 2.5% and 1.4% for  $\beta_1 = 6$  and 8 respectively. The energy loss during a given run is found to be up to 7%. The value of  $\beta_1$  is once again shown to be of prime importance.

The spatial PDFs after 10 periods of evolution are shown in Figure 3-16 for the usual variables: the free surface elevation, horizontal velocity, and acceleration at the free surface. We note that the breaking model has more influence than the filter strength, and both computations with  $\beta_1 = 6$  and 8 invoking a breaking model are in relative agreement in terms of maximum predicted values.

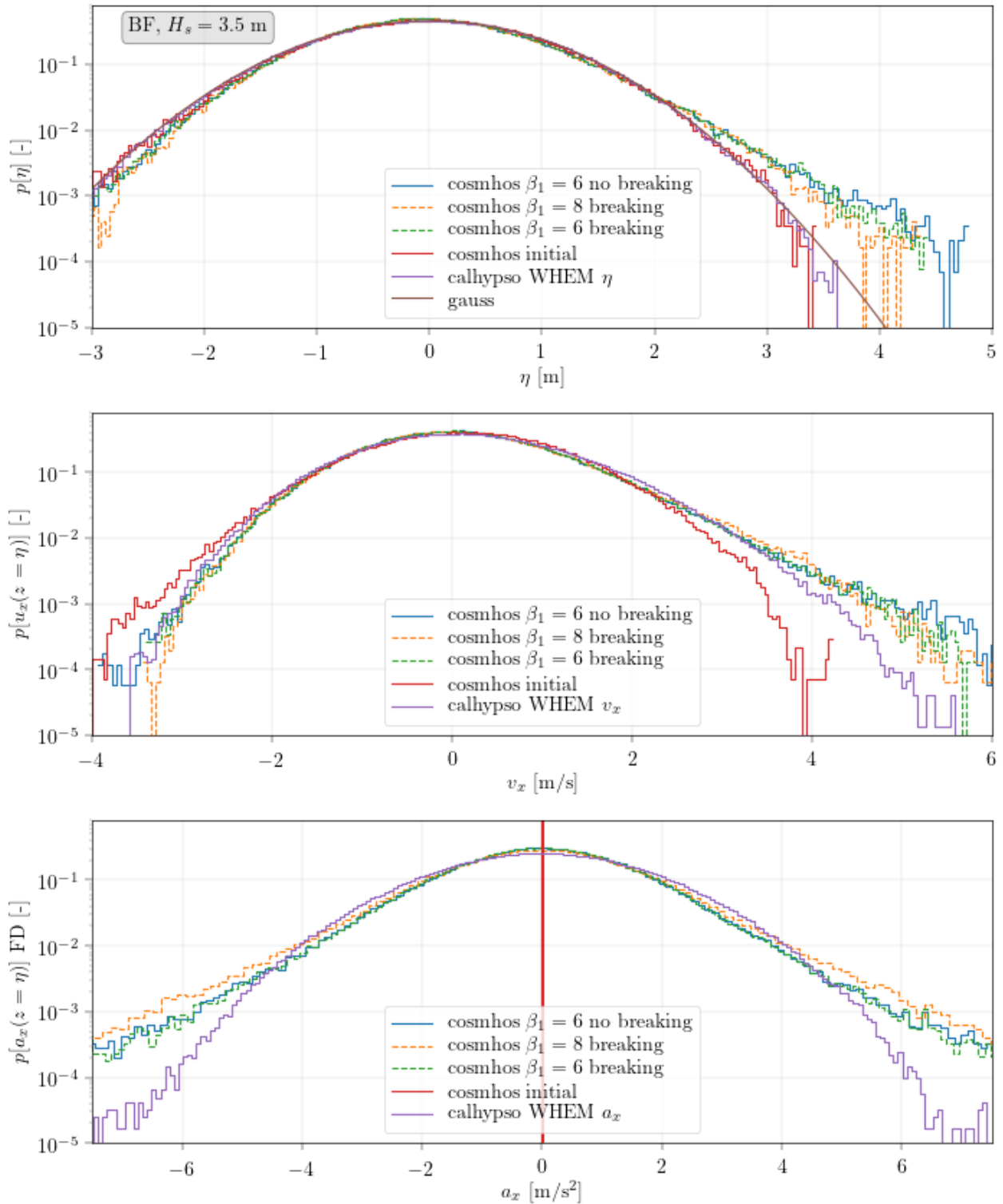


Figure 3-16. PDF of the free surface elevation (top panel), horizontal velocity (middle panel) and horizontal acceleration (bottom panel), predicted by cosmhos in 3 situations: with a breaking model and two filter strengths ( $\beta_1 = 6$  and 8), and without breaking model with  $\beta_1 = 6$ . Initial condition velocity with cosmhos at  $t = 0$  are also shown on the two first panels. Brittany Fatigue modified ( $H_s = 3.5$  m).

### 3.5.2. Breaking Brittany Fatigue, large steepness.

A test was also conducted at  $H_s = 4.5$  m, for a non-linearity parameter for the peak mode of  $H_s/\lambda_p = 6.8\%$ . The time series of the energy loss for the 20 computed runs is shown Figure 3-17. Compared to the left panel of Figure 3-15, where only the  $H_s$  differs, a significantly larger energy dissipation is found, between 6 and 12%, compared to between 0 and 4% for  $H_s = 3.5$  m.

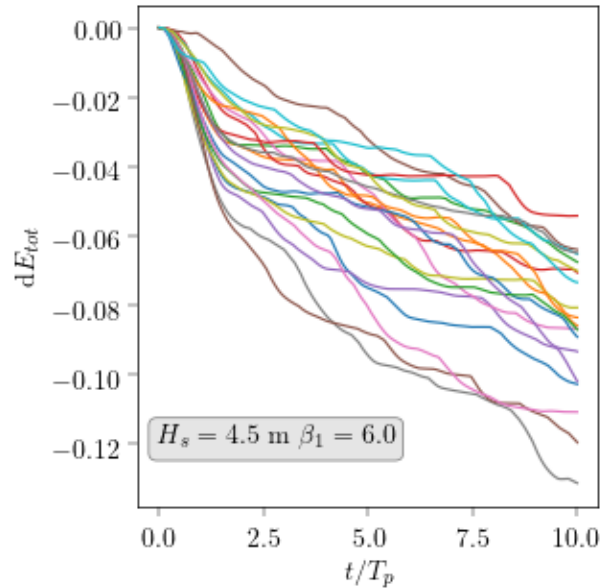


Figure 3-17. Relative energy loss during the 20 different runs, for  $\beta_1 = 6$ .

Again, we show the obtained spatial PDF of the three variables of interest in Figure 3-18, for different computation cases: cosmhos with  $\beta_1 = 6$  with and without breaking activated, as well as the linear predictions from calhypso with a WHEM model.

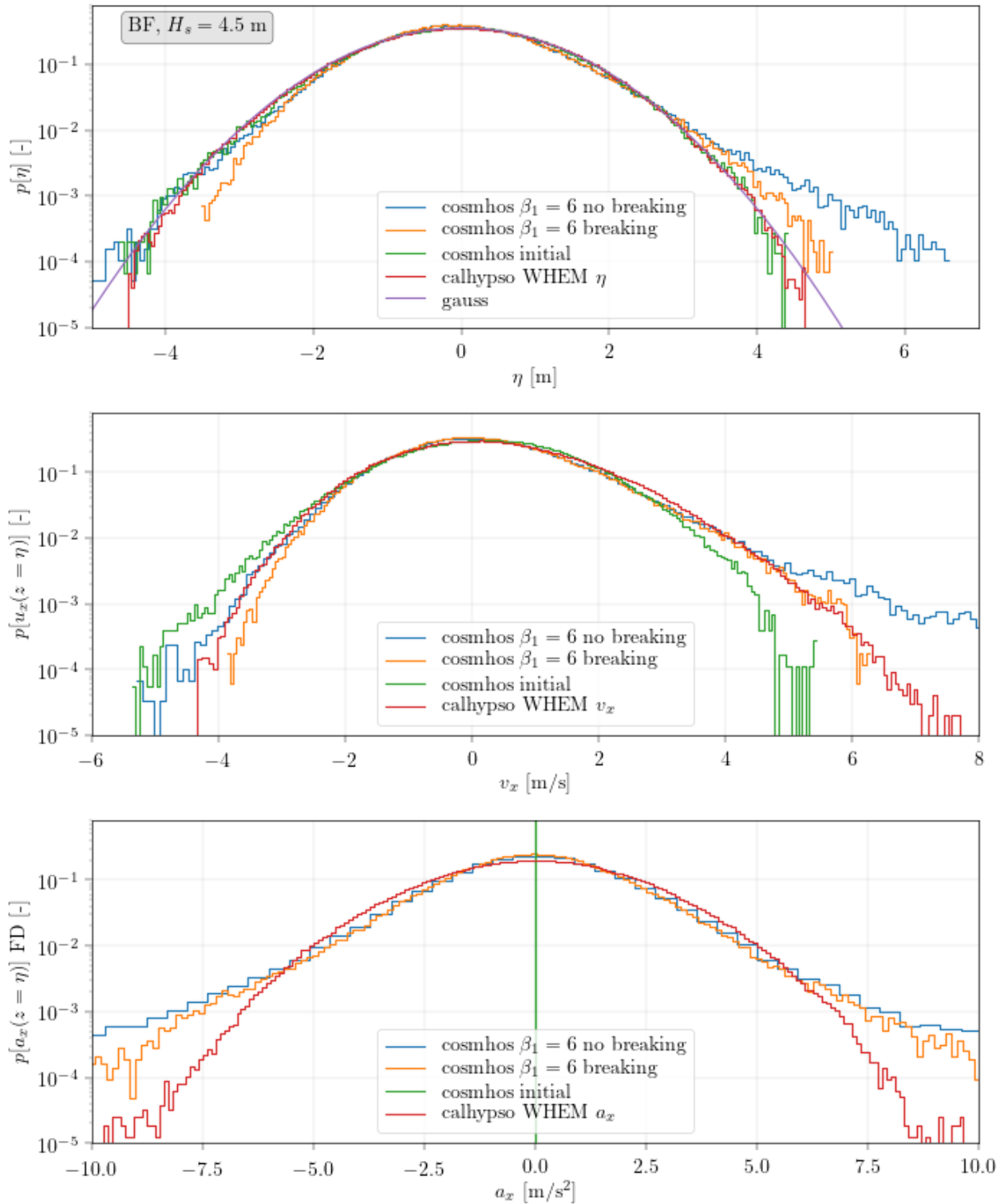


Figure 3-18. PDF of the free surface elevation (top panel), horizontal velocity (middle panel) and horizontal acceleration (bottom panel), predicted by cosmhos in 3 situations: with a breaking model and one filter strength ( $\beta_1 = 6$ ), and without breaking model with  $\beta_1 = 6$ . Initial condition velocity with cosmhos at  $t = 0$  are also shown on the two first panels. Brittany Fatigue modified ( $H_s = 4.5$  m).

### 3.5.3. Discussions

The wave breaking is shown to act in the same manner as the filter: whether  $\beta_1 = 6$  or 8, the surface elevation, velocities and accelerations seem to be equal when the breaking is activated. This is positive, given the fact that the breaking formulation is a model and is based on physical grounds instead of a purely numerical one.

Velocities and free surface elevations seem to be correctly computed, with a behavior that does not exhibit too many spurious values. Once again, the linear model does not manage to capture the extrema of the free surface elevations, due to the linear assumptions, but the WHEM model seems to be in better agreement compared to the cosmos+breaking than it was for a non-breaking case.

Finally, the accelerations encountered in both cases do not seem to really decrease from the activation of a breaking model. This can be partly explained stating that the breaking model mostly acts at the maxima of the free surface elevation. However, the maxima of the accelerations are not located at these moments and locations.

### 3.6. Summary and conclusions – kinematics studies.

To compare the influence of the different parameters and estimate a dispersion in terms of predicted free surface elevation and kinematics, we extract from every probability density function presented above the highest values associated with a probability of  $1e^{-4}$ . For example, for  $\eta$ , this function is given by:

$$f_{\eta} = \max(\eta) ; pdf(\eta) > 10^{-4} \quad (6)$$

Note that the *pdf* is filtered out, to remove spurious values that could lead to an overestimation. The results for all the computed cases are given in Figure 3-19. The different physical cases (BF, BS, TF, TS) are separated by a wide vertical line. In the same manner, the study assessing the influence of the wave breaking (BFb) is also separated because the significant wave height was modified compared to the non-breaking original case (BF). Free surface elevations, horizontal velocities along  $x$  (and  $y$  when nonzero), and accelerations are shown.



significant when focusing on the accelerations. For the other cases (BF, BS, TF), only  $\beta_1 = 10$  is considered unstable.

However, even with  $\beta_1 = 6$ , we find that the values of  $\eta$ ,  $v_x$  and  $a_x$  are underpredicted with the linear theory whatever the stretching model used. While the linear theory underpredict the maximums of the free surface elevation by 10 to 15%, the underestimation on the kinematics is higher: up to -20% compared to an HOS simulation with a relatively strong filter ( $\beta_1 = 6$ ). The main parameter influencing the underprediction in free surface elevation is the relative wave height  $H_s/\lambda_p$ . Indeed, the selected cases are outside the range of the linear assumptions but increasing  $H_s/\lambda_p$  is shown to increase the error committed of the maxima of  $\eta$ . This effect is however less pronounced when regarding the velocities and accelerations. The underprediction of the velocity seems to be less pronounced for smaller water-depth  $h/\lambda_p$ , probably explained by the stretching model that is not independent of the relative water depth.

Errors committed on the accelerations are more difficult to assess, mostly because of the difficulty to compute them with the nonlinear model. Indeed, the TS case, i.e.  $H_s/T_p = 5.8\%$  seems to lie outside of the validity range of the acceleration computation method. For the other cases, the behavior of the error committed on the acceleration seems to match the one of the error on the velocity: large water depth leads to a larger error, and more specifically, to a large underprediction of the maxima of the accelerations (-17%).

On the contrary, studying a 2D wave field as if it were 1D, with all the energy along one dimension axis leads to an overestimation of the kinematics. As was to be expected, it is also shown that the larger the spreading, the larger this overprediction. Note that the free surface elevation is not impacted and only the kinematics are overpredicted.

The usual choice of selection of deterministic amplitude for the different modes seems to be unimpactful on any of the three studied variable. Indeed, the difference between “random amplitudes” and “deterministic” amplitude is always lower than a few percent, at any chosen probability as long as the results are statistically converged.

Wave breaking model is shown to largely affect the free surface elevation and kinematics at crest, especially when the significant wave height becomes large, leading to a large dissipation of the energy. In rough sea states, typically  $H_s/\lambda_p \sim 6\%$ , the breaking leads to a large reduction of the crest velocities, mainly by eliminating the spurious values of velocities, acting as a physical filter.

Possible future extensions and continuation of this work might focus on different aspects to refine the obtained results:

- Testing the influence of the directionality of the spectrum directly with the nonlinear HOS model. This would come at a larger cost but would allow to estimate the combined effect of nonlinearity and directionality, compared to linear approaches.
- Testing the different stretching models on a spectrum extracted from the nonlinear free surface elevations. This would be very interesting to separate the effect on the kinematics. The underlying question is which part of the underprediction of the kinematics arise from the underprediction of the free surface elevation and which part originates from the stretching model itself.
- Filtering only local maximums before the statistical analysis. This would avoid to pollution of a large wave that could alone, have 20 points in a low probability region.

## 4. Influence of bathymetry – A non-hydrostatic multilayer wave model

### 4.1. Introduction

Propagation of phase-resolved waves in the coastal zone can be a challenging numerical task. As shown in the previous chapter, HOSM is capable of simulating steep ocean waves in fairly shallow water depths, accounting for wave breaking through a breaking model.

Variable bathymetry and the introduction of a coastline, like the one shown in Figure 4-1, increases the complexity of the problem and has a profound impact on the wave field. Coastal effects such as reflection from shore, diffraction, bottom friction and sudden shifts of water depth led to frequent occurrence of wave breaking and significant wave energy dissipation. Furthermore, the introduction of variable bathymetry and the coastline challenges one of the fundamental assumptions for the HOSM simulation, which is using spatial periodic domains, since variable seabed by nature is rarely periodic. Non-periodic sea bed variation can however be overcome by workaround-techniques like domain mirroring and the introduction of transitional zones (Ref. [24], [54]–[56]), at the expense of increased computational time. Modelling the coastline, however, proves difficult in a HOSM simulation.

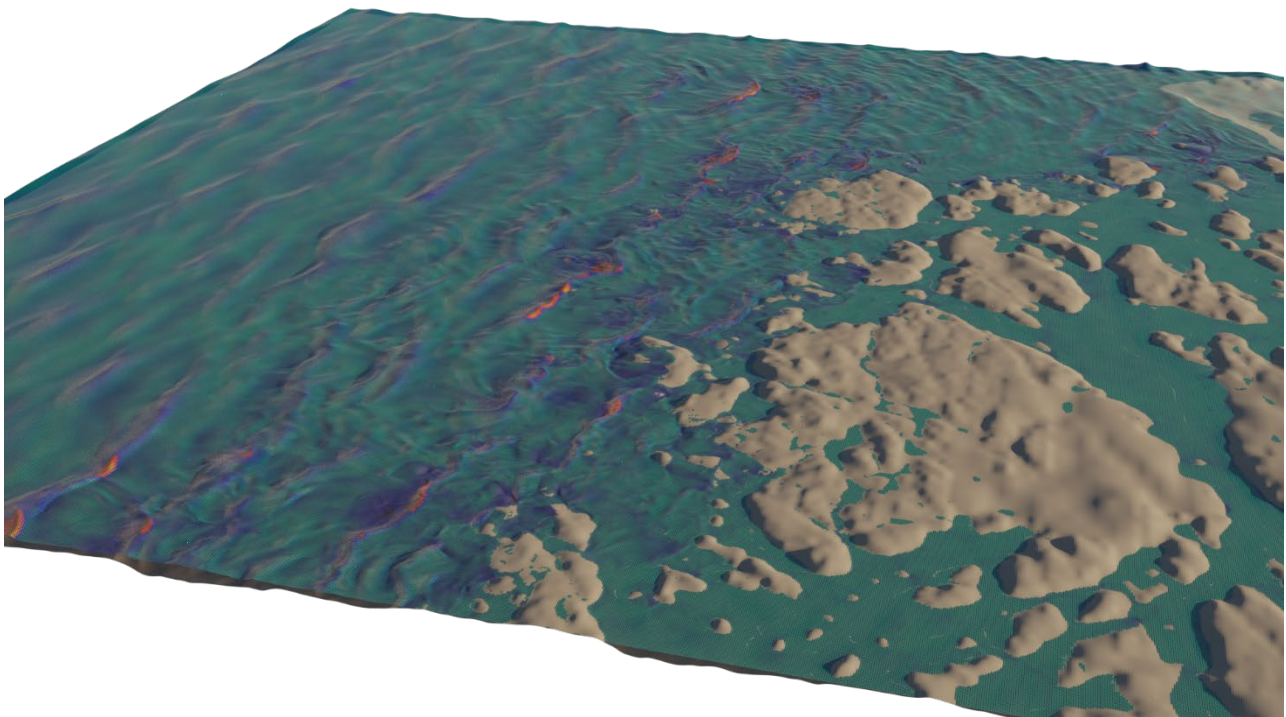


*Figure 4-1 non-hydrostatic multilayer model coastal wave simulation*

For this type of problem, a different wave model is sought. Historically, wave modelling using shallow water equations or Boussinesq-type models have been used for simulation of waves in coastal conditions. Examples of this are given in Reference [57], [58] and [59].

With no requirement for periodicity in space and simulating only the sea surface (single layer models), these models may seem well suited for the task. However, the drawback is their ability to model waves in

deeper waters. Using shallow water wave models, based on the shallow water equations first derived by Saint-Venant using conservation of mass and momentum in vertical slices, the vertical pressure profile is assumed essentially hydrostatic, and a constant vertical velocity profile which makes the code incapable of modelling wave dispersion [1].

The Boussinesq approximation [60] for water waves takes into account the vertical structure of the horizontal and vertical flow velocity. This results in non-linear partial differential equations, called Boussinesq-type equations, which incorporate frequency dispersion. As a result, Boussinesq-type models are capable of weak dispersion and are suitable for modelling long waves. Many improvements and variations of the Boussinesq-type models have been developed over the years to improve its ability for wave dispersion by introducing higher order terms[61], or layers [62] at the expense of performance and stability.

In the late 1990's and early 2000, the non-hydrostatic multilayer model was introduced to coastal engineering as an efficient alternative to the Boussinesq-type models frequently used at the time for wave modelling. Reference is made to the work of Sterling and Zijlema [63], [64] and Casulli [65], which lead to the development of the open source non-hydrostatic multilayer wave model SWASH [66].

In the present work, the wave model is built on the basis of the non-hydrostatic multilayer solver published more recently by Stéphane Popinet [1].

## 4.2. Solver

The core solver applied when propagating waves onto shore is a vertically-Lagrangian multilayer solver for free-surface flows [1], provided by the open-source library of differential solvers, Basilisk [67].

The solver discretizes the domain vertically into Lagrangian layers, while horizontally a static cartesian grid is used. This results in a semi-discrete approximation of the incompressible Euler equations with a free-surface and gravity

$$\begin{aligned}\partial_t h_k + \nabla \cdot (h\mathbf{u})_k &= 0 \\ \partial_t (h\mathbf{u})_k + \nabla \cdot (h\mathbf{u}\mathbf{u})_k &= -gh_k \nabla \eta - \nabla (h\phi)_k + [\phi \nabla z]_k \\ \partial_t (hw)_k + \nabla \cdot (hw\mathbf{u})_k &= -[\phi]_k \\ \nabla \cdot (h\mathbf{u})_k + [w - \mathbf{u} \cdot \nabla z]_k &= 0\end{aligned}$$

with  $k$  the index of the layer,  $h_k$  its thickness,  $\mathbf{u}_k$  and  $w_k$  are the horizontal and vertical components of the velocity,  $g$  the acceleration of gravity,  $\phi_k$  the non-hydrostatic pressure (divided by the fluid density),

$$\eta = z_b + \sum_k h_k$$

is the free-surface height, with  $z_b$  the height of the bottom topography,

$$z_{k+1/2} = z_b + \sum_{l=0}^k h_l$$

is the height of each layer interface, as seen in Figure 6.

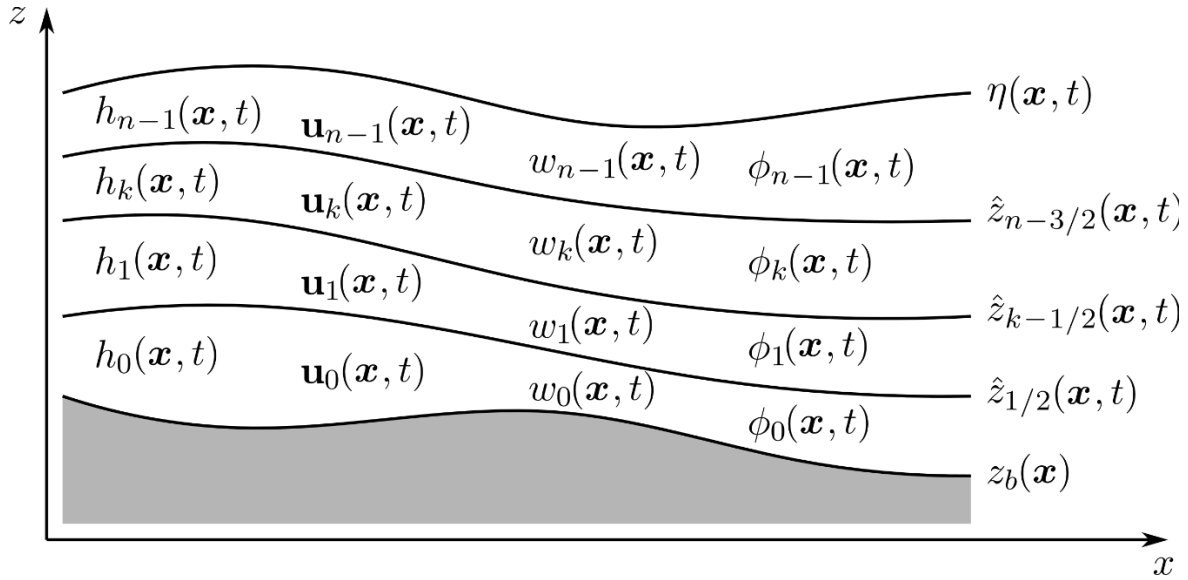


Figure 4-2 Multilayer discretization scheme (Figure obtained from [1]).

From this definition the implementation of variable depth is done through the scalar field variable  $z_b$  which varies with position  $(x,y)$ . By using multiple layers distributed with a higher density close to the free surface, the vertical velocity and pressure profiles may be accurately modelled. The solution is therefore very capable of modelling wave dispersion of short waves, using a limited number of layers, as it will be shown in the validation sections below. Furthermore, the sigma-coordinate based vertical-Lagrangian structure of the layered mesh makes it straight forward to add complex variable bathymetry.

The drawbacks of this model are few. The most obvious one is the addition of the layer thicknesses as prognostic variables. The added complexity and computational cost are low however, since they are passive tracers which will be transported using the same scheme as other tracers [1].

Using a projection scheme for time-stepping, the non-hydrostatic multilayer wave model is indeed closer to CFD than being a single layer model. As a result, the model requires more CPU time than HOSM, but significantly less than traditional Volume-of-fluids CFD models. The multilayer model provides a good overlap and extension of the HOSM model in terms of applicability, as illustrated in Figure 4-3.

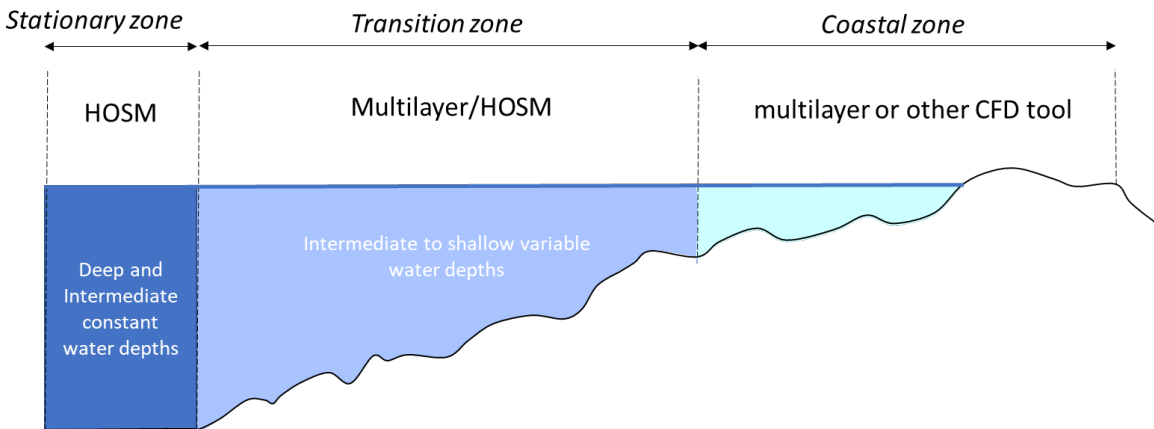


Figure 4-3 Visual illustration of analysis approach

### 4.3. Boundaries

A practical problem when propagating waves in shallow water is to find a good theoretical description to provide as input at either the inflow boundary, or when initializing the domain, as illustrated in Figure 4-4. For this purpose, one of the main motivations for developing the multilayer wave model was to propagate waves from deep/intermediate water depths and into the shallows, where conventional theories such as second order irregular wave theory [68], or even higher order methods such as HOSM can be used to provide the solution at the inflow boundary.

The second major part of the wave model is thus the boundary kinematics library CFDwavemaker [67]. CFDwavemaker is another open source, purpose-built library for generation of higher order irregular and short-crested waves for input to CFD-type programs. The library has several wave theories implemented and allows for reading of spectral component results from HOSM simulations and compute kinematics at each time-step at the boundary. Reference is made to the user manual of CFDwavemaker, Ref. [69].

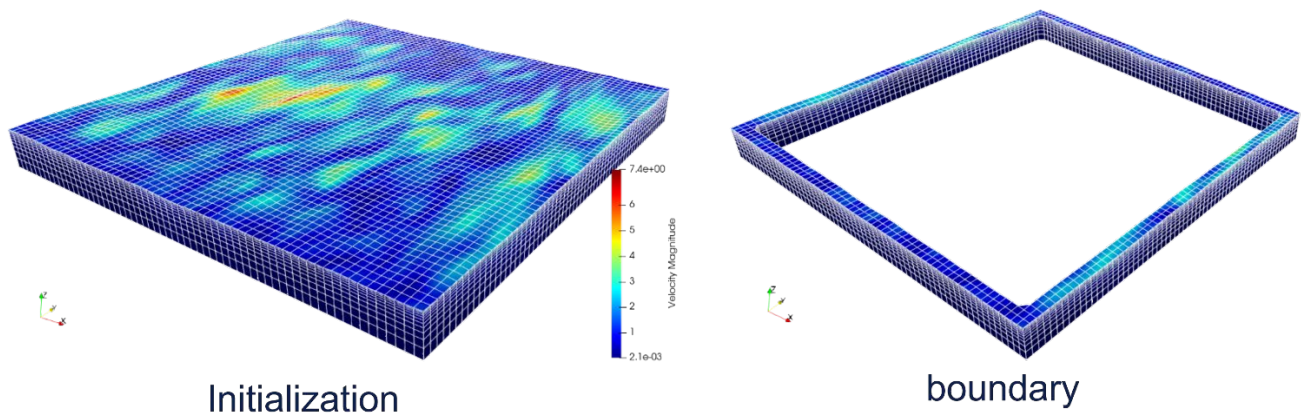


Figure 4-4 The two alternatives for wave propagation in a simulation domain

## 4.4. Validation cases

### 4.4.1. General

Validation of numerical tools are and should be considered an essential part of the model development. When dealing with complex numerical models, numerical dissipation and convergence, instabilities and other sources of inaccuracy may lead to substantial differences in output. It is thus extremely important to validate models before applying them for actual engineering tasks. In the present section, 4 validation cases are presented. In each case the multilayer wave model is validated against model test measurement data.

### 4.4.2. Crest distributions for intermediate and deep waters

Based on event-based approach discussed in section 2.5.1, the multilayer wave model was run and compared with HOSM simulations of the same events, for a range of different sea states covering deep and intermediate water depths. HOSM was run using a breaking model with  $U_c = 0.85$  and  $\alpha = 0.02$ . Unlike

HOSM, the non-hydrostatic multilayer model does not rely on a breaking model to limit crests heights to physical bounds. Like other CFD programs, waves will break when becoming too steep in the multilayer simulations.

For validation, crest distributions for 10 different sea states, where model test data was available, were simulated. Since we are primarily interested in the tail of the short-term crest distributions (events with low probability of occurrence), a cut-off on linear crests simulated in HOSM/multilayer was set to  $H_s/2$ . Approximately 1000 events are run for each sea state, giving sufficient events to populate the lower tail of the crest distribution. Each event was initialized using second order wave theory and started approximately  $3 \cdot T_p$  before the occurrence of the event, to allow the wave to modulate, amplify and break if becoming too steep.

The resulting crest distributions from the non-hydrostatic multilayer model (red dots) and HOSM (green dots) are presented in Figure 4-5 and Figure 4-6. The experimental data (black dots) are plotted as black dots, while the Forristall crest distribution [30] are plotted as a blue line, mainly for reference. The underlying linear representation of the events simulated in HOSM and the multilayer wave model are shown as orange dots. The sea-state parameters  $H_s$  and  $T_p$ , as well as the corresponding sea-state wave steepness  $S_p = H_s k_p / 2$  are indicated in each plot.

As seen from the figures, the agreement between HOSM and the multilayer model is very good for all compared sea states.

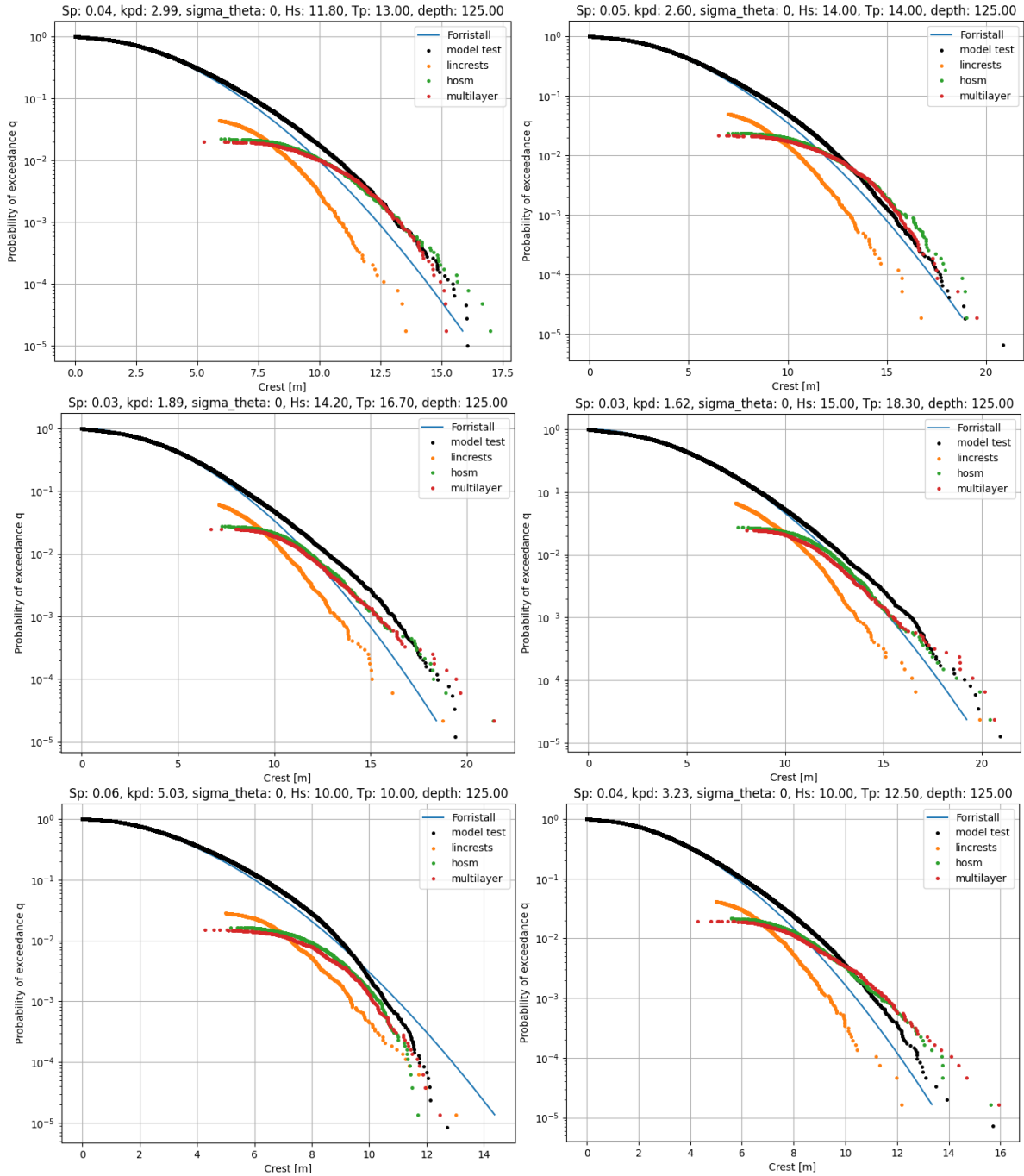


Figure 4-5 Crest distribution comparison for sea state 1-6 (out of 10). All sea states are long-crested, for deep and intermediate constant water depth.

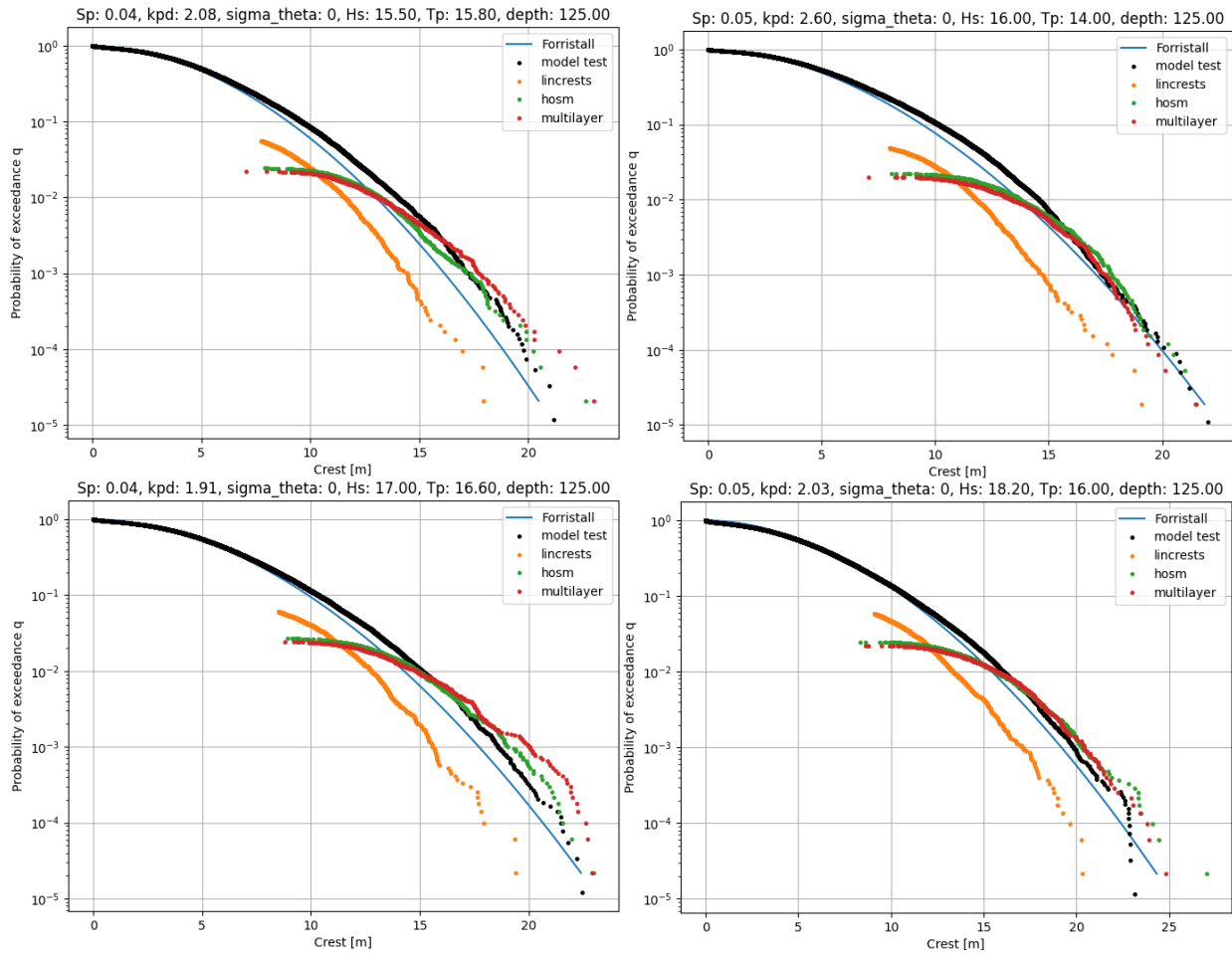


Figure 4-6 Crest distribution comparison for sea state 7-10. All sea states are long-crested, for deep and intermediate constant water depth.

### 4.4.3. Deterministic comparison of irregular wave propagation and crest kinematics

One of the key features of the multilayer model is its ability to propagate waves at any water depth (short wave dispersion). No assumptions are needed on the pressure/velocity profile underneath the surface, since the velocity profile is resolved, provided that enough layers are used. This makes the multilayer model capable of propagating strongly dispersive waves, something which is challenging using single-layer models [57].

To illustrate this, a comparison to the model test experiments of Johannessen [70] was run, where a focused wave group, strongly dispersive, was simulated using the multilayer solver. The chosen waves are steep, but non-breaking and the amplitude was set close to the very limit to where wave breaking (spilling) was observed in the laboratory.

The simulation domain was 10.5 meters long, where the linear focus point was set to 4.8 meters from the wave maker. With a mean wave period of about 1 second, the wave group is allowed to propagate

approximately  $3\lambda_p$  before passing the focus point. A screenshot of the simulation domain is shown in Figure 4-7, showing the stretched vertical-Lagrangian grid used in the multilayer simulation.

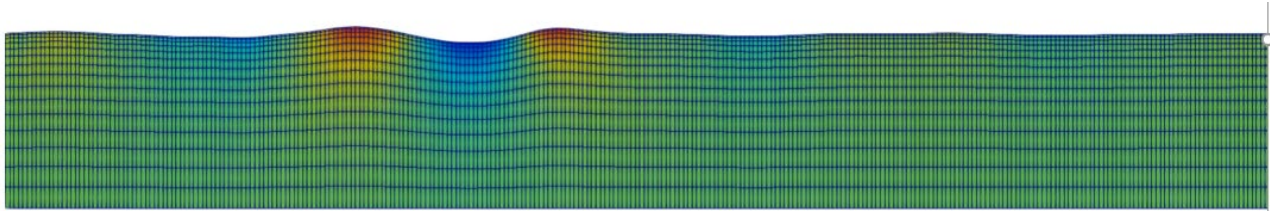


Figure 4-7 Snapshot of multilayer model grid when simulating irregular focused wave event

The selected wave event has a linear target amplitude of 61 mm, and 28 frequencies, where the spectral shape is given by

$$a \propto f^{-2}, \text{ for } \frac{53}{64} \leq f \leq \frac{80}{64}$$

using a water depth of 1.2 m.

Due to higher order modulation of the wave however, the focus point of the wave will shift downwave in the basin, and the measured maximum amplitude becomes significantly steeper than the linear target (as expected).

Figure 4-8 and Figure 4-9 show the wave time-series measured at different locations in the basin, where the black dots are the model test measurements, the blue line the multilayer model, and the green line the second order theoretical solution. The second order solution was used as input at the inflow boundary of the multilayer solver.

The modulation of the wave groups is an effect which is not captured by second order wave theory despite being frequently used for dispersive wave propagation in engineering. The multilayer model, however, is indeed capable of capturing this beyond second order wave interaction effect, and results in a significantly better match with the model test measurements. The results are indeed similar to what was obtained using other fully nonlinear CFD codes [71].

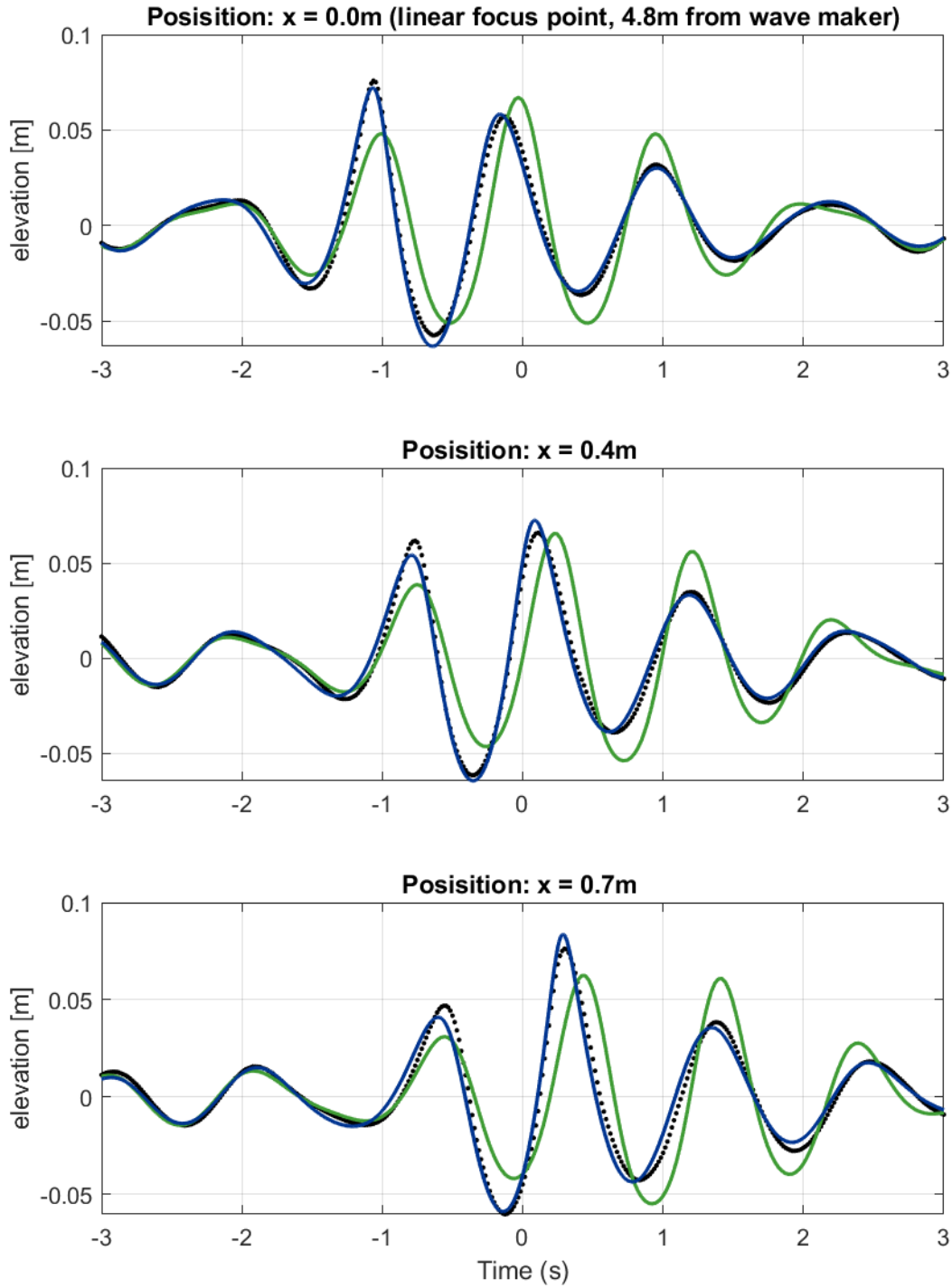


Figure 4-8 Unidirectional focused steep wave event 61mm amplitude (model scale) - Wave gauge 1 to 3. Black dots = model test, blue line= multilayer model, green line= second order wave theory

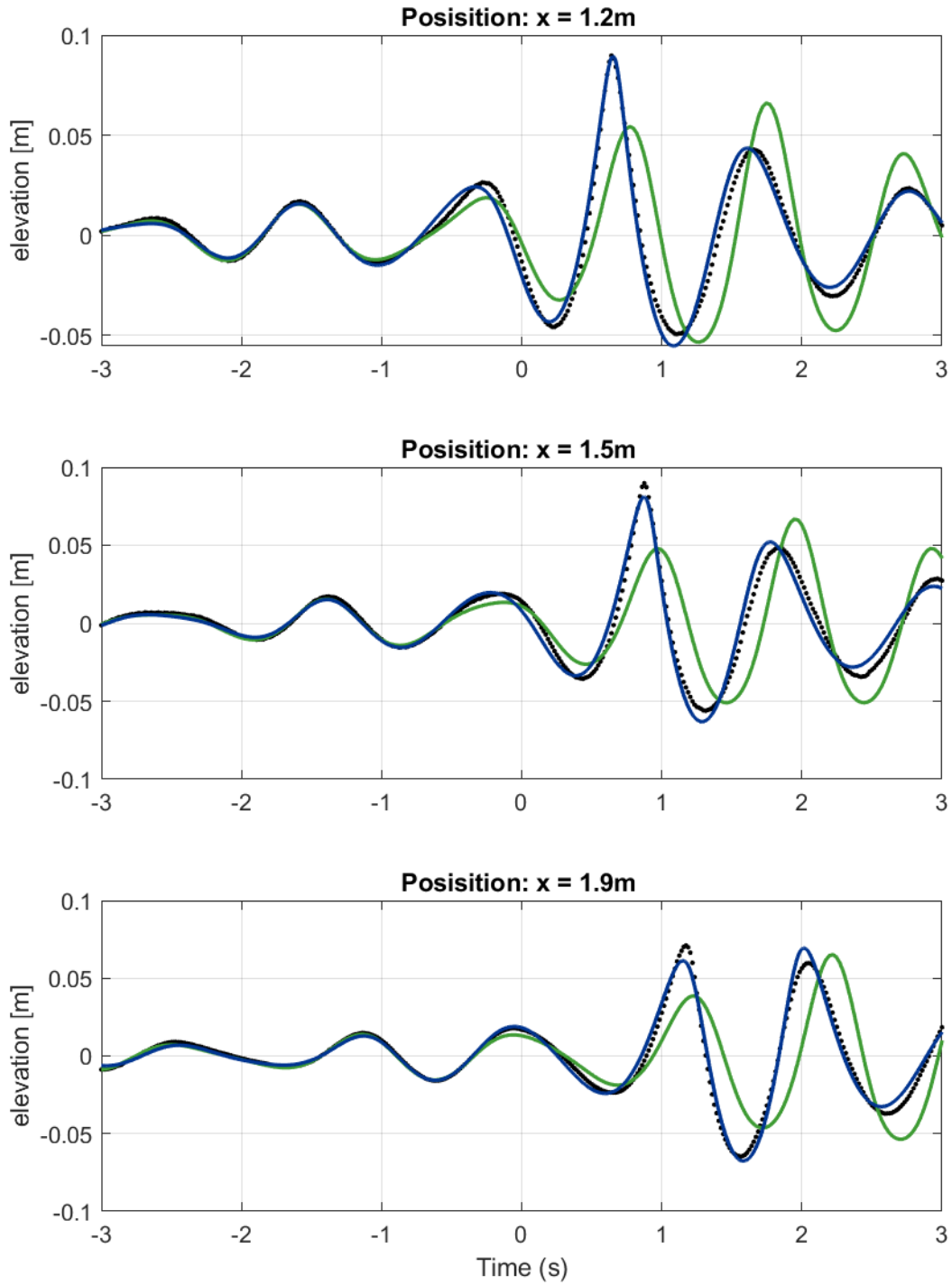


Figure 4-9 Unidirectional focused steep wave event 61 mm amplitude (model scale) - Wave gauge 4 to 6

#### 4.4.4. Significant wave height along an uneven sloping seabed

As part of the PhD work of M. Boers, a series of shallow water tests, propagating waves onto an uneven slope with a small barrier, was conducted [72]. The seabed profile is shown in Figure 4-10. The simulated condition had the following sea state characteristics:

Hs: 0.1m (model scale)

Tp: 3.4 sec (model scale)

$k_p d$ : 0.53

Due to the shallow water depth of this experiments, the wave elevation measured at  $x=0$ , was reconstructed using HOSM, using the procedure described in Ref. [73], [74]. A snapshot comparison of the measured wave and the HOSM reconstruction is illustrated in Figure 4-11.

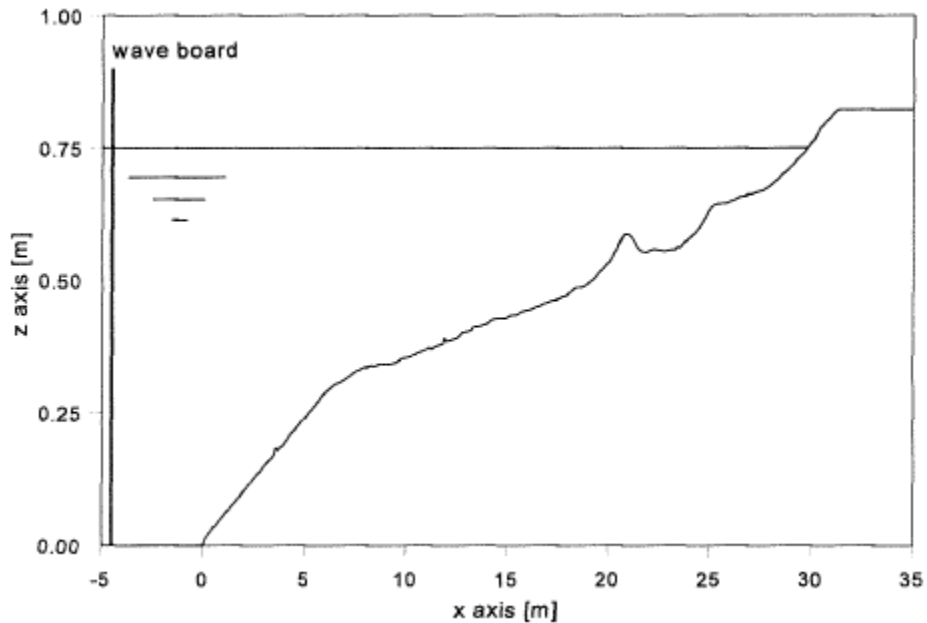


Figure 4-10 Beach profile (compressed x-axis) used in Boers experiments [72], with a small underwater barrier at approximately 22m.

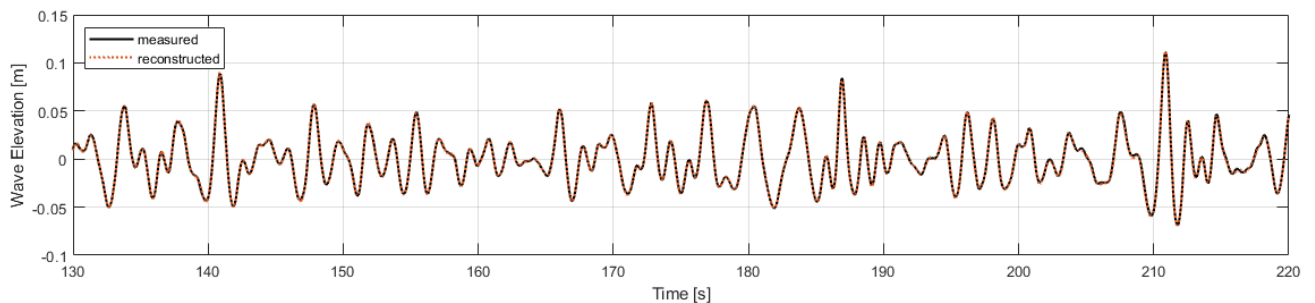


Figure 4-11 Reconstructed wave in HOSM (black=measured input wave, red dots=reconstructed HOSM wave)

The actual measured wave-gauge time-series from the model test were not available for comparison, but the spectral parameters, as a function of position were obtained from [72]. The values have been compared against simulation results, and are presented in Figure 4-12.

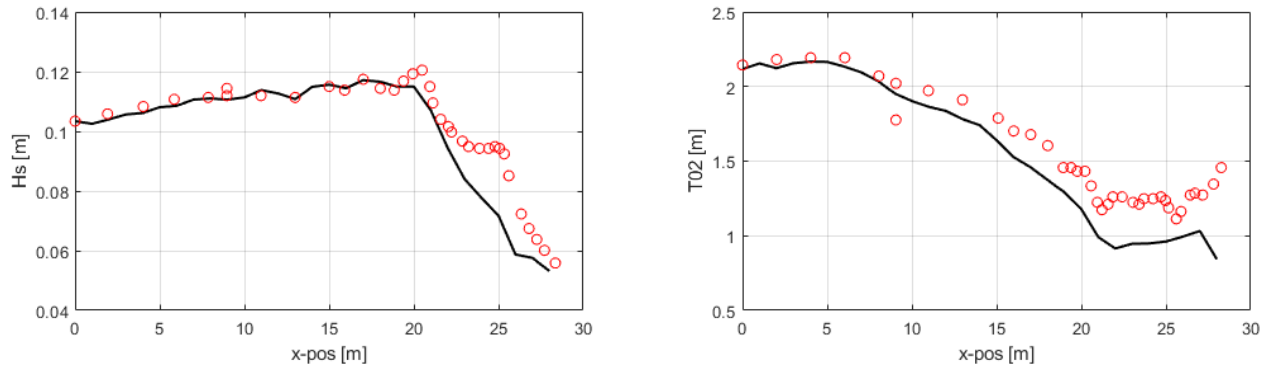


Figure 4-12 Comparison of measured significant wave height (left plot) and spectral mean period calculated from the second moment (right plot). The red dots marks the measurements obtained from the model test report [72], while the black line is the results measured form the multilayer simulation.

#### 4.4.5. Crest distributions along a sloping bottom

To validate the crest distributions for in-homogenous conditions, a series of shallow-water wave tests performed as part of the master degree work of Erik Svangstu [75] was used as a validation case. The model length scale has been chosen as 1:81, implying a time scale of 1:9. The test was conducted in a small towing tank, lowering a tilted solid rectangular box shape, open in each end, into the basin, as illustrated in Figure 4-13. Flow was thus allowed to pass under the box, which minimized the backflow on the sloping bottom.

Of the many sea states and realizations tested, the two realizations given in Table 4-1 were simulated using the non-hydrostatic multilayer model. Both sea states have the same spectral peak period, but different steepness. The model test domain and the location of each wave probe is illustrated in Figure 4-13. Each test was roughly 2.3 hours full scale.

Table 4-1 Sea state parameters

| Test ID | Significant wave Height [meters] | Spectral peak period [seconds] | Simulated time [seconds] |
|---------|----------------------------------|--------------------------------|--------------------------|
| 2114    | 5.67                             | 13.5                           | 900                      |
| 2115    | 8.51                             | 13.5                           | 885                      |

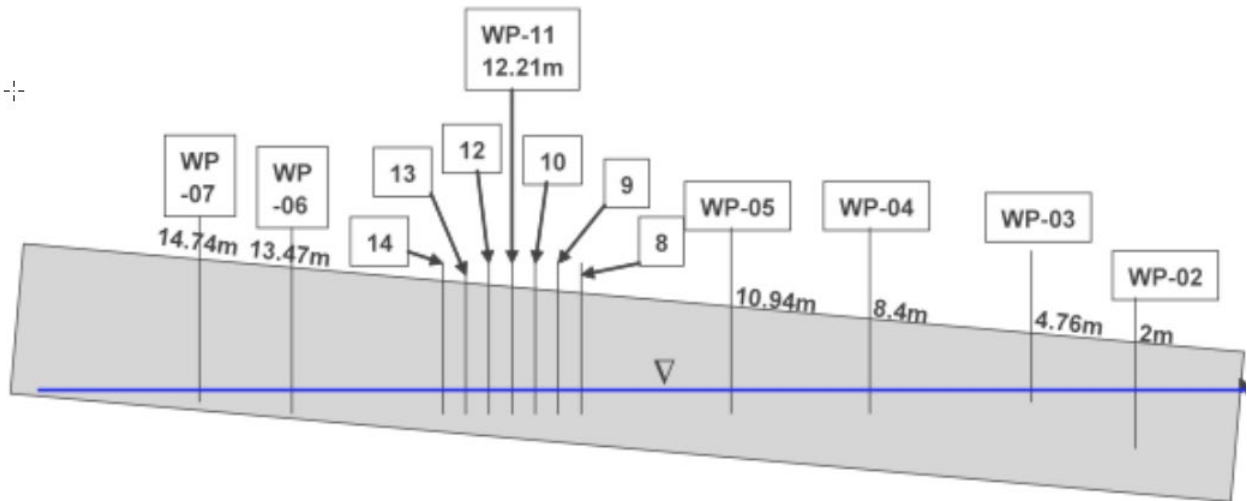


Figure 4-13 Sloping bottom model test setup (illustration from [76]) and wave gauge locations (wave propagation direction from right to left)

The wave input at the boundary was specified by HOSM reconstruction [73], [74] of the measured time-trace at WP-02. The simulation domain thus starts at the position of WP-02. Wave paddle movement and wave maker theory is a possible alternative for computing the wave kinematics to apply, but in these tests the wave paddle movement was not recorded.

The simulation domain is modelled using a constant slope, equivalent to the slope of the model test, however the backflow is not allowed to circulate back, since it was no practical way of modelling this using the multilayer solver. Instead, the domain was extended, beyond the point where the seabed penetrates the surface, and a drain applied at the outflow end of the basin, as illustrated in Figure 4-14. The domain extension and drainage had a positive effect on reducing backflow, but not sufficient to eliminate it. For steeper sea states, backflow increases and will eventually cause the simulation to become unstable at the inflow boundary. This is shown in Figure 4-15 and Figure 4-16, which shows two snapshots in time for test2116<sup>1</sup>. After 270 seconds, the backflows influence on the velocity field is clearly visible. This is indeed also the case for lower sea states and is likely to affect the results.

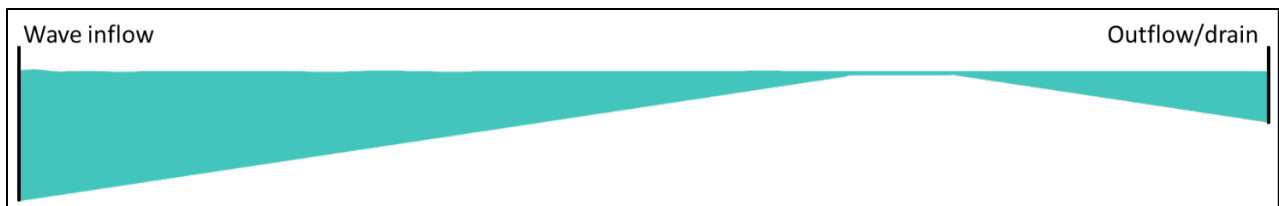


Figure 4-14 Simulation domain (from left to right)

<sup>1</sup> Test 2116 had a  $H_s$  of 11.34m (full scale)

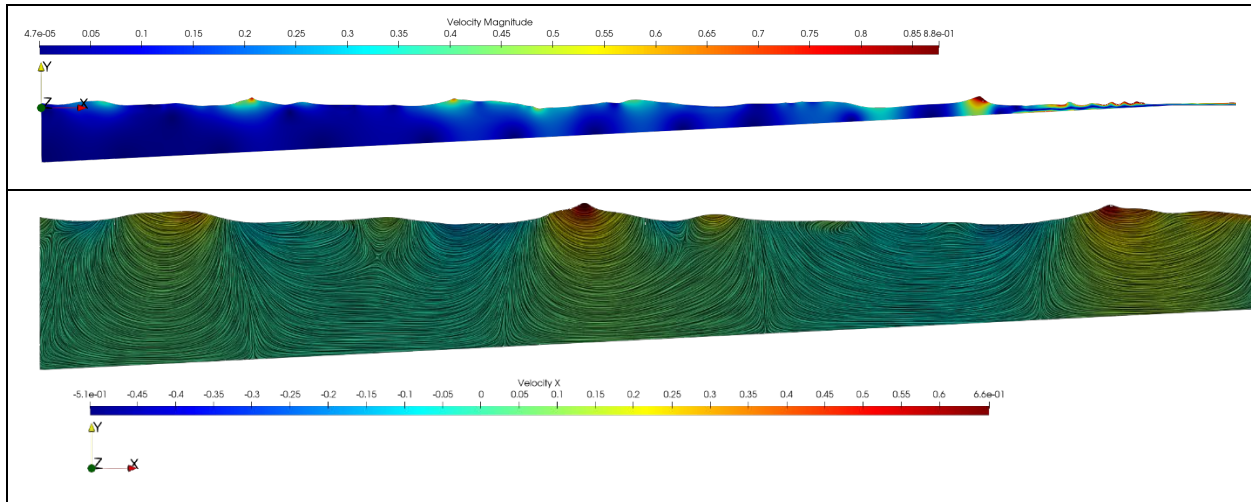


Figure 4-15 Simulation screenshot  $t=42$  sec from test 2116. (Time in model scale). Upper plot shows the complete domain, while the lower plot is zoomed in on the first 10 meters of the basin. Line integral convolution (LIC) is used to visualize flow patterns.

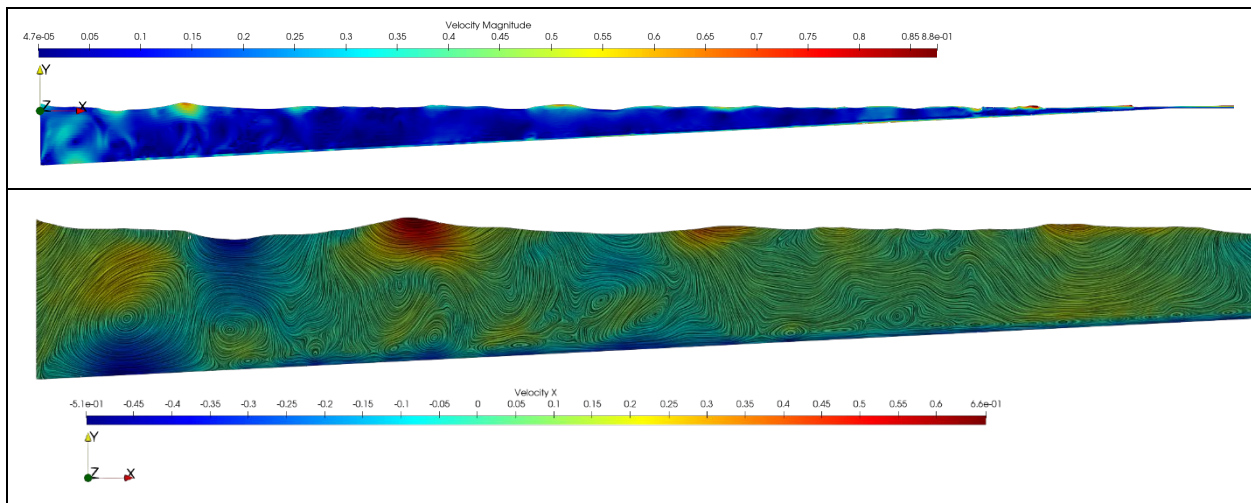


Figure 4-16 Simulation screenshot  $t=270$  sec from test 2116. (Time in model scale). Upper plot shows the complete domain, while the lower plot is zoomed in on the first 10 meters of the basin. Line integral convolution (LIC) is used to visualize flow patterns. Backflow (along the sloping bottom) will over time cause substantial vorticity to build up in the fluid domain, which is clearly visible in the screenshot.

Figure 4-17 and Figure 4-18 present a comparison of spectral parameters for the two simulated sea states. Significant wave height  $H_s$ , Mean wave period (computed from spectral moments), kurtosis and skewness, are plotted as function of position in the basin. All values are given in model scale. The black lines are recordings from the multilayer simulation, while the red lines show the measured model test values.

For the lower of the two sea states (test2114), the match is very good. The skewness level is marginally higher in the simulations but show the same trend as the model test (increasing with reduced water depth). For test 2115 the match is less good, but still within acceptable range, considering the model setup differences. Significant wave height reduces faster in the simulation as the waves propagate towards shore.

One likely cause of this is the backflow-problem previously discussed. Another cause may be inaccuracies in the reconstructed inflow wave. Generally, the steeper the sea state, the more challenging it is to reconstruct using HOSM.

Figure 4-19 and Figure 4-20 show spectral density for 8 locations spanning the basin. Again, the match is very good for test 2114, while for test 2115 energy seems to drop faster than in the model test.

Finally, crest distributions for tests 2114 and 2115 are shown in Figure 4-21 and Figure 4-22. The match between simulation and test is generally very good. The exception is the last wave gauge for test 2115, where clearly the crest distribution is lower. This is as expected given the reduction in wave energy observed in Figure 4-18.

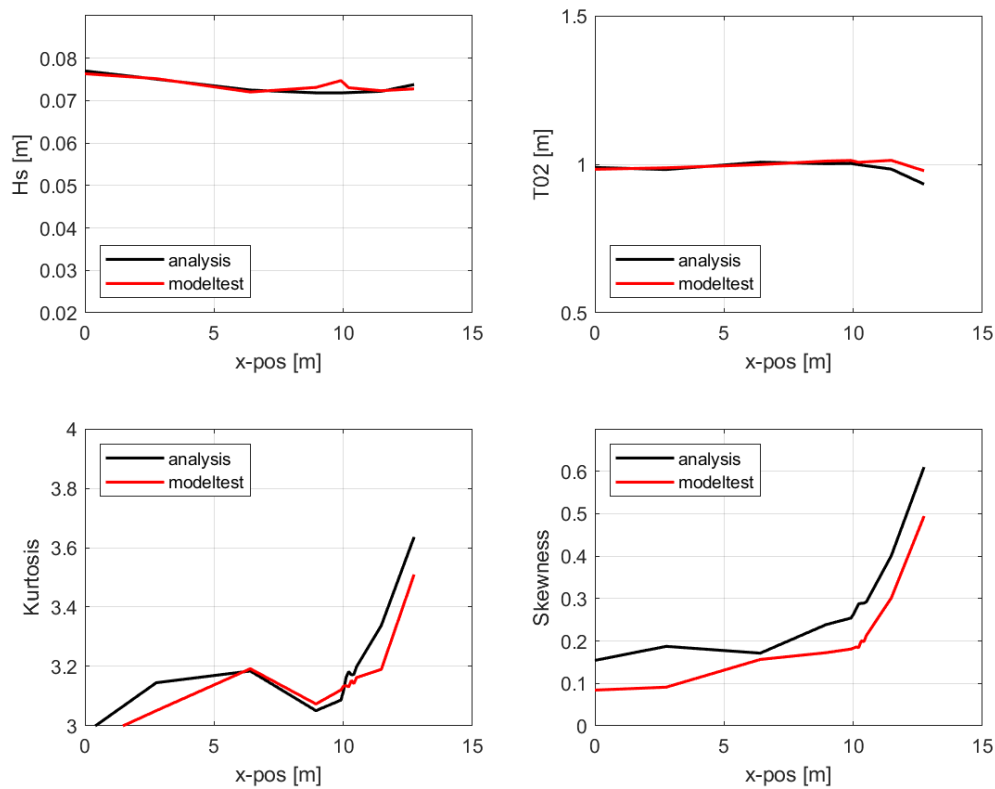


Figure 4-17 Spectral parameter variation, as a function of position in the tank, for test 2114. Reference position ( $x=0$ ) is in this case WP-02.

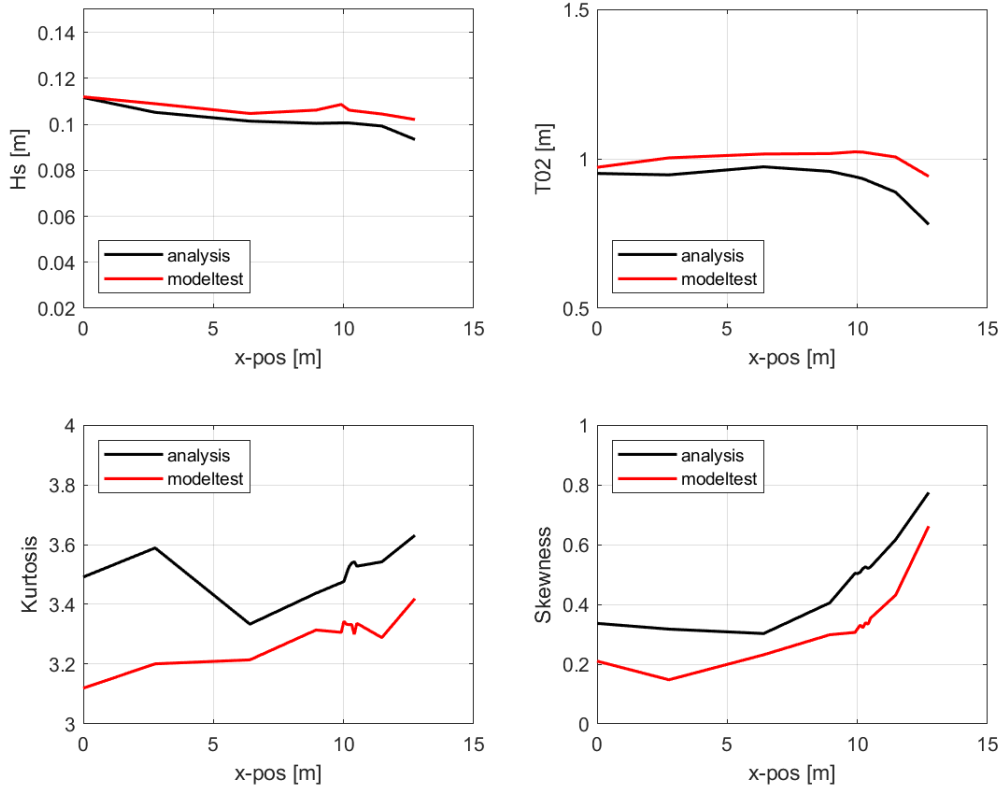


Figure 4-18 Spectral parameter variation, as a function of position in the tank, for test 2115. Reference position ( $x=0$ ) is in this case WP-02.

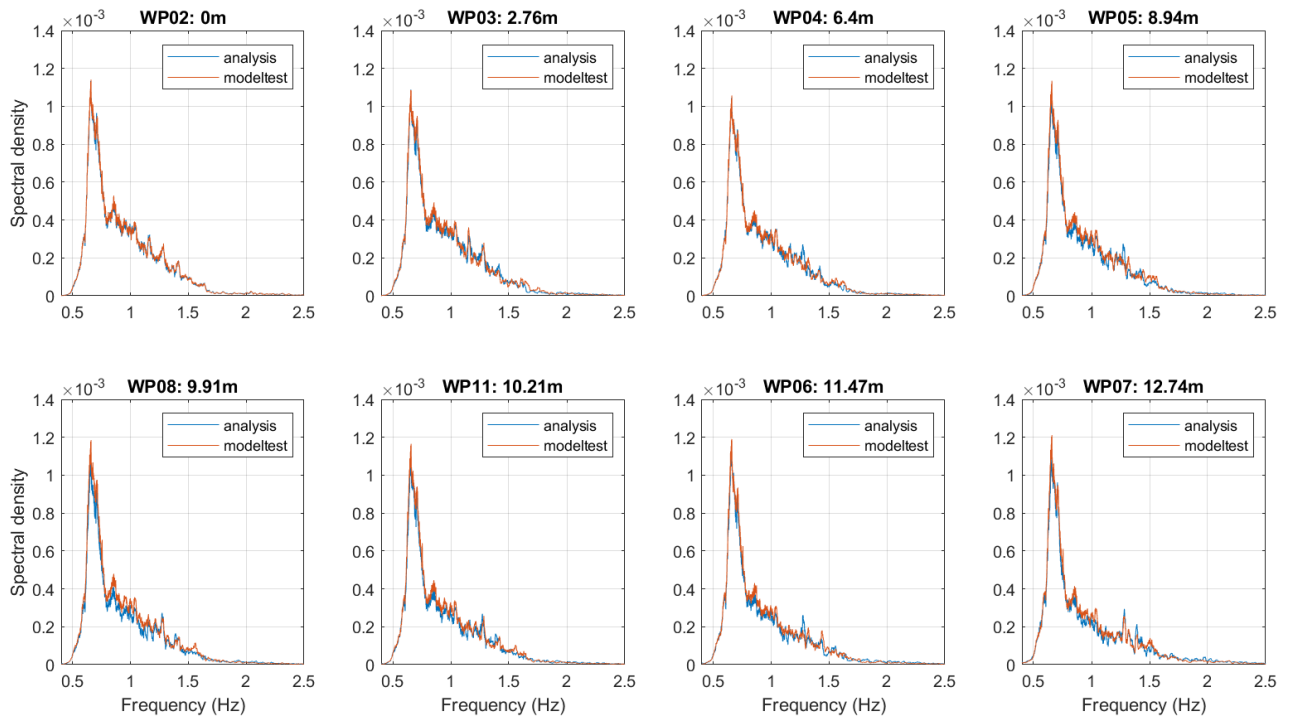


Figure 4-19 Spectral density plots for a selection of wave gauges spanning the basin length. Test 2114.

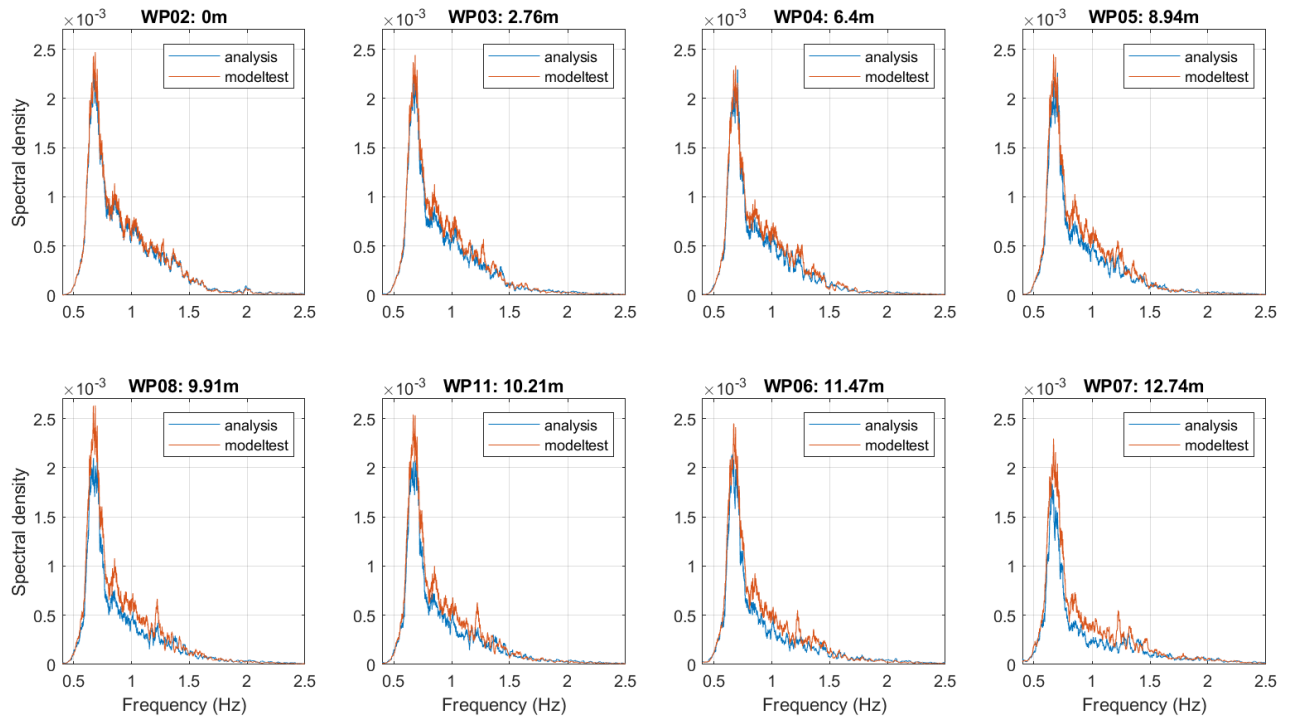


Figure 4-20 Spectral density plots for a selection of wave gauges spanning the basin length. Test 2115.

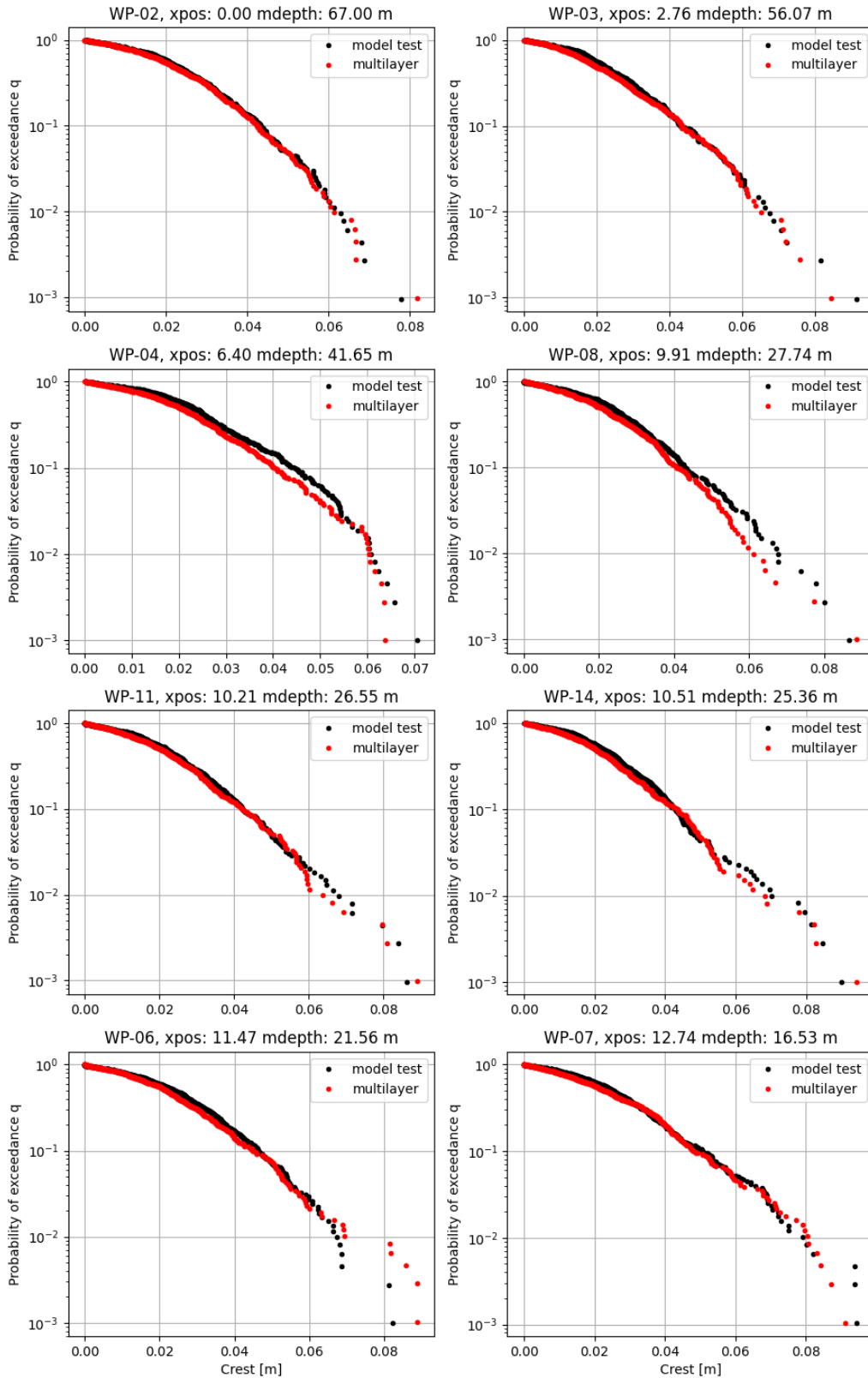


Figure 4-21: Test 2114 – Comparison of crest distributions at different locations along the slope. Plots have been sorted in ascending order with respect to position.

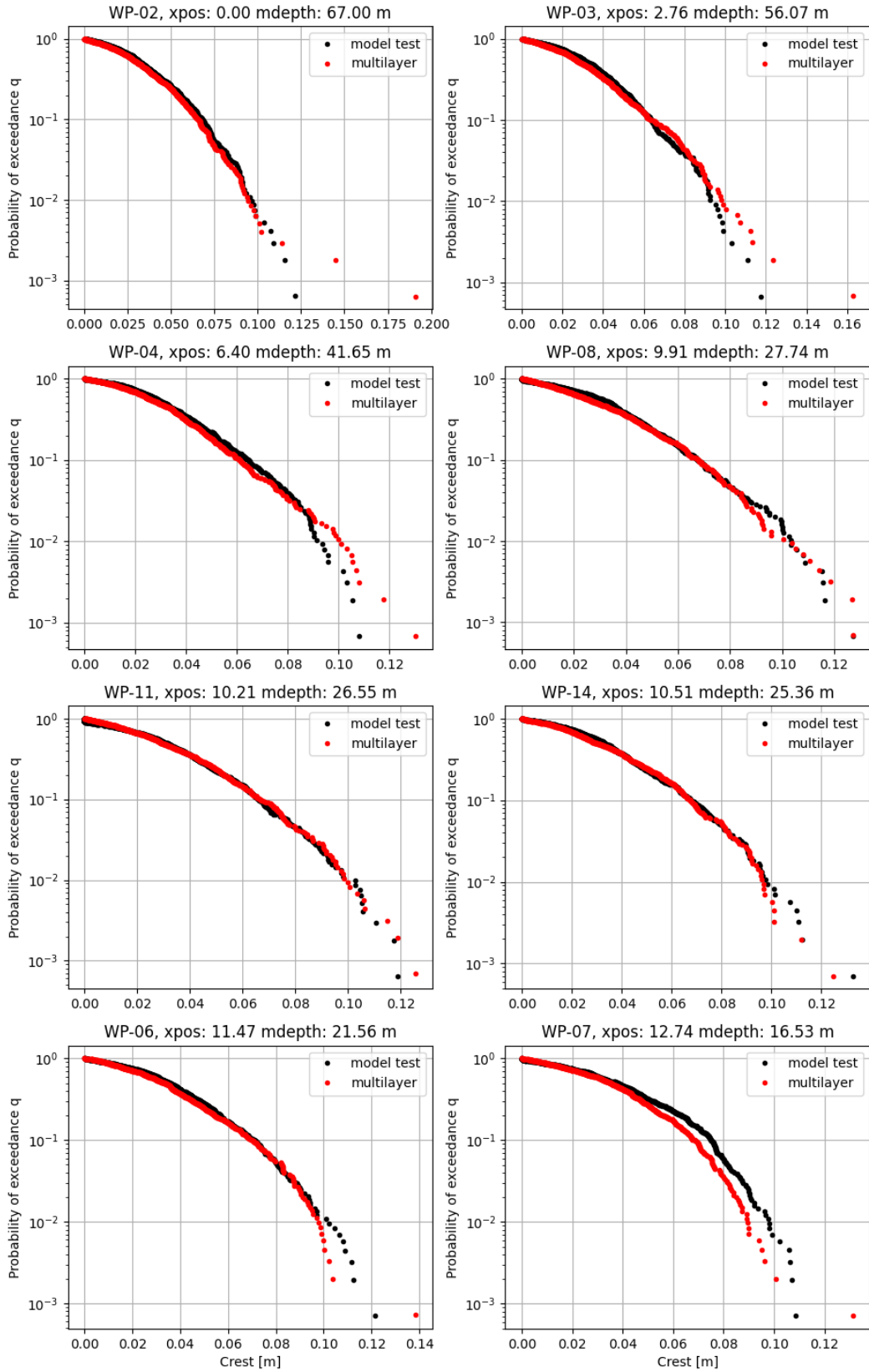


Figure 4-22 Test 2115 – Comparison of crest distributions at different locations along the slope. Plots have been sorted in ascending order with respect to position.

## 4.5. Discussion on variable water depth and coastal simulation

Statistical modelling of ocean waves is complicated by their nonlinearity, which leads in turn to non-Gaussian statistical behavior. While non-Gaussianity is present even in deep-water applications, its effects are especially pronounced as water depths decrease, as have been shown in this report. Introducing variable bathymetry and a coastline, further complicates the picture, having a significant impact on the wave field. In such cases one should not rely on empirical formulations derived for measurements at constant water depths to provide an adequate result.

In this chapter, a non-hydrostatic multilayer wave model has been demonstrated to be a good tool for propagation of phase resolved waves in the coastal zone, where other solvers may struggle. The model can be used at any water depth for propagation of irregular short- and long-crested waves, and handles variable water depth, coast interaction and wave breaking. Through rigorous testing and validation of the model it has proven to be robust and efficient and is likely to become a useful tool for wave load calculation in future coastal engineering.

Four different validation cases were considered in the pursuit to validate and test the model. The results are indeed very promising and are likely to improve further as the wave model matures.

## 5. General conclusion

After a validation of different components of the HOSM, especially the wave breaking model, a study has been conducted of 4 cases relevant for the HIPERWIND project. Those cases are defined at two geographical locations, with two sea states selected on each of them. The influence of the wave breaking model, both for short crested and long crested waves was quantified. It has been shown that while the influence of the angular spreading for BF, BT and TF cases was limited, a large modification of the crest elevation statistics was denoted for the TF case: in this case, the angular spreading greatly modifies the breaking behavior and therefore, the statistical distribution of crest elevation.

Afterwards, a study on the statistics of the horizontal kinematics, comparing usual engineering models (based on extensions of the linear wave theory) against a HOS model, was conducted. An underprediction of the maximal values was denoted and could be found throughout the four cases. The stretching models do not manage to recover the non-linear predictions, neither in terms of free surface elevation nor in terms of kinematics. This effect is increasing with the sea state steepness  $H_s/\lambda_p$ . Other influences of different assumptions were also investigated and quantified but shown to be of lower magnitude: the selection of random amplitudes for the wave spectrum is for example shown not to significantly affect the statistics of the kinematics nor free surface elevations.

Finally, because the presence of a variable bathymetry is also known to modify the statistics of the free surface elevation and kinematics, a Boussinesq-type multilayer model, allowing the simulation of variable water depth problems, has been validated against model tests.

## 6. Synthesis on the uncertainties

In conclusion, while the range of validity of the linear theory is often considered as being  $H_s/\lambda_p \in [0\%, 1\%]$ , valuable information is also obtained at higher relative wave height, though an underprediction of about 10 to 15% in wave height and velocity can be expected at crest. Giving a quantification for the acceleration is more difficult, knowing the instability at the required number of modes to accurately capture the second derivatives with the nonlinear models, but at least 15% of underprediction might be expected. Using deterministic amplitude when selecting the modes from a given spectrum is shown to have no – or

at least negligible – impact on the three studied variables. Finally, depending on the directional spreading of the sea state, 5 to 15% of overestimation of the  $v_x$  can be denoted when simplifying by concentrating all the energy along one dimension, compared to a more physical multidirectional spectrum.

## 7. References

- [1] S. Popinet, “A vertically-Lagrangian, non-hydrostatic, multilayer model for multiscale free-surface flows,” *J. Comput. Phys.*, p. 109609, 2020.
- [2] K. Dysthe, H. E. Krogstad, and P. Müller, “Oceanic rogue waves,” *Annu Rev Fluid Mech*, vol. 40, no. 1, pp. 287–310, 2008.
- [3] T. A. A. Adcock and P. H. Taylor, “The physics of anomalous (‘rogue’) ocean waves,” *Rep. Prog. Phys.*, vol. 77, no. 10, p. 105901, 2014.
- [4] E. Bitner-Gregersen and O. Gramstad, *Rogue Waves - Impact on ships and offshore structures*. DNV GL Strategic Research & Innovation, 2016.
- [5] B. J. West, K. A. Brueckner, R. S. Janda, D. M. Milder, and R. L. Milton, “A new numerical method for surface hydrodynamics,” *J Geophys Res*, vol. 92, no. C11, pp. 11803–11824, 1987, doi: 10.1029/JC092iC11p11803.
- [6] D. G. Dommermuth and D. K. P. Yue, “A high-order spectral method for the study of nonlinear gravity waves,” *J Fluid Mech*, vol. 184, pp. 267–288, 1987, doi: 10.1017/S002211208700288X.
- [7] W. J. D. Bateman, C. Swan, and P. H. Taylor, “On the calculation of the water particle kinematics arising in a directionally spread wavefield,” *J Comput Phys*, vol. 186, no. 1, pp. 70–92, 2003.
- [8] V. E. Zakharov, “Stability of periodic waves of finite amplitude on the surface of a deep fluid,” *J Appl Mech Tech Phys*, vol. 9, pp. 190–194, 1968.
- [9] W. Craig and C. Sulem, “Numerical Simulation of Gravity Waves,” *J Comput Phys*, vol. 108, no. 1, pp. 73–83, Sep. 1993.
- [10] W. J. D. Bateman, C. Swan, and P. H. Taylor, “On the Efficient Numerical Simulation of Directionally Spread Surface Water Waves,” *J Comput Phys*, vol. 174, no. 1, pp. 277–305, Nov. 2001.
- [11] O. Gramstad, “User manual for DNV GL HOSM program,” DNV GL, 2017.
- [12] W. Xiao, Y. Liu, G. Wu, and D. K. P. Yue, “Rogue wave occurrence and dynamics by direct simulations of nonlinear wave-field evolution,” *J Fluid Mech*, vol. 720, pp. 357–392, 2013, doi: 10.1017/jfm.2013.37.
- [13] O. Gramstad, E. Bitner-Gregersen, K. Trulsen, and J. C. Nieto Borge, “Modulational Instability and Rogue Waves in Crossing Sea States,” *J Phys Ocean.*, vol. 48, no. 6, pp. 1317–1331, 2018, doi: 10.1175/jpo-d-18-0006.1.
- [14] K. Trulsen, J. C. Nieto Borge, O. Gramstad, L. Aouf, and J. M. Lefèvre, “Crossing sea state and rogue wave probability during the Prestige accident,” *J Geophys Res Oceans*, vol. 120, no. 10, pp. 7113–7136, Oct. 2015.
- [15] R. Kurnia and E. van Groesen, “High order Hamiltonian water wave models with wave-breaking mechanism,” *Coast Eng*, vol. 93, pp. 55–70, Nov. 2014.
- [16] B. R. Seiffert and G. Ducrozet, “A Comparative Study of Wave Breaking Models in a High-Order Spectral Model,” in *OMAE2017*, Volume 7B: Ocean Engineering, Jun. 2017. doi: 10.1115/OMAE2017-61664.
- [17] B. R. Seiffert, G. Ducrozet, and F. Bonnefoy, “Simulation of breaking waves using the high-order spectral method with laboratory experiments: Wave-breaking onset,” *Ocean Model.*, vol. 119, pp. 94–104, Nov. 2017, doi: 10.1016/j.ocemod.2017.09.006.

- [18] X. Barthelemy, M. L. Banner, W. L. Peirson, F. Fedele, M. Allis, and F. Dias, "On a unified breaking onset threshold for gravity waves in deep and intermediate depth water," *J. Fluid Mech.*, vol. 841, pp. 463–488, 2018, doi: 10.1017/jfm.2018.93.
- [19] Z. Tian, M. Perlin, and W. Choi, "Energy dissipation in two-dimensional unsteady plunging breakers and an eddy viscosity model," *J. Fluid Mech.*, vol. 655, pp. 217–257, Jul. 2010, doi: 10.1017/S0022112010000832.
- [20] Z. Tian, M. Perlin, and W. Choi, "An eddy viscosity model for two-dimensional breaking waves and its validation with laboratory experiments," *Phys. Fluids*, vol. 24, no. 3, p. 036601, Mar. 2012, doi: 10.1063/1.3687508.
- [21] M. Felsberg and G. Sommer, "The monogenic signal," *IEEE Trans. Signal Process.*, vol. 49, no. 12, pp. 3136–3144, Dec. 2001, doi: 10.1109/78.969520.
- [22] C. P. Bridge, "Introduction To The Monogenic Signal," *ArXiv170309199 Cs*, Mar. 2017, Accessed: Apr. 21, 2021. [Online]. Available: <http://arxiv.org/abs/1703.09199>
- [23] G. Ducrozet, F. Bonnefoy, D. Le Touzé, and P. Ferrant, "A modified High-Order Spectral method for wavemaker modeling in a numerical wave tank," *European Journal of Mechanics - B/Fluids*, vol. 34, pp. 19–34, 2012. doi: <http://dx.doi.org/10.1016/j.euromechflu.2012.01.017>.
- [24] G. Ducrozet and M. Gouin, "Influence of varying bathymetry in rogue wave occurrence within unidirectional and directional sea-states," *Journal of Ocean Engineering and Marine Energy*. 2017. doi: 10.1007/s40722-017-0086-6.
- [25] O. Gramstad and G. Lian, "Long-term analysis of wave-induced loads using High Order Spectral Method and direct sampling of extreme wave events."
- [26] J. N. Sharma and R. G. Dean, "Development and evaluation of a procedure for simulating a random directional second order sea surface and associated wave forces," Univ. of Delaware, Newark, Ocean Eng. Report 20, 1979.
- [27] V. P. Krasitskii, "On reduced equations in the Hamiltonian theory of weakly nonlinear surface-waves," *J Fluid Mech*, vol. 272, pp. 1–20, 1994.
- [28] D. Dommermuth, "The initialization of nonlinear waves using an adjustment scheme," *Wave Motion*, vol. 32, no. 4, pp. 307–317, 2000.
- [29] G. Ducrozet, F. Bonnefoy, and Y. Perignon, "Applicability and limitations of highly non-linear potential flow solvers in the context of water waves," *Ocean Eng.*, vol. 142, pp. 233–244, Sep. 2017, doi: 10.1016/j.oceaneng.2017.07.003.
- [30] G. Z. Forristall, "Wave Crest Distributions: Observations and Second-Order Theory," *J. Phys. Oceanogr.*, vol. 30, no. 8, pp. 1931–1943, 2000, doi: 10.1175/1520-0485(2000)030<1931:WCDOAS>2.0.CO;2.
- [31] R. Gibson, "LOADS JIP Phase 2 Model Uncertainty," OCG-50-01-21B Rev. B, Jun. 2021.
- [32] D. N. Veritas, "Offshore Standard DNV-OS-J101: Design of Offshore Wind Turbine Structures," Høvik, Norway, May 2014. [Online]. Available: <https://rules.dnv.com/docs/pdf/dnvpmp/codes/docs/2014-05/Os-J101.pdf>
- [33] A. Babarit and G. Delhommeau, "Theoretical and numerical aspects of the open source BEM solver NEMOH," in *11th European wave and tidal energy conference (EWTEC2015)*, Nantes, France, 2015.
- [34] "TEESSIDE OFFSHORE WIND FARM DESIGN BASIS PART C2 GEOTECHNICAL AND ENVIRONMENTAL DATA."
- [35] T. B. Benjamin and J. E. Feir, "The disintegration of wave trains on deep water Part 1. Theory," *J Fluid Mech*, vol. 27, no. 3, pp. 417–430, 1967, doi: doi:10.1017/S002211206700045X.
- [36] DNV GL, *Recommended Practice DNVGL-RP-C205: Environmental Conditions and Environmental Loads*. DNV GL, 2019.
- [37] D. R. Crawford, P. G. Saffman, and H. C. Yuen, "Evolution of a random inhomogeneous field of non-linear deep-water gravity-waves," *Wave Motion*, vol. 2, pp. 1–16, 1980.

- [38] M. Onorato *et al.*, “Statistical properties of mechanically generated surface gravity waves: a laboratory experiment in a three-dimensional wave basin,” *J Fluid Mech*, vol. 627, pp. 235–257, 2009, doi: 10.1017/S002211200900603X.
- [39] O. Gramstad and K. Trulsen, “Influence of crest and group length on the occurrence of freak waves,” *J Fluid Mech*, vol. 582, pp. 463–472, 2007.
- [40] B. J. West, K. A. Brueckner, R. S. Janda, D. M. Milder, and R. L. Milton, “A new numerical method for surface hydrodynamics,” *J. Geophys. Res.*, vol. 92, no. C11, p. 11803, 1987, doi: 10.1029/JC092iC11p11803.
- [41] D. G. Dommermuth and D. K. Yue, “A high-order spectral method for the study of nonlinear gravity waves,” *J. Fluid Mech.*, vol. 184, pp. 267–288, 1987.
- [42] D. G. Dommermuth, E. A. Schlageter, J. C. Talcott, D. C. Wyatt, and E. A. Novikov, “Numerical Simulation of Bow Waves and Transom-Stern Flows,” in *APS Division of Fluid Dynamics Meeting Abstracts*, Nov. 1997, vol. abstract id. Ee.05. Accessed: Jun. 07, 2021. [Online]. Available: <http://adsabs.harvard.edu/abs/1997APS..DFD..Ee05D>
- [43] G. Ducrozet, “Modélisation des processus non-linéaires de génération et de propagation d’états de mer par une approche spectrale,” 2007.
- [44] B. R. Seiffert, G. Ducrozet, and F. Bonnefoy, “Simulation of breaking waves using the high-order spectral method with laboratory experiments: Wave-breaking onset,” *Ocean Model.*, vol. 119, pp. 94–104, 2017.
- [45] B. R. Seiffert and G. Ducrozet, “Simulation of breaking waves using the high-order spectral method with laboratory experiments: wave-breaking energy dissipation,” *Ocean Dyn.*, vol. 68, no. 1, pp. 65–89, 2018.
- [46] Z. Tian, M. Perlin, and W. Choi, “Energy dissipation in two-dimensional unsteady plunging breakers and an eddy viscosity model,” *J. Fluid Mech.*, vol. 655, pp. 217–257, Jul. 2010, doi: 10.1017/S0022112010000832.
- [47] Z. Tian, M. Perlin, and W. Choi, “An eddy viscosity model for two-dimensional breaking waves and its validation with laboratory experiments,” *Phys. Fluids*, vol. 24, no. 3, p. 036601, Mar. 2012, doi: 10.1063/1.3687508.
- [48] J. Sutherland, “The dynamics of nonlinear water wave groups,” PhD Thesis, University of Edinburgh, 1992.
- [49] B. Molin, *Hydrodynamique des structures offshore*. Editions Technip, 2002.
- [50] Y. Scolan and O. Kimmoun, “Cinématique de crêtes de houle, Campagne d’essais dans la cuve Roger BRARD.”
- [51] J. D. Wheeler, “Method for Calculating Forces Procedure by Irregular Waves,” in *OTC 1006 Offshore Technology Conference*, 1969.
- [52] S. F. D. Pawsey and F. J. Della Stritto, “Improved wave kinematics from wave staff arrays,” in *Offshore Technology Conference*, 1983.
- [53] M. J. Tucker, P. G. Challenor, and D. J. T. Carter, “Numerical simulation of a random sea: a common error and its effect upon wave group statistics,” *Appl. Ocean Res.*, vol. 6, no. 2, pp. 118–122, 1984.
- [54] M. Gouin, G. Ducrozet, and P. Ferrant, “Development and validation of a non-linear spectral model for water waves over variable depth,” *Eur. J. Mech.-BFluids*, vol. 57, pp. 115–128, 2016.
- [55] M. Gouin, G. Ducrozet, and P. Ferrant, “Propagation of 3D nonlinear waves over an elliptical mound with a high-order spectral method,” *Eur. J. Mech.-BFluids*, vol. 63, pp. 9–24, 2017.
- [56] C. Lawrence, K. Trulsen, and O. Gramstad, “Statistical properties of wave kinematics in long-crested irregular waves propagating over non-uniform bathymetry,” *Phys. Fluids*, vol. 33, no. 4, p. 046601, 2021.
- [57] J. T. Kirby, “Boussinesq models and applications to nearshore wave propagation, surf zone processes and wave-induced currents,” in *Elsevier Oceanography Series*, vol. 67, Elsevier, 2003, pp. 1–41.

- [58] Q. Chen, J. T. Kirby, R. A. Dalrymple, A. B. Kennedy, and A. Chawla, "Boussinesq modeling of wave transformation, breaking, and runup. II: 2D," *J. Waterw. Port Coast. Ocean Eng.*, vol. 126, no. 1, pp. 48–56, 2000.
- [59] Y. Liu, Y. Shi, D. A. Yuen, E. O. Sevre, X. Yuan, and H. L. Xing, "Comparison of linear and nonlinear shallow wave water equations applied to tsunami waves over the China Sea," *Acta Geotech.*, vol. 4, no. 2, pp. 129–137, 2009.
- [60] J. Boussinesq, "Théorie de l'intumescence liquide appelée onde solitaire ou de translation se propageant dans un canal rectangulaire," *CR Acad Sci Paris*, vol. 72, no. 755–759, p. 1871, 1871.
- [61] P. Madsen and H. Schäffer, "Higher-order Boussinesq-type equations for surface gravity waves: derivation and analysis," *Philos. Trans. R. Soc. Lond. Ser. Math. Phys. Eng. Sci.*, vol. 356, no. 1749, pp. 3123–3181, 1998.
- [62] P. J. Lynett, "Nearshore wave modeling with high-order Boussinesq-type equations," *J. Waterw. Port Coast. Ocean Eng.*, vol. 132, no. 5, pp. 348–357, 2006.
- [63] G. Stelling and M. Zijlema, "An accurate and efficient finite-difference algorithm for non-hydrostatic free-surface flow with application to wave propagation," *Int. J. Numer. Methods Fluids*, vol. 43, no. 1, pp. 1–23, 2003.
- [64] M. Zijlema and G. S. Stelling, "Further experiences with computing non-hydrostatic free-surface flows involving water waves," *Int. J. Numer. Methods Fluids*, vol. 48, no. 2, pp. 169–197, 2005.
- [65] V. Casulli, "A semi-implicit finite difference method for non-hydrostatic, free-surface flows," *Int. J. Numer. Methods Fluids*, vol. 30, no. 4, pp. 425–440, 1999.
- [66] M. Zijlema, G. Stelling, and P. Smit, "SWASH: An operational public domain code for simulating wave fields and rapidly varied flows in coastal waters," *Coast. Eng.*, vol. 58, no. 10, pp. 992–1012, 2011.
- [67] Ø. Lande and J. B. Helmers, "CFDwavemaker: An open-source library for efficient generation of higher-order wave kinematics," in *International Conference on Offshore Mechanics and Arctic Engineering*, 2022.
- [68] J. Sharma, R. Dean, and others, "Second-order directional seas and associated wave forces," *Soc. Pet. Eng. J.*, vol. 21, no. 01, pp. 129–140, 1981.
- [69] Ø. Lande, "CFDwavemaker repository," Dec. 2021. <https://github.com/oystelan/CFDwavemaker>
- [70] T. B. Johannessen, "The effect of directionality on the nonlinear behaviour of extreme transient ocean waves," PhD Thesis, University of London, 1997.
- [71] Ø. Lande and T. B. Johannessen, "Propagation of Steep and Breaking Short-Crested Waves: A Comparison of CFD Codes," in *International Conference on Offshore Mechanics and Arctic Engineering*, 2018, vol. 51210, p. V002T08A022.
- [72] M. Boers, "Simulation of a surf zone with a barred beach; Part 1: wave heights and wave breaking," *Oceanogr. Lit. Rev.*, vol. 4, no. 44, p. 292, 1997.
- [73] Y. Qi, G. Wu, Y. Liu, M.-H. Kim, and D. K. Yue, "Nonlinear phase-resolved reconstruction of irregular water waves," *J. Fluid Mech.*, vol. 838, pp. 544–572, 2018.
- [74] W. Fujimoto and T. Waseda, "Ensemble-based variational method for nonlinear inversion of surface gravity waves," *J. Atmospheric Ocean. Technol.*, vol. 37, no. 1, pp. 17–31, 2020.
- [75] E. Svangstu, "An investigation of wave conditions and wave induced loads for design of wind turbine foundations at 15–40m depth," Master's Thesis, Norges teknisk-naturvitenskapelige universitet, Fakultet for ..., 2011.
- [76] S. R. Winterstein and S. Haver, "Modelling Shallow-Water Waves: Truncated Hermite Models and the ShallowWave Routine," in *International Conference on Offshore Mechanics and Arctic Engineering*, 2015, vol. 56499, p. V003T02A049.